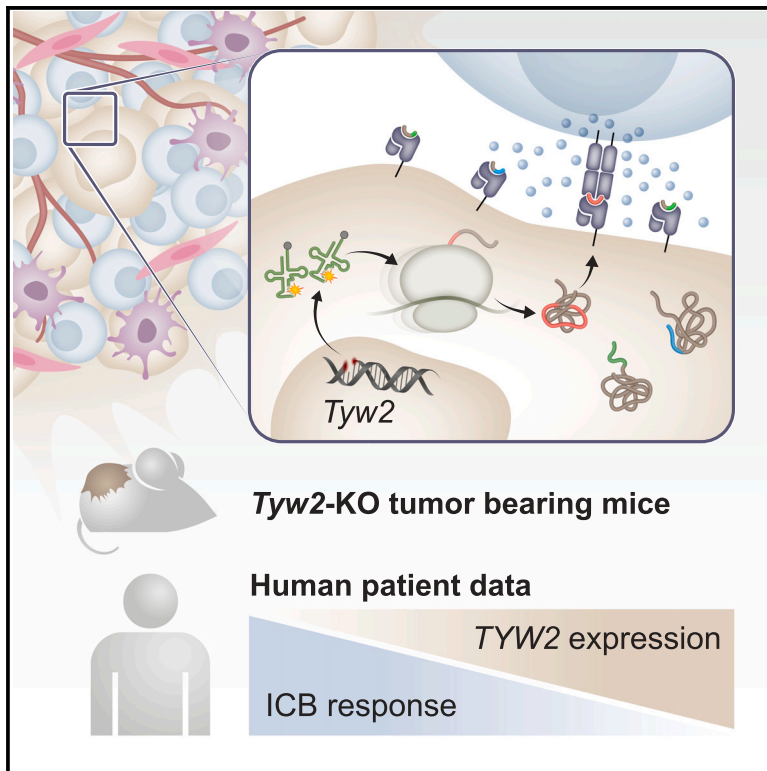


# Cancer Cell

## Translation dysregulation in cancer as a source for targetable antigens

### Graphical abstract



### Authors

Chen Weller, Osnat Bartok, Christopher S. McGinnis, ..., Eytan Ruppin, Andreas Schlosser, Yarden Samuels

### Correspondence

yarden.samuels@weizmann.ac.il

### In brief

Weller et al. substantiate the role of translation dysregulation in mediating anti-tumor immunity by demonstrating that *TYW2* loss in melanoma cells induces aberrant peptide MHC presentation, increasing both tumor immunogenicity and sensitivity to ICB therapy. *TYW2* expression levels in patients with melanoma predict clinical outcomes, highlighting translation regulatory factors as immunotherapy targets.

### Highlights

- *TYW2* loss induces ribosomal FS and immunogenic aberrant peptide MHC presentation
- Impaired translation fidelity limits tumor growth in a CD8<sup>+</sup> T cell-dependent manner
- *Tyw2* KO enhances CD8<sup>+</sup> T cell infiltration into tumors and sensitivity to ICB
- *TYW2* expression predicts survival and ICB response in patients with primary melanoma

Article

# Translation dysregulation in cancer as a source for targetable antigens

Chen Weller,<sup>1,24</sup> Osnat Bartok,<sup>1,24</sup> Christopher S. McGinnis,<sup>2,3,24</sup> Heyilimu Palashati,<sup>4,5</sup> Tian-Gen Chang,<sup>6</sup> Dmitry Malko,<sup>1</sup> Merav D. Shmueli,<sup>7</sup> Asuteka Nagao,<sup>8</sup> Deborah Hayoun,<sup>1</sup> Ayaka Murayama,<sup>8</sup> Yuriko Sakaguchi,<sup>8</sup> Panagiotis Poulis,<sup>9</sup> Aseel Khatib,<sup>10</sup> Bracha Erlanger Avigdor,<sup>1</sup> Sagi Gordon,<sup>1</sup> Sapir Cohen Shvefel,<sup>1</sup> Marie J. Zemanek,<sup>1</sup> Morten M. Nielsen,<sup>4,5</sup> Sigalit Boura-Halfon,<sup>11</sup> Shira Sagie,<sup>1</sup> Nofar Gumpert,<sup>1</sup> Weiwen Yang,<sup>4,5</sup> Dmitry Alexeev,<sup>12</sup> Pelgia Kyriakidou,<sup>12</sup> Winnie Yao,<sup>2,3</sup> Mirie Zerbib,<sup>13</sup> Polina Greenberg,<sup>1</sup> Gil Benedek,<sup>14</sup> Kevin Litchfield,<sup>15,16</sup> Ekaterina Petrovich-Kopitman,<sup>17</sup> Adi Nagler,<sup>1</sup> Roni Oren,<sup>13</sup> Shifra Ben-Dor,<sup>18</sup> Yishai Levin,<sup>19</sup> Yitzhak Pilpel,<sup>20</sup> Marina Rodnina,<sup>9</sup> Jürgen Cox,<sup>12</sup> Yifat Merbl,<sup>7</sup> Ansuman T. Satpathy,<sup>2,3</sup> Yaron Carmi,<sup>10</sup> Florian Erhard,<sup>21</sup> Tsutomu Suzuki,<sup>8</sup> Allen R. Buskirk,<sup>22</sup> Johanna Olweus,<sup>4,5</sup> Eytan Ruppin,<sup>6</sup> Andreas Schlosser,<sup>23</sup> and Yardena Samuels<sup>1,25,\*</sup>

<sup>1</sup>Department of Molecular Cell Biology, Weizmann Institute of Science, Rehovot 7610001, Israel

<sup>2</sup>Department of Pathology, Stanford University, Stanford, CA 94305, USA

<sup>3</sup>Parker Institute for Cancer Immunotherapy, San Francisco, CA 94129, USA

<sup>4</sup>Department of Cancer Immunology, Institute for Cancer Research, Oslo University Hospital, 0379 Oslo, Norway

<sup>5</sup>Precision Immunotherapy Alliance, University of Oslo, Oslo, Norway

<sup>6</sup>Cancer Data Science Laboratory, Center for Cancer Research, National Cancer Institute, National Institutes of Health, Bethesda, MD 20892, USA

<sup>7</sup>Department of Systems Immunology, Weizmann Institute of Science, Rehovot 7610001, Israel

<sup>8</sup>Department of Chemistry and Biotechnology, Graduate School of Engineering, The University of Tokyo, Tokyo 113-8656, Japan

<sup>9</sup>Department of Physical Biochemistry, Max Planck Institute for Multidisciplinary Sciences, 37077 Göttingen, Germany

<sup>10</sup>Department of Pathology, Sackler School of Medicine, Tel Aviv University, Tel Aviv 69978, Israel

<sup>11</sup>Department of Immunology and Regenerative Biology, Weizmann Institute of Science, Rehovot 7610001, Israel

<sup>12</sup>Computational Systems Biochemistry Research Group, Max-Planck Institute of Biochemistry, 82152 Martinsried, Germany

<sup>13</sup>Department of Veterinary Resources, Weizmann Institute of Science, Rehovot 7610001, Israel

<sup>14</sup>Tissue Typing and Immunogenetics Unit, Hadassah Hebrew University Hospital, Jerusalem 9112102, Israel

<sup>15</sup>CRUK Lung Cancer Centre of Excellence, University College London Cancer Institute, London WC1E 6DD, UK

<sup>16</sup>Tumour Immunogenomics and Immunosurveillance Laboratory, University College London Cancer Institute, London WC1E 6DD, UK

<sup>17</sup>Department of Life Science Core Facilities, Weizmann Institute of Science, Rehovot 7610001, Israel

<sup>18</sup>Bioinformatics Unit, Department of Life Sciences Core Facilities, Weizmann Institute of Science, Rehovot 7610001, Israel

<sup>19</sup>de Botton Institute for Protein Profiling, the Nancy and Stephen Grand Israel National Center for Personalized Medicine, Weizmann Institute of Science, Rehovot 7610001, Israel

<sup>20</sup>Department of Molecular Genetics, Weizmann Institute of Science, Rehovot 7610001, Israel

<sup>21</sup>Faculty for Informatics and Data Science, University of Regensburg, 93040 Regensburg, Germany

<sup>22</sup>Department of Molecular Biology and Genetics, Johns Hopkins University School of Medicine, Baltimore, MD 21205, USA

<sup>23</sup>Rudolf Virchow Center, Center for Integrative and Translational Bioimaging, Julius-Maximilians-University Würzburg, 97080 Würzburg, Germany

<sup>24</sup>These authors contributed equally

<sup>25</sup>Lead contact

\*Correspondence: [yardena.samuels@weizmann.ac.il](mailto:yardena.samuels@weizmann.ac.il)

<https://doi.org/10.1016/j.ccell.2025.03.003>

## SUMMARY

Aberrant peptides presented by major histocompatibility complex (MHC) molecules are targets for tumor eradication, as these peptides can be recognized as foreign by T cells. Protein synthesis in malignant cells is dysregulated, which may result in the generation and presentation of aberrant peptides that can be exploited for T cell-based therapies. To investigate the role of translational dysregulation in immunological tumor control, we disrupt translation fidelity by deleting tRNA<sup>tyrosine</sup>-synthesizing protein 2 (*TYW2*) in tumor cells and characterize the downstream impact on translation fidelity and immunogenicity using immunopeptidomics, genomics, and functional assays. These analyses reveal that *TYW2* knockout (KO) cells generate immunogenic out-of-frame peptides. Furthermore, *Tyw2* loss increases tumor immunogenicity and leads to anti-programmed cell death 1 (PD-1) checkpoint blockade sensitivity *in vivo*. Importantly, reduced *TYW2* expression is associated with increased response to checkpoint blockade in patients. Together, we demonstrate that defects in translation fidelity drive tumor immunogenicity and may be leveraged for cancer immunotherapy.

## INTRODUCTION

Recent clinical successes of cancer immunotherapies have highlighted the importance of identifying cancer neoantigens—novel epitopes of self-antigens that derive from mutant proteins—for anti-tumor immunity.<sup>1–3</sup> Indeed, identifying neoantigens derived from tumor-specific somatic mutations has enabled the advent of therapeutic cancer vaccines.<sup>4–8</sup> However, personalized immunotherapies are limited to certain cancer types and are seldom curative.<sup>9</sup> A major contributing factor to this limitation is the scarcity of identified targetable antigens, particularly in low tumor mutational burden (TMB) settings. One potential solution to this issue arises from the generation of antigens derived from dysregulated transcription, splicing, or translation.<sup>10–25</sup>

Mistranslation in cancer cells is a potentially rich source of aberrant peptides. Translation is a multi-step process that requires amino acid and tRNA recognition by aminoacyl-tRNA synthetases (AARSs), tRNA anticodon-codon pairing, and reading frame maintenance.<sup>26–28</sup> Notably, malignant cancers exhibit compromised translation fidelity as translation machinery is hijacked to enable unchecked proliferation, activation of oncogenic signaling pathways, and adaptation to the tumor microenvironment (TME).<sup>28–35</sup> For example, tRNA-modifying enzymes that modulate tRNA stability, translational accuracy, and efficiency are dysregulated in numerous cancer types and play a role in cancer progression.<sup>36–45</sup> However, whether this contributes to neoantigen generation has not been elucidated.

To explore how the loss of a single tRNA modifier affects translation fidelity and tumor immunogenicity, we studied tRNA wybutosine (yW)-synthesizing protein 2 (TYW2) (TRMT12), a tRNA Ado-Met-dependent transferase involved in the synthesis of yW at tRNA<sup>Phe</sup> position 37 (G37) adjacent to the anticodon, which promotes ribosome reading frame maintenance.<sup>46–48</sup> Notably, the role of TYW2 in tumor progression is complex; it is overexpressed in some cancer types<sup>49,50</sup> and epigenetically silenced in others.<sup>51</sup> Here, we investigate whether dysregulated translation fidelity in cancer increases neoantigen production and improves anti-tumor immune responses, providing insights into potential strategies for developing effective immunotherapies.

## RESULTS

### **TYW2 loss enhances programmed ribosomal frameshifts and induces ribosome stalling at Phe codons**

To interrogate the influence of TYW2 loss on the tumor transcriptome and immunopeptidome, we used CRISPR-Cas9 to knock out TYW2 in two melanoma cell lines, A375 and SKMEL30, and generated three single-cell derived TYW2 knockout (KO) lines from each source (Figure S1A). To assess the effect of TYW2 KO on tRNA<sup>Phe</sup> G37 modification, tRNA molecules from wild-type (WT) and KO cells were subjected to mass spectrometry (MS). As expected, tRNA<sup>Phe</sup> harbored the yW modifications o2yW and OHyW at G37 in WT cells. In contrast, these modifications were lost in KO cells, leaving only the intermediate-modified nucleoside imG-14 (Figures 1A and S1B). To substantiate the effect of hypomodified tRNA<sup>Phe</sup> on programmed ribosomal frameshifts (PRFs), we utilized a dual fluorescent protein reporter system<sup>52,53</sup> where mCherry-GFP fusion protein is produced

upon –1 frameshift (FS; Figure 1B). We observed a significant increase in PRF in TYW2 KO compared to WT cells (Figures 1C and S1C–S1G), demonstrating the regulatory effect of TYW2 on reading frame maintenance. Restoring TYW2 in KO cells rescued the enhanced ribosomal slippage phenotype (Figures 1C–1F and S1H–S1J), whereas restoring a K255Q loss of function mutant<sup>54</sup> did not (Figures 1D–1F).

We next used bulk RNA sequencing to measure transcriptional differences between TYW2 KO and WT cells. This analysis revealed increased expression of tRNA modifiers (e.g., TYW3 and ALKBH8/TRMT9A), components of antigen presentation machinery (e.g., B2M, human leukocyte antigen [HLA]-B, and TAP1), and translation-related RNA-binding proteins (e.g., NEMF, PELO, and CPEB1) in KO cells (Figures 1G and S1K). In contrast, several AARSs were downregulated in KO cells, including phenylalanyl-tRNA synthetase subunit beta (FARSB), supporting the role of TYW2 in regulating translation fidelity.

To further characterize the effects of yW modification loss on decoding, we performed ribosome profiling<sup>55</sup> on WT and KO cells. Given that yW37 is important for tRNA<sup>Phe</sup> binding to the ribosome-decoding site (A site),<sup>56,57</sup> we anticipated that ribosomes would dwell longer on Phe codons (UUC, UUU) in the absence of yW37. Indeed, average ribosome density was increased at UUC codons in the ribosomal A site in KO compared to WT cells (Figure 1H). In contrast, UUC codons positioned at the peptidyl (P) or exit (E) sites or neighboring positions showed little or no difference in ribosome density. Similarly, A site density at Phe codons was enriched relative to other sense codons and ribosome positions specifically in KO cells (Figures 1I, S1L, and S1M), indicating a delay in decoding. This A site stalling was not explained by differences in tRNA<sup>Phe</sup> aminoacylation status (Figure 1J) and did not result in global ribosome drop-off or frameshifting downstream of A sites (Figures S1N and S1O). Notably, a delayed decoding of the A site codon may allow the P site tRNA to FS –1 or +1,<sup>37,58,59</sup> similar to the effect of hypomodified tRNA<sup>Phe</sup> on PRF.<sup>27,53,59–61</sup> In this case, the translation product would not derive from the known slippery sequence patterns and would not include Phe (Figure 1K). In summary, these findings suggest that while there is no global effect of the hypomodified tRNA<sup>Phe</sup> on protein synthesis, TYW2 KO cells may be more susceptible to reading frame errors due to specific pausing at Phe codons.

### **Identification of out-of-frame HLA-bound peptides presented by TYW2 KO cells**

Defective ribosomal products are often unstable and prone to degradation and presentation by HLA molecules.<sup>62</sup> As ribosomal FS and expression of antigen presentation genes were increased in TYW2 KO cells, we hypothesized that HLA presentation of faulty translation products would increase in KO cells. To test this hypothesis, we applied immunopeptidomics<sup>63</sup> to the A375 and SKMEL30 lines described previously (Figures S2A and S2B), as well as to TYW2 KO and WT SKMEL5 clones that were also validated for enhanced PRF events upon TYW2 loss (Figures S2C–S2F).

To understand whether TYW2 loss affects the global immunopeptidome landscape, we first compared overrepresented biological pathways in WT and KO cells using Gene Ontology analysis (Figure S2G), which revealed many shared enriched

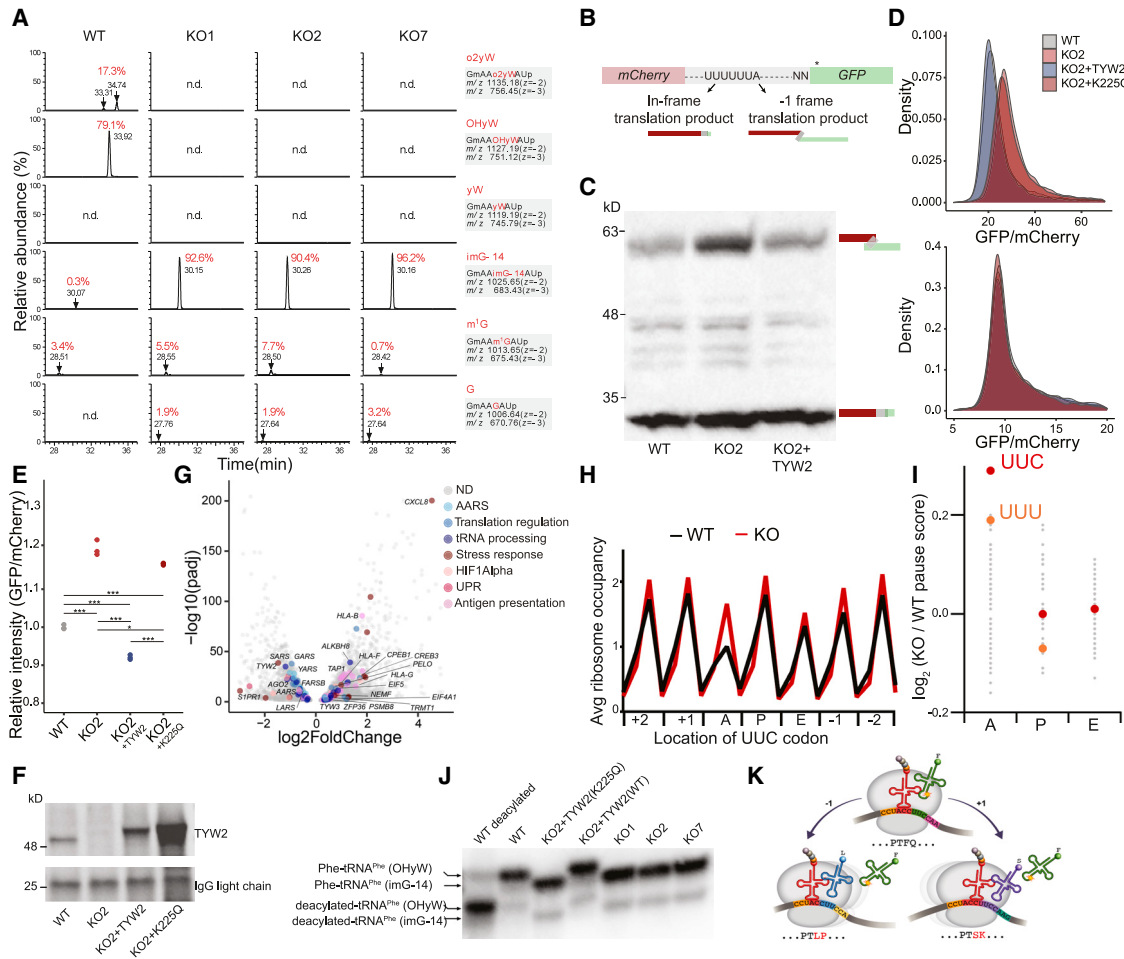


**Figure 1. TYW2 loss increases PRF events and induces ribosome pausing at Phe codons in the ribosomal A site**

(A) tRNA<sup>Phe</sup> modification status in A375 cells via MS shotgun analysis of class-I tRNA fraction from WT and TYW2 KO cells ( $n = 1$ ). Rows correspond to extracted ion chromatograms (XICs) for negative ions of tRNA<sup>Phe</sup> fragments bearing G37 with modifications corresponding to the G  $\rightarrow$  m<sup>1</sup>G  $\rightarrow$  imG-14  $\rightarrow$  yW  $\rightarrow$  OHyW/o2yW cascade. Sequence of each fragment with m/z values of doubly and triply charged ions for XICs is shown on the right. Target peaks are indicated by arrows with retention time. o2yW-containing fragment splits into two peaks. Percentage on each chromatogram represents relative abundance of each fragment (n.d., not detected).

(B) Schematic of the dual fluorescent reporter used for monitoring  $-1$  PRF. <sup>52</sup> \* represents in-frame stop codon.

(C) Western blot of mCherry in A375 cells: WT, KO2, and KO2 cells overexpressing (OE) WT TYW2 (KO2+TYW2), transfected with the  $-1$  FS construct described in (B).

(D) Density plots of GFP/mCherry abundance in A375 cells transfected with the  $-1$  FS (top) or frame 0 control (bottom) constructs, measured by flow cytometry.

(E) Scatterplot of the relative fold change in mean GFP/mCherry expression in WT, KO2, KO2+TYW2, and KO2+K225Q A375 cells transfected with the  $-1$  FS construct (normalized to WT;  $n = 3$  biological replicates of each cell line). One-way ANOVA, post hoc Tukey HSD test. \* $0.05 < p < 0.001$ , \*\*\* $p < 0.001$ .

(F) Western blot of TYW2 in WT, KO2, KO2+TYW2, and KO2+K225Q A375 cells following TYW2 immunoprecipitation.

(G) Volcano plot of differentially expressed genes ( $n = 2,040$  upregulated and  $n = 2,992$  downregulated in KO cells) in bulk RNA sequencing analysis of WT and KO2 A375 cells ( $p$  adj.  $< 0.05$ , Benjamini-Hochberg-corrected Wald test;  $n = 3$  replicates per group). ND, not determined.

(H) Line plot of average ribosome density aligned at UUC codons in TYW2 WT and KO SKMEL30 cells.

(I) Scatterplot of the KO:WT pause score ratios for all 61 sense codons at each ribosomal functional site (A, P, E;  $n = 2$  biological replicates per cell line). Phe codons UUC (red) and UUU (orange) are highlighted. UUU and UUC scores overlap in the E site; both values are 0.01.

(J) Aminoacylation status of tRNA<sup>Phe</sup> in each A375 cell line detected by acid-urea northern blotting ( $n = 3$  biological replicates). Aminoacylation and tRNA<sup>Phe</sup> G37 modification status indicated on the left. tRNA<sup>Phe</sup> from WT was deacylated by alkaline treatment and used as a control (left lane).

(K) Schematic illustrating proposed outcome of A site ribosome pausing at Phe codons; decoding of hypomodified tRNA<sup>Phe</sup> ( $-y$ W) is delayed, allowing P site tRNA to slip into either the  $-1$  or  $+1$  frame.

See also [Figure S1](#).

pathways among the cell lines. KO-specific enriched pathways included mRNA processing and antigen processing and presentation, mirroring our bulk RNA sequencing analyses (Table S1).

Next, given the importance of  $\gamma$ W37 modification of tRNA<sup>Phe</sup> in reading frame maintenance, we queried the immunopeptidomic data for out-of-frame (off-frame) HLA-bound peptides.<sup>19</sup> Consistent with previous studies, we detected cryptic peptides resulting from both off-frame and non-canonical translation<sup>10,12,16,19</sup> (Figure S2H). While a subset of off-frame peptides were detected in both WT and KO cells ( $n = 53$  in A375;  $n = 25$  in SKMEL30;  $n = 159$  in SKMEL5; Figures 2A, S2I, and S2J), we also identified a large number of KO-specific off-frame peptides ( $n = 46$  in A375, Figure 2A;  $n = 7$  in SKMEL30, Figure S2I;  $n = 38$  in SKMEL5, Figure S2J). Very few ( $n = 1$ –5) off-frame peptides were uniquely identified in WT samples (Figures 2A, S2I, and S2J).

To exclude the possibility that the increased detection of KO-specific off-frame peptides was due to higher levels of homogeneity compared to parental WT cells, we repeated this analysis using two independent A375 single-cell derived WT lines. Interestingly, these WT and KO lines exhibited distinct differences even at the canonical immunopeptidome level (Figures S2K–S2N). Furthermore, peptides identified in KO cells were biased toward the N terminus of the source protein (Figure S2O). Importantly, an off-frame peptide search revealed a KO-specific peptide cluster ( $n = 19$ , 12 detected in both KO lines) compared to a single off-frame peptide identified in the WT samples (Figure S2P), mirroring our previous results.

We next evaluated whether off-frame peptides were specifically associated with FS at Phe codons using a custom analysis pipeline (Figure 2B). First, we generated a reference database containing FS sequences proximal to Phe codons (“ProxyPhe”) that could result from ribosome slippage due to translocation (P-effect) or delay in decoding (“hungry frameshifting”; A-effect, Figures 1K and S3A–S3C). Second, we used two orthogonal peptide identification strategies (MaxQuant<sup>64</sup> and Peptide-PRISM<sup>19</sup>; Figure 2B) to generate a combined list of ProxyPhe-peptides (Table S1 and STAR Methods). Finally, to restrict hits to cancer-specific peptides, we filtered out peptides identified in the HLA-ligand ATLAS dataset<sup>65</sup> (Figures S3D and S3E; Table S1) and in immunopeptidomic data of healthy HLA-B\*57:01+ donors’ peripheral blood mononuclear cells (PBMCs) to account for the A375 cell allotype (Figures S3F–S3H; Table S1).

Overall, our analysis revealed 99 ProxyPhe-peptides (Table S1), 34 of which were specific to *TYW2* KO cells, versus 4 associated with WT controls (Table S1). These 99 peptides shared similar characteristics with identified HLA peptides (Figures 2C–2E; Table S1) and exhibited enhanced allelic enrichment scores for HLA-B\*57:01 (Figure 2F) and HLA-A\*11:01 (Figure S3I), consistent with prior studies reporting a biased presentation of cryptic peptides by HLA-A\*11:01 allele.<sup>19,66</sup> Moreover, ProxyPhe-peptide positions were biased toward the N terminus of their source protein compared to canonical peptides (Figure 2G).

Interestingly, while KO-specific ProxyPhe-peptides are derived from  $-1$  and  $+1$  FS,  $+1$  was dominant in this group (29/34 peptides; Table S1; Figure 2H). Moreover, six KO-specific peptides were identified as *trans*-frame (i.e., chimera of in-frame and out-of-frame sequences; Table S1). Of these six, two (AVAQLASRW and ILDSQPPEL) could arise from either off-frame or 5’ UTR translation of different source genes, respectively (Figure S3J). Further,

VIFVSVQTK represents a  $+1$  chimeric peptide that could result from either A- or P-effect induced by hypomodified tRNA<sup>Phe</sup> (Figure 2H). Spectrum validation using Prosit<sup>67</sup> comparison of experimentally identified and synthetic peptide sequences illustrated high Pearson correlation coefficient (PCC) scores for ProxyPhe-peptides (19/20 examined peptides showed  $>0.92$  PCC; Table S1; Figures 2H and S3K). Overall, these results confirm that loss of *TYW2* is associated with endogenous HLA presentation of aberrant peptides.

### ***TYW2* loss alters the degradome landscape**

To further validate the presence of aberrant, off-frame proteins associated with *TYW2* loss, we isolated proteasomes from WT and KO A375 cell lines and analyzed their degradation products using mass spectrometry analysis of proteolytic peptides (MAPP<sup>68,69</sup>; Figures S3L and S3M; Table S2). While WT and KO cells did not differ at the level of the total proteome, KO cell degradation products were distinct from WT controls and featured peptides derived from the ubiquitin-conjugating enzyme activity family (Figures 3A and S3N–S3P; Table S2). Moreover, the overall number of detected products was higher in KO cells compared to WT controls (Figures 3B, 3C, and S3Q). Finally, FragPipe<sup>70,71</sup> analysis (Figures 3D, S3R, and S3S) of aberrant products identified five *trans*-frame and off-frame peptides ( $n = 3$  and  $n = 2$ , respectively, Table S2), three of which were exclusive to KO cells (Figure 3E; Table S2). Collectively, these data demonstrate that defects in translational fidelity caused by *TYW2* loss manifest as pronounced differences in the degradome and immunopeptidome.

### **Off-frame peptides induced by *TYW2* loss are immunogenic**

Off-frame peptides differ in their sequence from self-peptides, thus having an increased likelihood to elicit effective immune responses.<sup>72</sup> To examine whether aberrant peptides identified in *TYW2* KO cells are immunogenic, we co-cultured PBMCs from four healthy donors with autologous mature dendritic cells (DCs) loaded with aberrant peptides (Figure 4A, isolation i). T cell reactivity was then measured using flow cytometry analysis of 41BB, tumor necrosis factor alpha (TNF- $\alpha$ ), and interferon-gamma (IFN $\gamma$ ) expression, revealing that 5/11 examined aberrant peptides led to CD8<sup>+</sup> T cell activation upon stimulation (Figures 4B and S4A–S4G).

Next, we investigated the ability of DCs loaded with aberrant peptides to prime autologous naive CD8<sup>+</sup> T cells following short-term co-culture without any restimulation (Figure 4A, isolation ii).<sup>73–75</sup> The immunogenicity of aberrant peptides was compared to known neoepitopes encoded by shared mutations<sup>76,77</sup> and determined using specific peptide-major histocompatibility complex (MHC) multimers. Among six donors, we identified T cell populations recognizing two aberrant peptides in five (TTWDRPLTV) and three (LIDSGIRYL) donors (Figures 4C and S4H). In comparison, no populations were found reactive to the mutation-encoded neoantigens, demonstrating higher immunogenicity of the translation-aberrant peptides in these donors.

### ***Tyw2* loss impairs translation fidelity and leads to reduced tumor growth *in vivo***

We next tested the contribution of translation aberrations to immune surveillance *in vivo*. To this end, we first validated that

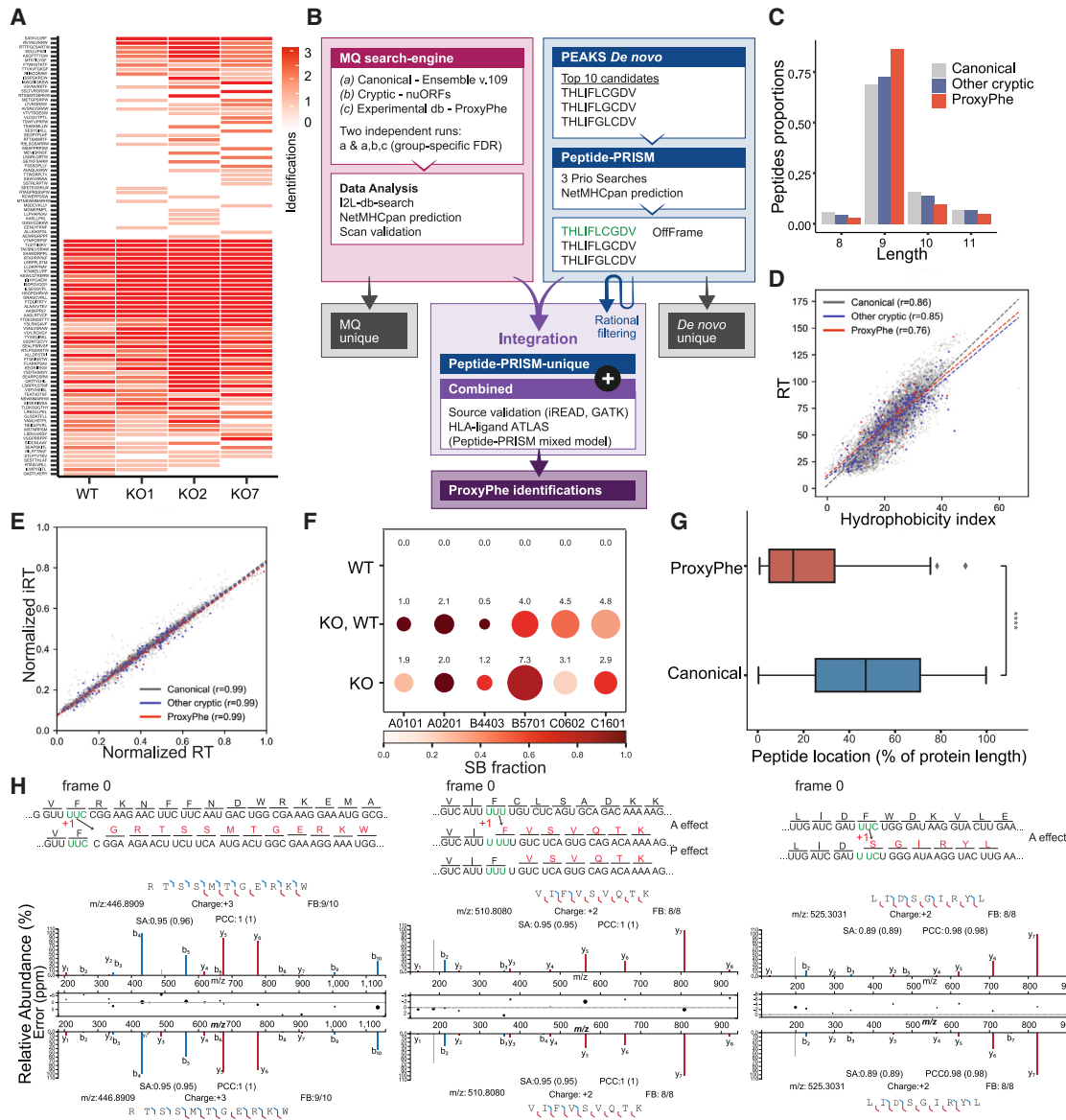


**Figure 2. Immunopeptidome analysis of TYW2 WT and KO cells**

(A) Heatmap of off-frame HLA-bound peptides in TYW2 WT or KO A375 cells ( $n = 3$  replicates per line). Color bar represents the number of replicates in which a peptide was identified by MS/MS.

(B) Schematic illustrating the analysis workflow used for the detection of ProxyPhe-peptides.

(C) Bar chart of the length distribution of canonical, ProxyPhe, and other cryptic peptides across all datasets.

(D) Scatterplot of retention time (RT) vs. hydrophobicity for canonical, ProxyPhe, and other cryptic peptides.

(E) Scatterplot of observed RT and predicted RT (iRT) for canonical, ProxyPhe, and other cryptic peptides.

(F) Dot plot of the enrichment of ProxyPhe-peptides ( $n = 64$ ) associated with HLA alleles in A375 TYW2 KO and WT samples. Dot size and numbers denote ProxyPhe HLA binders normalized to the amount of canonical HLA binders. Dot color reflects the strong binders (SB) fraction. Enrichment values were multiplied by  $10^3$ .

(G) Boxplot of the position of ProxyPhe ( $n = 23$ ) and canonical peptides ( $n = 6046$ ) identified in A375 clones along the normalized source protein length. \*\*\*\* $p = 1.515e-23$ , Mann-Whitney U test. Boxes represent the interquartile range and median peptide length, and the whiskers extend  $\pm 1.5$ -fold the interquartile range (dots correspond to individual peptides).

(H) Schematic illustrations of +1 out-of-frame (OOF) and trans-frame peptides identified in the immunopeptidome analyses (top). Red amino acids indicate +1 FS, black indicate canonical translation (i.e., frame 0). Green nucleotides indicate slippery-prone Phe codons. Mirror plots depict the ProxyPhe-peptide spectrum matches between experimentally identified (top) and synthetic peptides (bottom); PCC: Pearson correlation coefficient; SA, spectrum angle; FB, fragmented bonds).

See also [Figures S2](#) and [S3](#); [Table S1](#).

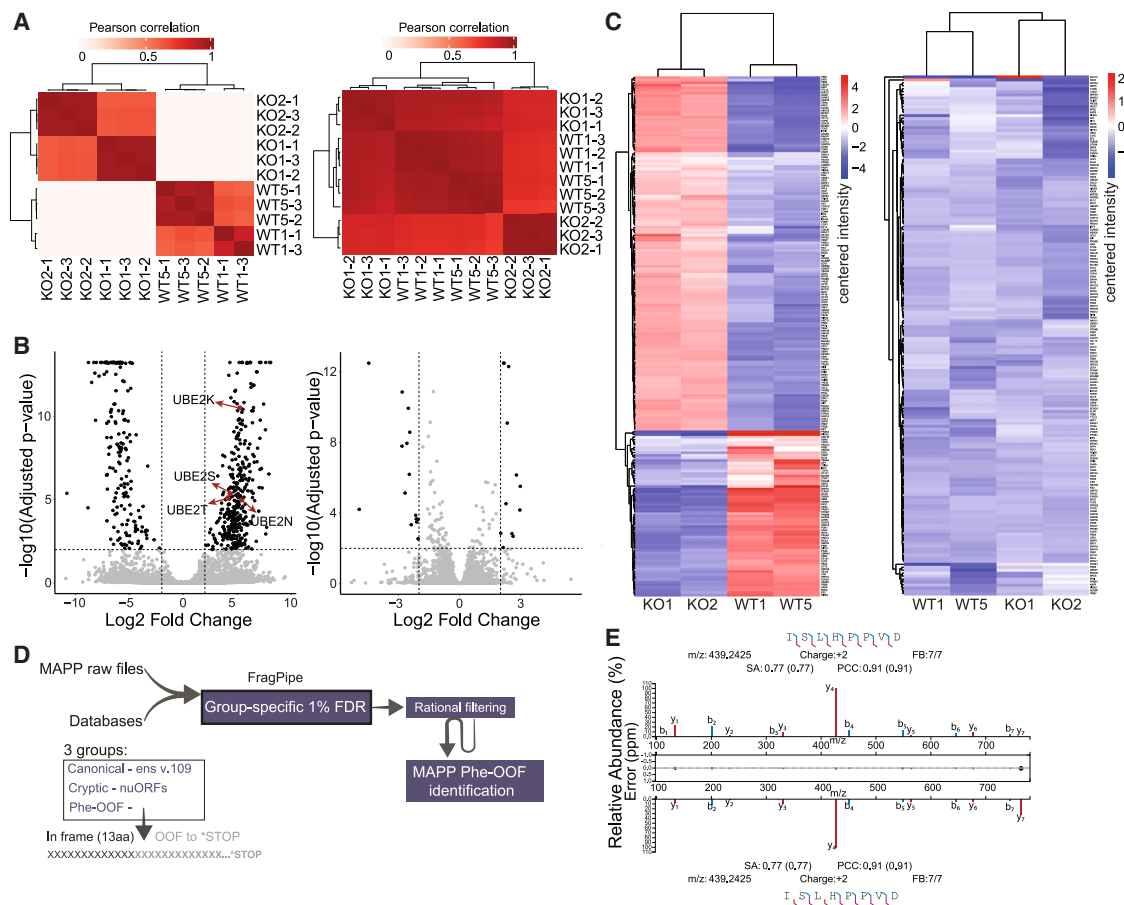


**Figure 3. Exploring the effects of TYW2 loss on the degradome**

(A) Heatmaps of pairwise Pearson correlation coefficient (PCC) between the peptides identified in each sample by MAPP (left) or whole-cell proteome (right).  
 (B) Volcano plot of peptides identified by MAPP (left) or whole-cell proteome (right). For the peptides highlighted in black, the log<sub>2</sub> fold change between KO and WT is  $-2 < X < 2$  and  $p \text{ adj.} < 0.01$  computed by limma linear model.<sup>97</sup> Peptides marked in red are associated with the “ubiquitin-like protein conjugating enzyme activity” or “ubiquitin-conjugating enzyme activity” pathways.  
 (C) Heatmap of peptides that were robustly (had the same trend in two WT or two KO clones) differentially abundant between TYW2 WT and KO samples by MAPP (left) or whole-cell proteomics (right). Color bar represents the centered intensity.  
 (D) Scheme depicting ProxyPhe-peptide search in the MAPP data.  
 (E) Representative mirror plot of a ProxyPhe aberrant peptide. Upper spectrum represents experimentally identified peptide; lower spectrum represents predicted peptide.

See also [Figure S3](#) and [Table S2](#).

murine *Tyw2* recapitulated the translation phenotype observed in human cells ([Figures S5A](#) and [S5B](#)). We then applied the CRISPR-Cas9 system to knock out *Tyw2* in the B2905 murine melanoma cells.<sup>78</sup> Given that genetic intratumor heterogeneity is a key factor in determining immune-mediated tumor eradication,<sup>79</sup> we set up a controlled experimental system where *Tyw2* is knocked out or endogenously expressed in isogenic, homogeneous cell lines ([Figure 5A](#)). Specifically, we generated single-cell-derived clones from the heterogeneous parental line, inoculated each clone into immunocompetent mice, and selected a clone that reproducibly exhibited increased growth after 2–3 weeks (clone4). Next, we transfected clone4 cells with CRISPR-Cas9 targeting *Tyw2* and established clonal lines. After validating *Tyw2* editing, we selected two *Tyw2* KO lines and a *Tyw2* WT line to use as an off-target control for CRISPR-Cas9 targeting. Dual fluorescence FS reporter analysis of these

clones demonstrated that PRF was enhanced in KO cells ([Figure 5B](#)), suggesting that murine *Tyw2* mirrors human TYW2 regulation of reading frame maintenance.

Next, we inoculated *Tyw2* WT and KO cells into immunocompetent mice and observed that both WT and clone4 parental cells grew aggressively unlike KO cells ([Figures 5C](#) and [S5C](#)). Notably, *Tyw2* overexpression in KO cells accelerated tumor growth and rescued ribosomal FS ([Figures 5D](#) and [S5D–S5F](#)), demonstrating that reduced tumor growth was caused by *Tyw2* loss. To assess the role of immune selection, we inoculated WT and KO cells into NOD-SCID gamma (NSG) and isogenic *Rag2* KO immunodeficient mice and observed no significant growth differences between WT and KO tumors ([Figures 5E](#), [S5G](#), and [S5H](#)). Together, these results demonstrate that *Tyw2* loss leads to anti-tumor immune responses *in vivo*.

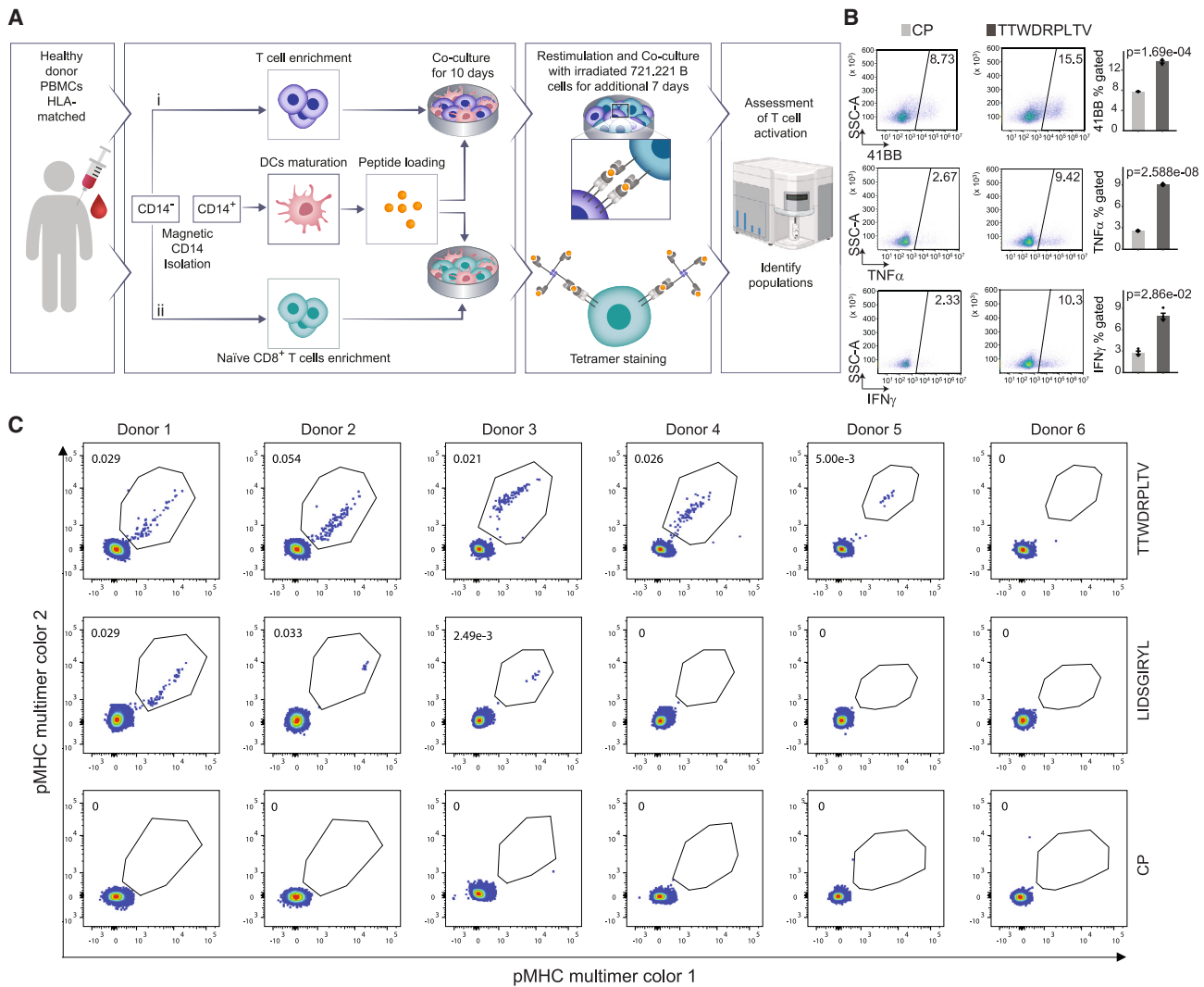


**Figure 4. Out-of-frame peptides induced by *Tyw2* loss are immunogenic**

(A) Overview of the two strategies used to assess the immunogenicity of peptides using PBMCs from healthy donors.

(B) Scatterplots of antigen-specific reactivity marker abundance in CD8<sup>+</sup> T cells measured using flow cytometry, following co-culture and restimulation described in (A), strategy i. Numbers indicate the percentage of gated events. Bar charts summarize mean fold change  $\pm$  SEM in 41BB, TNF- $\alpha$ , or IFN $\gamma$  abundance ( $n = 4$  biological replicates). Exact  $p$  values from Welch two-sample  $t$  test or Mann-Whitney U test. CP, control peptide.

(C) CD8<sup>+</sup> T cell populations stained with relevant dual-colored peptide-MHC (pMHC) multimers following co-culture of naive CD8<sup>+</sup> T cells with autologous DCs loaded with indicated aberrant peptides or CP (A, strategy ii). Numbers indicate percentage of events gated as shown in Figure S4H.

See also Figure S4.

### CD8<sup>+</sup> T cell reactivity against *Tyw2* KO tumors

To examine the role of CD8<sup>+</sup> T cell-mediated anti-tumor immunity in *Tyw2* KO tumor regression, we inoculated mice with *Tyw2* KO or WT cells after CD8<sup>+</sup> depletion (Figures 5F and S5I–S5K). KO tumor growth was enhanced after CD8<sup>+</sup> depletion compared to isotype control, while WT tumor growth was unaffected (Figure 5F). These results suggest that *Tyw2* KO tumor growth is controlled in a CD8<sup>+</sup> T cell-dependent manner. We next isolated CD8<sup>+</sup> T cells from naive mice, labeled them with carboxyfluorescein-succinimidyl ester (CFSE) to monitor proliferation, and co-cultured them with DCs pre-loaded with tumor cell lysates (TCLs) from *Tyw2* WT or KO cells (Figure 5G). This analysis revealed that T cells cultured in the presence of DCs

loaded with *Tyw2* KO TCLs were more proliferative (Figures 5H and S5L).

To examine whether MHC-I-bound aberrant peptides contribute to CD8<sup>+</sup> T cell reactivity against *Tyw2* KO tumors, we performed immunopeptidome analysis of bone-marrow-derived DCs (BMDCs) loaded with either *Tyw2* KO or WT TCLs (Figures 5G, S5M, and S5N). Intriguingly, BMDCs loaded with KO TCLs had a distinct MHC-I ligand repertoire at the canonical peptide level (Figures 5I and S5O–S5Q). Furthermore, ProxyPhe-peptide search revealed 21 robustly identified aberrant peptides, 11 of which were KO-specific compared to the single identified WT-specific peptide (Figures 5J, 5K, and S5R–S5T; Table S3). Notably, none of the aberrant peptides were

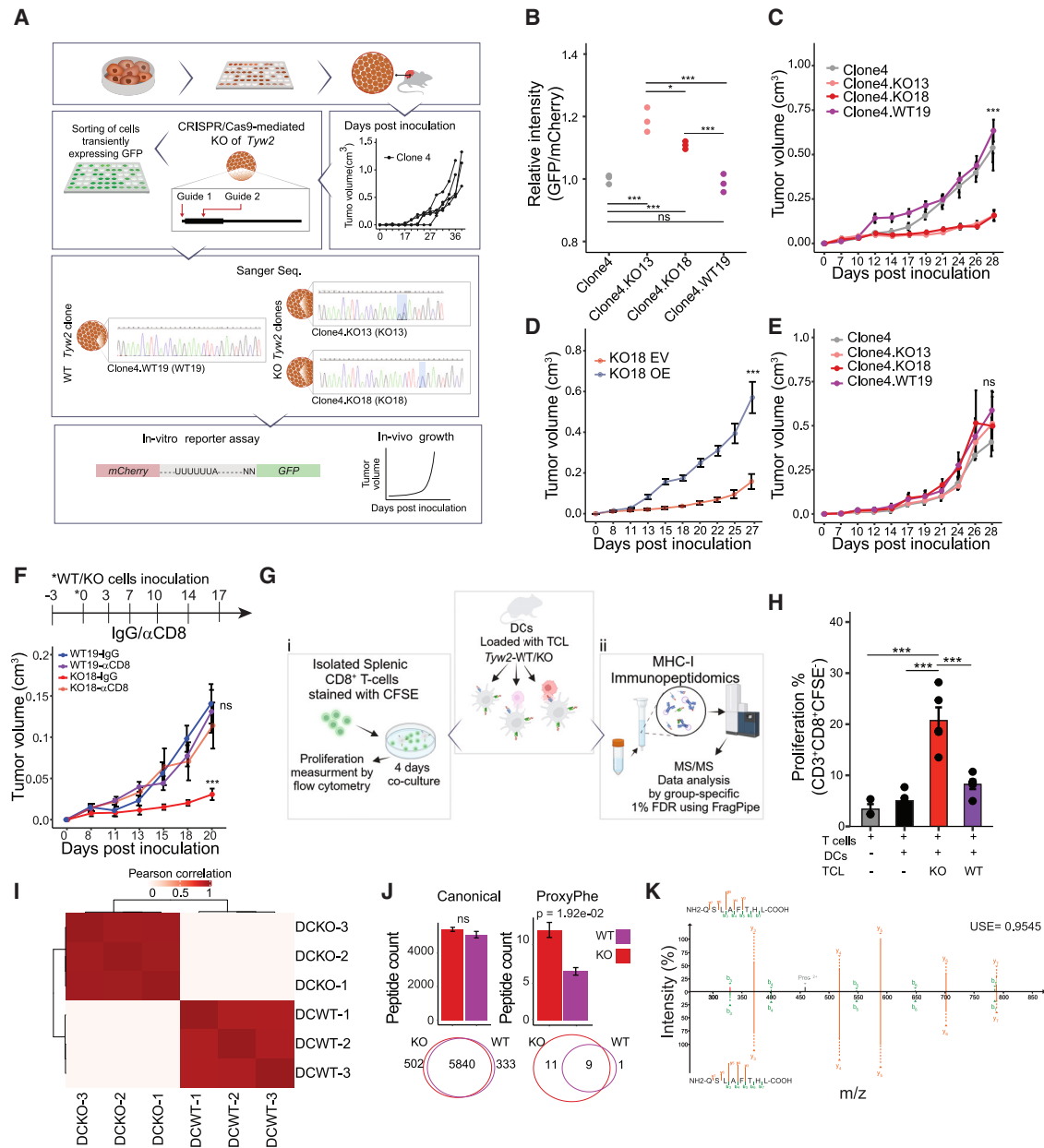


**Figure 5. Effect of *Tyw2* loss on tumor growth and MHC-I peptide presentation**

(A) Schematic describing the generation of a murine *Tyw2* KO-controlled cell line system.

(B) Scatterplot of the relative fold change in mean GFP/mCherry expression in parental clone4 and *Tyw2* WT or KO cells transfected with the -1 FS construct (normalized to clone4;  $n = 3$  biological replicates per cell line). ns, not significant,  $0.05 < p < 0.001$ ,  $***p < 0.001$ , one-way ANOVA with post hoc Tukey HSD test.

(C) *In vivo* tumor growth following inoculation of clone4 or *Tyw2* WT or KO tumor cells into C57BL/6 mice ( $n = 10$  mice per cell line). Data are presented as mean  $\pm$  SEM.  $p = 8.62e-7$ , Kruskal-Wallis test.  $***p < 0.001$ , Holm-corrected pairwise Wilcoxon test.

(D) *In vivo* tumor growth following inoculation of KO18 cells overexpressing WT *Tyw2* (OE; KO18 OE) or control empty vector (KO18 EV) into C57BL/6 mice ( $n = 8$  mice per cell line). Data are presented as mean  $\pm$  SEM.  $p = 7.78e-4$ , Kruskal-Wallis test.  $***p < 0.001$ .

(E) *In vivo* tumor growth following inoculation of clone4 or *Tyw2* WT or KO cells into NSG mice ( $n = 4$  mice per cell line). Data are presented as mean  $\pm$  SEM.  $p = 0.7154$ , pairwise Wilcoxon test. ns, not significant.

(F) *In vivo* tumor growth following inoculation of KO18 or WT19 cells into C57BL/6 mice after treatment with anti-CD8 or IgG isotype control antibodies ( $n = 5$  mice per group). Treatment regimen summarized above. Data are presented as mean  $\pm$  SEM.  $p = 8.65e-3$ , Kruskal-Wallis test.  $***p < 0.001$ , Bonferroni-corrected pairwise Wilcoxon test.

(G) Schematic of *Tyw2* KO and WT tumor cell lysate (TCL) experiments.

(H) Bar plot of proportions of proliferative CD8<sup>+</sup> T cells after co-culture with untreated DCs and DCs loaded with *Tyw2* WT or KO TCLs ( $n = 3$  for T cell-only condition,  $n = 5$  for all other conditions) determined by CFSE dilution, measured using flow cytometry.  $p = 1e-5$ , one-way ANOVA.  $***p < 0.001$ , post hoc Tukey HSD test. Data are presented as mean  $\pm$  SEM.

detected in unloaded-BMDCs control, suggesting that they were cancer specific (Table S3).

To test the immunogenicity of the KO-specific aberrant peptides, we isolated splenocytes from mice immunized with ten aberrant peptides and evaluated peptide-specific CD8<sup>+</sup> T cell cytotoxic reactivity compared to non-immunized controls, following *ex vivo* re-stimulation with each of the peptides or with a non-relevant peptide control (SIINFEKL). Half of the examined peptides elicited T cell responses in immunized mice, with one peptide, YAPANGDFTL, demonstrating the highest immunogenicity (Figures S5U and S5V). Next, we tested the ability of CD8<sup>+</sup> T cells from immunized mice to elicit reactivity upon co-culture with *Tyw2* KO or WT cells. Even without the external addition of peptides, CD8<sup>+</sup> T cells from immunized mice demonstrated higher reactivity towards KO cells (Figures S5W and S5X). Together, these results suggest that immunological control of *Tyw2* KO tumors may involve CD8<sup>+</sup> T cell responses to non-mutated, translationally aberrant antigens.

### Increased T cell infiltration and exhaustion are associated with *Tyw2* loss

The CD8<sup>+</sup> T cell-dependent differential growth of *Tyw2* KO vs. WT tumors suggests that they feature distinct immune TMEs. To explore this, we inoculated *Tyw2* WT and KO clones into immunocompetent mice and used single-cell RNA sequencing (scRNA-seq) to profile the TME at two time points (18 and 21 days post inoculation, respectively), during which WT and KO tumors exhibited distinct growth dynamics (Figure 6A). We used MULTI-seq<sup>80</sup> to barcode pooled WT and KO tumors at each time point ( $n = 4\text{--}5$  tumors per sample) and performed multiplexed scRNA-seq analysis of CD45<sup>+</sup> immune cells (Figure 6B). Unsupervised clustering and differential gene expression analysis led to the identification of major adaptive immune lineages, such as CD4<sup>+</sup> and CD8<sup>+</sup> T cells, innate lymphoid cells (ILCs), natural killer (NK) cells, regulatory T cells (Tregs), and B cells as well as myeloid lineages such as DCs and monocytes/macrophages (Figures 6C and S6A).<sup>81,82</sup>

Next, we quantified the TME immune population structure in each sample to identify populations associated with anti-tumor immune responses (Figures S6B and S6C). This analysis revealed that CD8<sup>+</sup> T cell proportions increased 1.9-fold between day 18 and day 21 in KO tumors while remaining relatively unchanged in WT tumors (Figure 6D). We next annotated and quantified CD8<sup>+</sup> T cell subtypes, which revealed the presence of naive, memory-like, effector-like, progenitor exhausted (Tpex), exhausted (Tex), and proliferative CD8<sup>+</sup> T cells (Figures 6E, 6F, S6D, and S6E).<sup>83,84</sup> Among these CD8<sup>+</sup> T cells, WT and KO tumors were associated with altered abundances of memory-like and Tex CD8<sup>+</sup> T cells at day 21 (Figure 6G). Specifically, Tex proportions increased 2.5-fold between day 18 and day 21 in KO tumors (vs. 1.8-fold decrease in WT), while memory-like propor-

tions increased 1.4-fold in WT tumors (vs. 1.8-fold decrease in KO; Figure 6H).

CD8<sup>+</sup> T cell exhaustion is associated with elevated and persistent antigen stimulation that induces the co-expression of inhibitory checkpoint receptors (Figure 6I).<sup>84</sup> Thus, these observations, together with the immunopeptidome analyses demonstrating the *Tyw2* loss-dependent increase in aberrant peptide presentation, suggest that CD8<sup>+</sup> T cell stimulation and activation were increased in the *Tyw2* KO TME. Supporting this notion, CODEX<sup>85</sup> analysis of WT and KO tumors demonstrated that total, LAG3<sup>+</sup>-exhausted, and KI67<sup>+</sup> proliferative CD8<sup>+</sup> T cell proportions were all increased in KO tumors at day 21 (Figures 6J and S6F). Moreover, CellChat<sup>86</sup> analysis revealed that pro-inflammatory IFN $\gamma$ -IFNGR1/2 signaling between CD8<sup>+</sup> T cells and myeloid cells was specifically active in day 21 KO tumors (Figure 6K). NK cell cytotoxicity was also inhibited in WT tumors but remained consistent over time in KO tumors (Figures S6G and S6H), reflecting the increased inflammatory nature of the *Tyw2* KO TME.

### Murine *Tyw2* loss enhances the response to immune checkpoint blockade

Given the T cell exhaustion signature observed in *Tyw2* KO TME, we hypothesized that *Tyw2* KO tumor-bearing mice would benefit from immune checkpoint blockade (ICB) therapy. To test this, we treated *Tyw2* KO or WT tumors with an anti-programmed cell death 1 (PD-1) antibody when mice first formed palpable tumors or when tumors grew to  $\sim 0.05\text{ cm}^3$  (Figure 7A). While anti-PD-1 treatment did not impact WT tumor growth, it significantly delayed KO tumor growth (Figures 7B and S7A–S7E), with 40% of the mice being tumor-free or bearing  $<0.05\text{ cm}^3$  tumors 50 days post inoculation (Figures 7C–7E, S7F, and S7G).

Next, we tested whether T cells from anti-PD-1-treated mice were reactive toward *Tyw2* KO-specific Proxyphe-identified peptides that demonstrated immunogenicity ( $n = 5$ , Figure S5V). To this end, we isolated splenic CD8<sup>+</sup> T cells from mice 27 days post inoculation, labeled them with CFSE, cultured them with DCs preloaded with the aberrant peptides, and measured media IFN $\gamma$  concentration and T cell proliferation (Figure S7H). We observed reactivity against 3/5 examined peptides, and responses were particularly strong against the YAPANGDFTL peptide (Figures 7F, S7I, and S7J). Further, CD8<sup>+</sup> T cells from the draining lymph node of *Tyw2* KO tumor-bearing mice demonstrated high reactivity against YAPANGDFTL (Figures S7K and S7L). These results provide evidence that endogenous presentation of aberrant peptides is sufficient to trigger *de novo* antigen-specific T cell responses in *Tyw2* KO-bearing mice.

### TYW2 expression is associated with melanoma patient survival and ICB response

Having demonstrated the role of *Tyw2* loss in driving anti-tumor immunity in mice, we next investigated its clinical relevance.

(I) Heatmap of pairwise Pearson correlation coefficient (PCC) of MHC-I peptide presentation by BMDCs loaded with *Tyw2* KO and WT TCLs.

(J) Bar plots of filtered peptide counts for canonical (left) and Proxyphe (right) identifications in BMDCs loaded with *Tyw2* WT or KO TCLs (top;  $n = 3$  replicates per group). Data are presented as mean  $\pm$  SEM. Venn diagrams summarize intersecting peptides in each group (bottom). Indicated  $p$  values computed with Welch two-sample  $t$  test. ns, not significant.

(K) Representative mirror plot of a *trans*-frame peptide uniquely identified in the *Tyw2* KO TCL-loaded sample. Unweighted spectral entropy (USE) is shown. Upper spectrum: experimentally identified peptide; lower spectrum: predicted peptide.

See also Figure S5; Table S3.

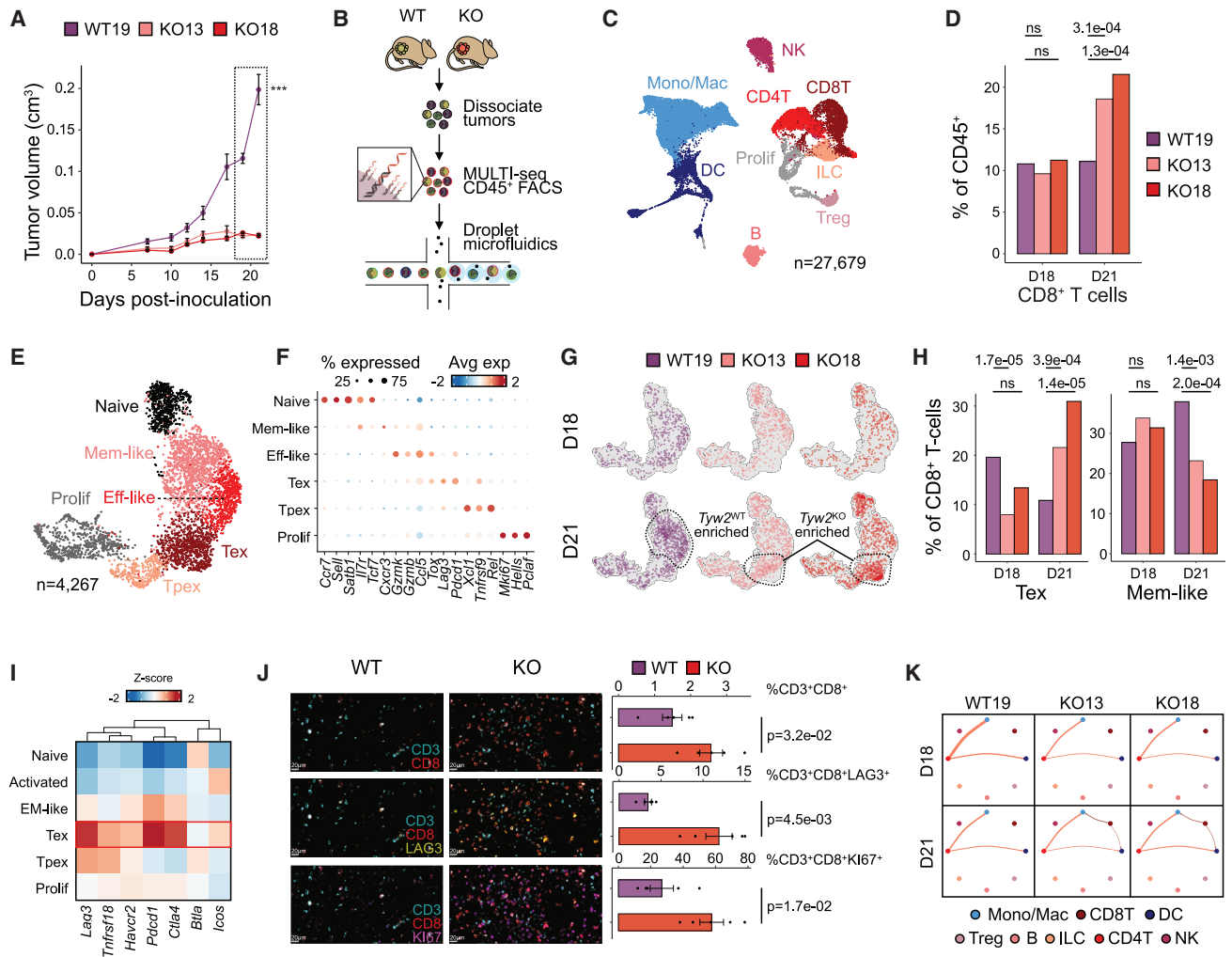


**Figure 6. Longitudinal scRNA-seq analysis of tumor immune compartment reveals anti-tumor CD8<sup>+</sup> T cell responses linked to *Tyw2* KO**

(A) *In vivo* tumor growth following inoculation of WT19, KO13, or KO18 cells into C57BL/6 mice. Time points highlighted with dotted box were used for scRNA-seq analysis. \*\*\**p* < 0.001, pairwise Bonferroni-corrected Student's *t* test.

(B) Schematic overview of experimental workflow. Tumors were removed and dissociated at day 18 and day 21 prior to MULTI-seq barcoding, enrichment for CD45<sup>+</sup> immune cells, and scRNA-seq.

(C) Uniform manifold approximation and projection (UMAP) of immune gene expression space colored by cell type.

(D) Bar charts of the percentage of CD8<sup>+</sup> T cells among all CD45<sup>+</sup> cells in each tumor background at day 18 (D18) and day 21 (D21). Statistically significant changes denoted with propeller test *p* values (ns, not significant; *n* = 3 sets of 4–5 pooled tumors).

(E) UMAP of CD8<sup>+</sup> T cell gene expression space colored by subtype.

(F) Dot plot of CD8<sup>+</sup> T cell subtype annotation genes. Dot color indicates expression level and size indicates the proportion of cells expressing each gene.

(G) UMAP of CD8<sup>+</sup> T cell gene expression space colored by sample identities on day 18 (top) and day 21 (bottom). Regions of gene expression space that are enriched in *Tyw2* KO or WT samples highlighted with dotted circles.

(H) Bar charts of the percentage of exhausted and memory-like CD8<sup>+</sup> T cells among all CD8<sup>+</sup> T cells in each tumor background at day 18 and day 21. Statistically significant changes denoted with propeller test *p* values (ns, not significant; *n* = 3 sets of 5 pooled tumors).

(I) Z score heatmap of the average expression of immunosuppression markers in CD8<sup>+</sup> T cell subtypes. Z scores for each gene clustered using hierarchical clustering. Exhausted CD8<sup>+</sup> T cells highlighted with red box.

(J) Representative images of the day 21 *Tyw2* KO and WT TME with bar charts of mean ± SEM total (top), exhausted (middle), and proliferative CD8<sup>+</sup> T cell percentages (bottom). Exact *p* values from Welch two-sample *t* test (*n* = 5 mice per tumor background).

(K) Weighted network graph of IFNG-IFNGR1/IFNGR2 predicted signaling interactions split by tumor background and time point. Nodes colored by cell type, edges weighted by signaling probability and colored by sender cell type.

See also Figure S6.

First, we examined the relationship between *TYW2* expression levels and melanoma patient survival and found that lower *TYW2* expression was associated with improved progression-

free survival (PFS) in patients with primary melanoma in The Cancer Genome Atlas (TCGA) cohort (Figure 8A). Patients with higher *TYW2* expression also tended to have worse overall

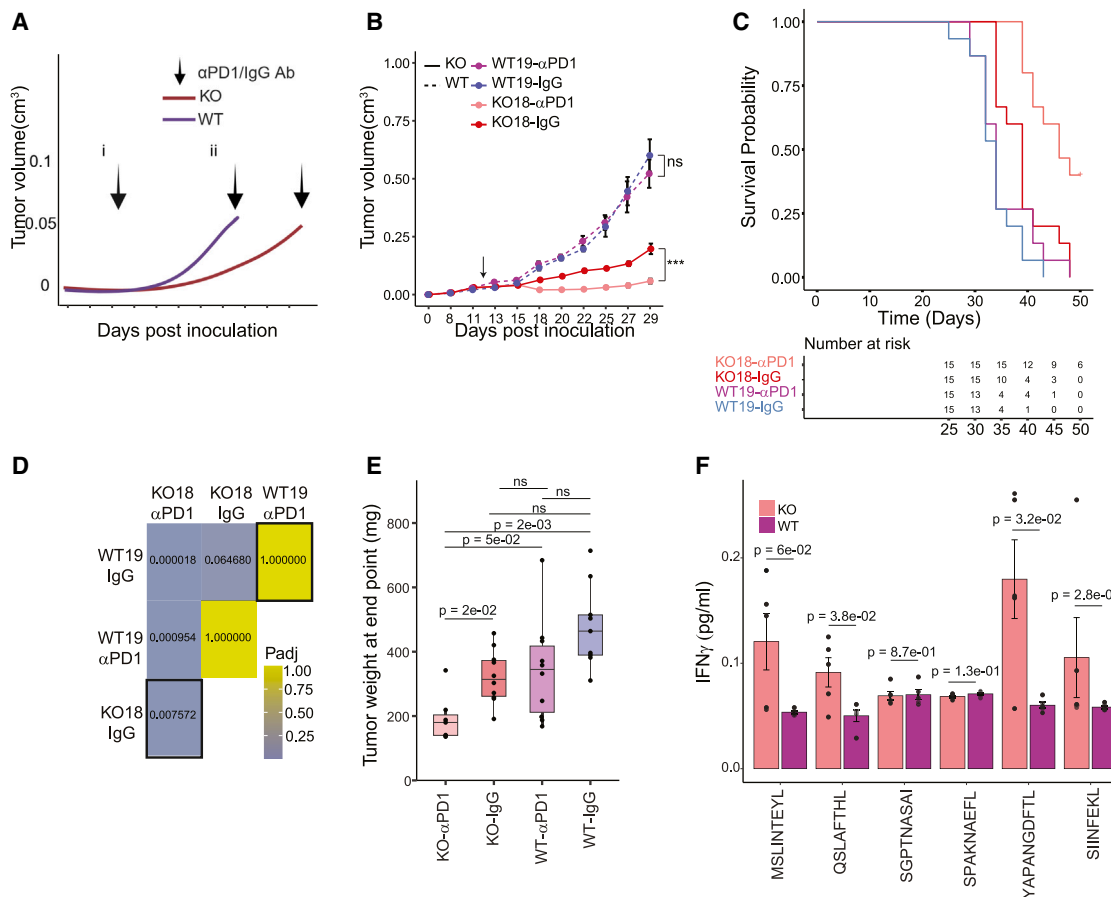


**Figure 7. Anti-PD-1 therapy delays *Tyw2* KO tumor growth**

(A) Schematic representation of experimental design. Antibodies were administered when tumors were palpable (i) or when tumor volume reached  $\sim 0.05$  cm<sup>3</sup> (ii). (B) *In vivo* tumor growth following inoculation of KO18 or WT19 cells into C57BL/6 mice after treatment with anti-PD-1 or IgG isotype control antibodies (as in Ai; arrow marks treatment onset;  $n = 10$  mice per group). Data are presented as mean  $\pm$  SEM. ns, not significant,  $***p < 0.001$ , pairwise Wilcoxon test with Bonferroni correction.

(C) Kaplan-Meier (KM) curves of survival probability between KO18 or WT19 tumor-bearing mice  $\pm$  anti-PD-1 treatment ( $n = 15$  mice per group, two independent experiments combined).

(D) Heatmap of Bonferroni-corrected  $p$  values for survival experiment obtained by  $p$  log-like model.

(E) Boxplots of tumor weight at endpoint in KO18 or WT19 tumor-bearing mice  $\pm$  anti-PD-1 treatment ( $n = 10$  mice per group). Boxes represent the interquartile range and median tumor weight, and the whiskers extend  $\pm 1.5$ -fold the interquartile range (dots correspond to individual mice). Exact  $p$  values from Bonferroni-corrected  $t$  tests. ns, not significant.

(F) Bar charts of media IFN $\gamma$  concentration following 16 h CD8<sup>+</sup> T:DCs co-culture ( $n = 5$  replicates per peptide; as described in Figure S7H). Exact  $p$  values from Bonferroni-corrected  $t$  tests. Data are presented as mean  $\pm$  SEM.

See also Figure S7.

survival (OS), although the association was not statistically significant (Figure S8A).

Next, we examined the relationship between *TYW2* expression levels and ICB response and found that *TYW2* expression in the TME was predictive of ICB response in on-treatment samples in the Riaz et al.<sup>87</sup> cohort (Figure 8B) and, to a lesser extent, pre-treatment samples (Figure 8B). Further, lower *TYW2* expression was correlated with improved OS with a stronger effect observed in on-treatment samples (Figure 8C) compared to pre-treatment samples (Figure S8B).

Importantly, the predictive signal of *TYW2* expression was independent of TMB levels (Figure S8C). Furthermore, *TYW2* expression strongly predicted patient outcomes within the low-TMB group of on-treatment samples (Figure 8D). For pre-treatment

samples, the hazard ratio (HR) was 3.05 but was not statistically significant (Figure S8D). Assessment of two additional melanoma patient cohorts from Cabrita et al.<sup>88</sup> and Auslander et al.<sup>89</sup> mirrored these results, as lower *TYW2* expression correlated with PFS following ICB therapy in the Cabrita et al.<sup>88</sup> cohort (Figure 8E) and with ICB response in the Auslander et al.<sup>89</sup> cohort (Figure 8F).

Next, we assessed how additional genes that were differentially expressed between *TYW2*-high and *TYW2*-low samples contributed to patient outcome predictions. To this end, we performed differential expression analysis among TCGA samples grouped by *TYW2* expression level. Notably, *TYW2*-low tumors were associated with elevated expression levels of genes associated with immune activation in the TME (e.g., *IL32*, *IL21R*, *CCL5*, *CXCR3*, *CD3E*, and *CR2*), and *TYW2* itself emerged as

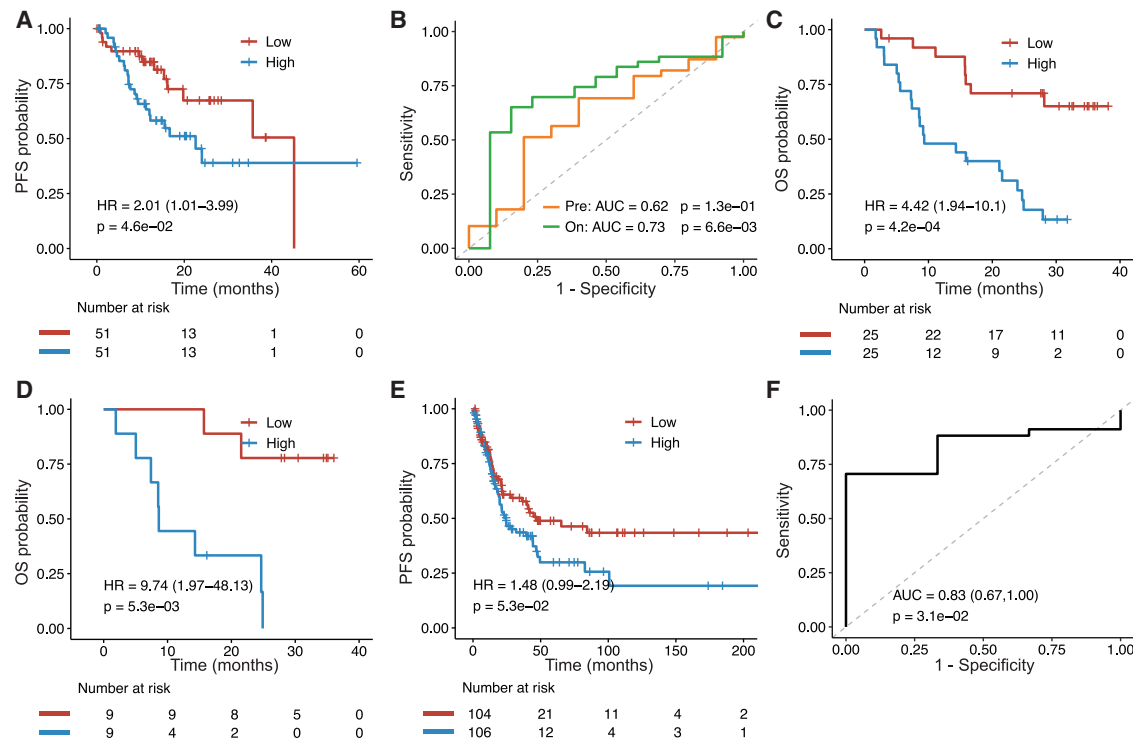


**Figure 8. TYW2 expression is negatively associated with patient prognosis and ICB response**

(A) Kaplan-Meier curves of progression-free survival (PFS) for patients with low versus high TYW2 expression in the TCGA primary melanoma cohort ( $n = 102$ ). Indicated  $p$  value and HR from univariable Cox model. TYW2 expression binarized at the 50th percentile.

(B) Receiver operating characteristic (ROC) curves and area under the curve (AUC) values for predicting objective response to ICB (measured by RECIST criteria) in pre-treatment ( $n = 49$ ) or on-treatment subsets ( $n = 56$ ) in the Riaz et al.<sup>87</sup> cohort using TYW2 expression. Indicated  $p$  values from two-tailed DeLong's test.

(C) Kaplan-Meier curves of overall survival (OS) following ICB therapy for patients with low versus high on-treatment TYW2 expression in the Riaz et al.<sup>87</sup> cohort ( $n = 50$ ). Indicated  $p$  value and HR from univariable Cox model.

(D) Kaplan-Meier curves of OS following ICB therapy for patients with low versus high on-treatment TYW2 expression in low-TMB patients in the Riaz et al.<sup>87</sup> cohort ( $n = 18$ ). Indicated  $p$  value and HR from univariable Cox model.

(E) Kaplan-Meier curves of PFS following ICB therapy for patients with low versus high TYW2 expression in the Cabrita et al.<sup>88</sup> cohort ( $n = 210$ ). Indicated  $p$  value and HR from univariable Cox model.

(F) ROC curve and AUC for predicting objective response to ICB (measured by RECIST criteria) using TYW2 expression in the Auslander et al.<sup>89</sup> cohort ( $n = 37$ ). Indicated  $p$  value from two-tailed DeLong's test.

See also [Figure S8](#); [Table S4](#).

the top-ranked gene for predicting patient outcomes ([Figures S8E](#) and [S8F](#); [Table S4](#)). Further, we found that low TYW2 expression was linked to increased CD8<sup>+</sup> T cell infiltration and heightened cytolytic and exhausted activity in the tumor ([Figures S8G–S8O](#)). Overall, these findings underscore the critical role of TYW2 in anti-tumor immunity and cancer immunotherapy, extending beyond mouse models to diverse clinical settings.

## DISCUSSION

Immunotherapies targeting mutation-derived neoantigens have had limited success for numerous reasons, including the small percentage of about only ~1% of somatic mutations that are shared across patients<sup>90</sup> and low-TMB patients that lack identifiable targetable antigens.<sup>91</sup> Hence, expanding the neoantigen search to non-mutational sources could greatly increase immunotherapy applications.

Various mechanisms may drive aberrant peptide presentation in tumors. Particularly, the “addiction” of cancer cells to dysre-

gulated translation<sup>29,35</sup> positions non-canonical translation as an attractive source of non-mutational cancer neoantigens.<sup>92,93</sup> Given the intimate relationship between mRNA translation and antigen presentation,<sup>94,95</sup> we hypothesized that loss of a single *trans*-acting factor regulating translational fidelity could generate a range of tumor-specific immunogenic peptides. To test this concept, we studied how deleting the tRNA-modifying enzyme TYW2<sup>46,54</sup> influences aberrant peptide generation, tumor recognition, and immune-mediated tumor elimination.

We established a controlled system to compare the generation and presentation of aberrant peptides in TYW2 KO cells. Ribosome profiling revealed pauses at Phe codons, suggesting a delay in decoding, and immunopeptidome analyses of these cells identified a set of immunogenic FS peptides uniquely presented by KO cells. Furthermore, *Tyw2* KO tumors showed CD8<sup>+</sup> T cell-mediated tumor control *in vivo*, and *Tyw2* KO tumor-bearing mice exhibited a superior response to ICB compared to *Tyw2* WT tumor-bearing mice, indicating the involvement of antigen-specific anti-tumor responses. Importantly, stimulation of T cells from

ICB-treated *Tyw2* KO tumor-bearing mice with off-frame peptides induced antigen-specific proliferation and activation in different *ex vivo* assays. Finally, our observations were corroborated by primary melanoma patient data showing that lower *TYW2* expression was associated with improved OS after ICB therapy in low-TMB patients, which addresses an important unmet clinical need. Taken together, this study highlights the potential of tumor translational regulators as an attractive target for immunotherapy development, for enhancing the repertoire of tumor neoantigens.

### Limitations of the study

First and foremost, pharmacological agents that inhibit TYW2 in tumor cells have not been described, limiting the immediate translational horizon of our work. However, we believe that the results shown above will stimulate future efforts to design TYW2 inhibitors. Second, future studies will be needed to establish whether these results can be recapitulated in other cancer types. Finally, this study explored a single tRNA-modifying enzyme as a proof of concept. Whether perturbing other translational fidelity regulators can drive anti-tumor immune responses *in vivo*, and perhaps even to a larger extent, remains an interesting open area of research.

### RESOURCE AVAILABILITY

#### Lead contact

Requests for further information, resources, and reagents should be directed to and will be fulfilled by the lead contact, Yardena Samuels ([Yardena.Samuels@weizmann.ac.il](mailto:Yardena.Samuels@weizmann.ac.il)).

#### Materials availability

All plasmids and cell lines are available upon request.

#### Data and code availability

The mass spectrometry proteomic data have been deposited to the ProteomeXchange Consortium via the PRIDE<sup>96</sup> partner repository with the dataset identifier PXD053256 and are publicly available. Bulk RNA-seq (BioProject: ID#PRJNA1045112) and Ribo-seq (BioProject: ID#PRJNA1045083) data were deposited to the BioProject, and single-cell RNA-seq data (GEO: GSE272996) were deposited in GEO and are publicly available. Data from public repositories were accessed from the Gene Expression Omnibus with accession numbers GEO: GSE91061 (the Riaz et al.<sup>87</sup> cohort), GEO: GSE65904 (the Cabrita et al.<sup>88</sup> cohort), and GEO: GSE115821 (the Auslander et al.<sup>89</sup> cohort) and from the TCGA data portal SKCM (<https://portal.gdc.cancer.gov/projects/TCGA-SKCM>; the TCGA primary melanoma cohort). Gene expression counts data from TCGA were obtained from the GDC Xena Hub ([https://xenabrowser.net/datapages/?dataset=TCGASKCM.htseq\\_counts.tsv&host=https%3A%2F%2Fgdc.xenahubs.net&removeHub=https%3A%2F%2Fxcna.treehouse.gi.ucsc.edu%3A443](https://xenabrowser.net/datapages/?dataset=TCGASKCM.htseq_counts.tsv&host=https%3A%2F%2Fgdc.xenahubs.net&removeHub=https%3A%2F%2Fxcna.treehouse.gi.ucsc.edu%3A443)).

The pipeline and scripts used for the immunopeptidome analysis and figures can be found on GitHub: <https://github.com/YSamuelsLab/MetaPept2>. Single-cell RNA-seq original code has been deposited into Zenodo (<https://doi.org/10.5281/zenodo.12802673>) and is available on GitHub: [https://github.com/chris-mcgininis-ucsf/tyw2\\_neoantigen](https://github.com/chris-mcgininis-ucsf/tyw2_neoantigen). Processed single-cell RNA-seq data and R scripts used for analyzing data and generating Figures 6 and S6 are deposited onto Synapse: [synapse.org/Synapse:syn61841510](https://synapse.org/Synapse:syn61841510). All raw data, supplementary files, code, and any additional information required to re-analyze the data reported in this study are available from the lead contact upon request.

### ACKNOWLEDGMENTS

Y. Samuels is supported by the Israel Science Foundation grant no. 2133/23, the European Research Council (ERC) under the European Union's Horizon

2020 research and innovation programme (#770854), the European Union (#101094980), MRA (#917324), the Minerva Stiftung with the funds from the BMBF of the Federal Republic of Germany, the ICRF (20-802-ICG), and the Intramural Research Program of the NIH, NCI. Y. Samuels is the incumbent of the Knell Family Professorial Chair and is the Head of the Moross Integrated Cancer Center (MICC), de-Picciotto-Lesser Cell Observatory unit at MICC. S.G. is supported by the Sheba-Talpiot Medical Program. D.M. is supported by the Israeli Ministry of Aliyah and Integration. C.S.M. is a Cancer Research Institute Irvington Fellow (CRI Award #4134) and a Parker Institute for Cancer Immunotherapy Scholar. A.T.S. is supported by a Career Award for Medical Scientists from the Burroughs Wellcome Fund, a Lloyd J. Old STAR Award from the Cancer Research Institute, a Pew-Stewart Scholars for Cancer Research Award, and the Parker Institute for Cancer Immunotherapy. J.O. is supported by the Research Council of Norway through its Centers of Excellence scheme, #332727, and through grant #316060, and by the Norwegian Cancer Society grant #216135-2020, South-Eastern Regional Health Authority Norway #2021074, ERC under the European Union's Horizon 2020 research and innovation programme (#865805), and Novo Nordisk Foundation. A.R.B. was supported by NIH grant GM136960. T.S. was supported by the Exploratory Research for Advanced Technology (ERATO, JPMJER2002) program from JST.

### AUTHOR CONTRIBUTIONS

Y. Samuels, O.B., and C.W. designed the study, performed the experiments, supervised the project, and wrote the paper. C.S.M. edited the paper. C.S.M., W.Y., and A.T.S. generated and analyzed scRNA-seq data. D.M., D.H., B.E.A., S.G., D.A., P.K., and J.C. analyzed RNA-seq and immunopeptidomic data. P.G. and N.G. performed immunopeptidomics. J.O., H.P., S.S., M.M.N., and W.Y. performed immunogenicity experiments and co-wrote the paper. Y.L. performed MS analyses. S.B.-D. designed CRISPR experiments. S.B.-H., M.Z., and R.O. performed mouse experiments. M.R. and P.P. assessed frameshifting mechanisms. S.C.S., A. Nagler, and E.P.-K. derived cell clones. K.L. provided conceptual insights. G.B. performed HLA typing. A.R.B. performed Ribo-seq analyses. T.S., A. Nagao, A.M., and Y. Sakaguchi assessed tRNA<sup>Phe</sup> modification and aminoacylation status. Y.P. designed PRF reporter experiments. F.E. and A.S. analyzed Ribo-seq and immunopeptidomic data. Y.C. and A.K. performed *ex vivo* experiments. M.D.S. and Y.M. performed MAPP. M.J.Z. performed CODEX imaging. T.-G.C. and E.R. performed patient data analyses. All authors read and approved the manuscript.

### DECLARATION OF INTERESTS

Y. Samuels, O.B., and C.W. hold patents related to TYW2. C.S.M. holds patents related to MULTI-seq. A.T.S. is a founder of Immunai, Cartography Biosciences, Santa Ana Biosciences, and Prox Biosciences, an advisor to 10x Genomics and Wing Venture Capital, and receives research funding from Merck Research Laboratories and Astellas Pharma. E.R. is a divested co-founder of Pangea Biomed and is a non-paid member of the scientific advisory boards of Pangea Biomed and GSK oncology.

### STAR★METHODS

Detailed methods are provided in the online version of this paper and include the following:

- KEY RESOURCES TABLE
- EXPERIMENTAL MODEL AND STUDY PARTICIPANT DETAILS
  - Cell culture
  - Mice
  - Healthy donors for PBMC extraction
- METHOD DETAILS
  - HLA-typing of healthy donor PBMCs
  - CRISPR-Cas9 mediated KO for *TYW2*
  - Immunoprecipitation assay and western blot analysis
  - MS shotgun analysis of tRNA<sup>Phe</sup> from the cells
  - Lentiviral production, mutagenesis, and viral transduction
  - PRF reporter assay
  - Bulk RNA-sequencing

- Ribosome profiling
- tRNA charging assay by acid urea PAGE northern blotting
- Immunopeptidome sample processing and LC-MS/MS
- Immunopeptidome data analysis
- *De novo* peptide sequencing
- Peptide-PRISM
- Differential enrichment analysis
- Peptide distribution along the source protein
- Construction of *ProxyPhe-peptides database*
- Data analysis workflow for ProxyPhe-peptide identification
- Integration and filtering
- Source validation
- Retention time and hydrophobicity index
- Allelic enrichment analysis
- Spectra validation
- Mass spectrometry analysis of proteolytic peptides (MAPP)
- Purification and concentration of proteasome peptides
- Mass spectrometry sample processing
- Liquid chromatography mass spectrometry
- Mass spectrometry data analysis
- Proteomics processing and label-free quantification
- Differential enrichment analysis and aberrant peptides identification
- Immunogenicity assessment for identified peptides (human)
- Identification of T cells reactive to aberrant peptides using multi-timers
- *In vivo* tumor inoculation
- *In vivo* CD8<sup>+</sup> T cell depletion
- Tumor cell lysate preparation
- T cell proliferation assay
- Dendritic cells immunopeptidomics
- Immunization of mice
- *Ex-vivo* peptide stimulation
- T cell:tumor cell co-culture
- scRNA-seq sample preparation
- scRNA-seq library preparation and next generation sequencing
- scRNA-seq library pre-processing, quality-control, MULTI-seq sample classification, and cell type annotation
- CODEX multiplexed tissue imaging
- *In vivo*  $\alpha$ -PD-1 therapy
- Patient DATA analysis
- **QUANTIFICATION AND STATISTICAL ANALYSIS**
  - Intercellular signaling predictions
  - scRNA-seq statistical tests
  - Codex image processing
  - Statistical analyses

## SUPPLEMENTAL INFORMATION

Supplemental information can be found online at <https://doi.org/10.1016/j.ccell.2025.03.003>.

Received: June 19, 2024

Revised: November 14, 2024

Accepted: March 3, 2025

Published: March 27, 2025

## REFERENCES

1. Tran, E., Robbins, P.F., and Rosenberg, S.A. (2017). 'Final common pathway' of human cancer immunotherapy: targeting random somatic mutations. *Nat. Immunol.* **18**, 255–262.
2. Gubin, M.M., Zhang, X., Schuster, H., Caron, E., Ward, J.P., Noguchi, T., Ivanova, Y., Hundal, J., Arthur, C.D., Krebber, W.J., et al. (2014). Checkpoint blockade cancer immunotherapy targets tumour-specific mutant antigens. *Nature* **515**, 577–581.
3. Deniger, D.C., Pasetto, A., Robbins, P.F., Gartner, J.J., Prickett, T.D., Paria, B.C., Malekzadeh, P., Jia, L., Yossef, R., Langhan, M.M., et al. (2018). T-cell Responses to TP53 "Hotspot" Mutations and Unique Neoantigens Expressed by Human Ovarian Cancers. *Clin. Cancer Res.* **24**, 5562–5573.
4. Blass, E., and Ott, P.A. (2021). Advances in the development of personalized neoantigen-based therapeutic cancer vaccines. *Nat. Rev. Clin. Oncol.* **18**, 215–229.
5. Fritsch, E.F., Burkhardt, U.E., Hacoheh, N., and Wu, C.J. (2020). Personal Neoantigen Cancer Vaccines: A Road Not Fully Paved. *Cancer Immunol. Res.* **8**, 1465–1469.
6. Vormehr, M., Türeci, Ö., and Sahin, U. (2019). Harnessing Tumor Mutations for Truly Individualized Cancer Vaccines. *Annu. Rev. Med.* **70**, 395–407.
7. Oliveira, G., Stromhaug, K., Klaeger, S., Kula, T., Frederick, D.T., Le, P.M., Forman, J., Huang, T., Li, S., Zhang, W., et al. (2021). Phenotype, specificity and avidity of antitumour CD8(+) T cells in melanoma. *Nature* **596**, 119–125.
8. Klebanoff, C.A., Acquavella, N., Yu, Z., and Restifo, N.P. (2011). Therapeutic cancer vaccines: are we there yet? *Immunol. Rev.* **239**, 27–44.
9. Sellars, M.C., Wu, C.J., and Fritsch, E.F. (2022). Cancer vaccines: Building a bridge over troubled waters. *Cell* **185**, 2770–2788.
10. Holly, J., and Yewdell, J.W. (2023). Game of Omes: ribosome profiling expands the MHC-I immunopeptidome. *Curr. Opin. Immunol.* **83**, 102342.
11. Prensner, J.R., Abelin, J.G., Kok, L.W., Clauser, K.R., Mudge, J.M., Ruiz-Orera, J., Bassani-Sternberg, M., Moritz, R.L., Deutsch, E.W., and van Heesch, S. (2023). What Can Ribo-Seq, Immunopeptidomics, and Proteomics Tell Us About the Noncanonical Proteome? *Mol. Cell. Proteomics* **22**, 100631.
12. Ouspenskaia, T., Law, T., Clauser, K.R., Klaeger, S., Sarkizova, S., Aguet, F., Li, B., Christian, E., Knisbacher, B.A., Le, P.M., et al. (2022). Unannotated proteins expand the MHC-I-restricted immunopeptidome in cancer. *Nat. Biotechnol.* **40**, 209–217.
13. Chong, C., Müller, M., Pak, H., Harnett, D., Huber, F., Grun, D., Leleu, M., Auger, A., Arnaud, M., Stevenson, B.J., et al. (2020). Integrated proteogenomic deep sequencing and analytics accurately identify non-canonical peptides in tumor immunopeptidomes. *Nat. Commun.* **11**, 1293.
14. Laumont, C.M., and Perreault, C. (2018). Exploiting non-canonical translation to identify new targets for T cell-based cancer immunotherapy. *Cell. Mol. Life Sci.* **75**, 607–621.
15. Laumont, C.M., Daouda, T., Laverdure, J.P., Bonneil, É., Caron-Lizotte, O., Hardy, M.P., Granados, D.P., Durette, C., Lemieux, S., Thibault, P., and Perreault, C. (2016). Global proteogenomic analysis of human MHC class I-associated peptides derived from non-canonical reading frames. *Nat. Commun.* **7**, 10238.
16. Ruiz Cuevas, M.V., Hardy, M.P., Holly, J., Bonneil, É., Durette, C., Courcelles, M., Lanoix, J., Côté, C., Staudt, L.M., Lemieux, S., et al. (2021). Most non-canonical proteins uniquely populate the proteome or immunopeptidome. *Cell Rep.* **34**, 108815.
17. Bartok, O., Pataskar, A., Nagel, R., Laos, M., Goldfarb, E., Hayoun, D., Levy, R., Körner, P.R., Kreuger, I.Z.M., Champagne, J., et al. (2021). Anti-tumour immunity induces aberrant peptide presentation in melanoma. *Nature* **590**, 332–337.
18. Laumont, C.M., Vincent, K., Hesnard, L., Audemard, É., Bonneil, É., Laverdure, J.P., Gendron, P., Courcelles, M., Hardy, M.P., Côté, C., et al. (2018). Noncoding regions are the main source of targetable tumor-specific antigens. *Sci. Transl. Med.* **10**, eaau5516.
19. Erhard, F., Dölken, L., Schilling, B., and Schlosser, A. (2020). Identification of the Cryptic HLA-I Immunopeptidome. *Cancer Immunol. Res.* **8**, 1018–1026.
20. Marcu, A., Schlosser, A., Keupp, A., Trautwein, N., Johann, P., Wölfel, M., Lager, J., Monoranu, C.M., Walz, J.S., Henkel, L.M., et al. (2021). Natural and cryptic peptides dominate the immunopeptidome of atypical teratoid rhabdoid tumors. *J. Immunother. Cancer* **9**, e003404.

21. Erhard, F., Halenius, A., Zimmermann, C., L'Hernault, A., Kowalewski, D.J., Weekes, M.P., Stevanovic, S., Zimmer, R., and Dölken, L. (2018). Improved Ribo-seq enables identification of cryptic translation events. *Nat. Methods* **15**, 363–366.
22. Barczak, W., Carr, S.M., Liu, G., Munro, S., Nicastrì, A., Lee, L.N., Hutchings, C., Ternette, N., Klenerman, P., Kanapin, A., et al. (2023). Long non-coding RNA-derived peptides are immunogenic and drive a potent anti-tumour response. *Nat. Commun.* **14**, 1078.
23. Malka, Y., Alkan, F., Ju, S., Körner, P.R., Pataskar, A., Shulman, E., Loayza-Puch, F., Champagne, J., Wenzel, C., Faller, W.J., et al. (2022). Alternative cleavage and polyadenylation generates downstream uncapped RNA isoforms with translation potential. *Mol. Cell* **82**, 3840–3855.e8.
24. Yewdell, J.W. (2022). MHC Class I Immunopeptidome: Past, Present, and Future. *Mol. Cell. Proteomics* **21**, 100230.
25. Bigot, J., Lalanne, A.I., Lucibello, F., Gueguen, P., Houy, A., Dayot, S., Ganier, O., Gilet, J., Tosello, J., Nemati, F., et al. (2021). Splicing Patterns in SF3B1-Mutated Uveal Melanoma Generate Shared Immunogenic Tumor-Specific Neopeptides. *Cancer Discov.* **11**, 1938–1951.
26. Zaher, H.S., and Green, R. (2009). Fidelity at the molecular level: lessons from protein synthesis. *Cell* **136**, 746–762.
27. Rodnina, M.V. (2023). Decoding and Recoding of mRNA Sequences by the Ribosome. *Annu. Rev. Biophys.* **52**, 161–182.
28. Mohler, K., and Ibba, M. (2017). Translational fidelity and mistranslation in the cellular response to stress. *Nat. Microbiol.* **2**, 17117.
29. Dedon, P.C., and Begley, T.J. (2022). Dysfunctional tRNA reprogramming and codon-biased translation in cancer. *Trends Mol. Med.* **28**, 964–978.
30. Endres, L., Fasullo, M., and Rose, R. (2019). tRNA modification and cancer: potential for the therapeutic prevention and intervention. *Future Med. Chem.* **11**, 885–900.
31. Truitt, M.L., and Ruggero, D. (2016). New frontiers in translational control of the cancer genome. *Nat. Rev. Cancer* **16**, 288–304.
32. Vaklavas, C., Blume, S.W., and Grizzle, W.E. (2017). Translational Dysregulation in Cancer: Molecular Insights and Potential Clinical Applications in Biomarker Development. *Front. Oncol.* **7**, 158.
33. Santos, M., Fidalgo, A., Varanda, A.S., Oliveira, C., and Santos, M.A.S. (2019). tRNA Deregulation and Its Consequences in Cancer. *Trends Mol. Med.* **25**, 853–865.
34. Park, S.G., Schimmel, P., and Kim, S. (2008). Aminoacyl tRNA synthetases and their connections to disease. *Proc. Natl. Acad. Sci. USA* **105**, 11043–11049.
35. Robichaud, N., Sonenberg, N., Ruggero, D., and Schneider, R.J. (2019). Translational Control in Cancer. *Cold Spring Harbor Perspect. Biol.* **11**, a032896.
36. Suzuki, T. (2021). The expanding world of tRNA modifications and their disease relevance. *Nat. Rev. Mol. Cell Biol.* **22**, 375–392.
37. Urbonavicius, J., Qian, Q., Durand, J.M., Hagervall, T.G., and Björk, G.R. (2001). Improvement of reading frame maintenance is a common function for several tRNA modifications. *EMBO J.* **20**, 4863–4873.
38. Pereira, M., Francisco, S., Varanda, A.S., Santos, M., Santos, M.A.S., and Soares, A.R. (2018). Impact of tRNA Modifications and tRNA-Modifying Enzymes on Proteostasis and Human Disease. *Int. J. Mol. Sci.* **19**, 3738.
39. Ou, X., Cao, J., Cheng, A., Peppelenbosch, M.P., and Pan, Q. (2019). Errors in translational decoding: tRNA wobbling or misincorporation? *PLoS Genet.* **15**, e1008017.
40. Huang, S.Q., Sun, B., Xiong, Z.P., Shu, Y., Zhou, H.H., Zhang, W., Xiong, J., and Li, Q. (2018). The dysregulation of tRNAs and tRNA derivatives in cancer. *J. Exp. Clin. Cancer Res.* **37**, 101.
41. Santos, M., Pereira, P.M., Varanda, A.S., Carvalho, J., Azevedo, M., Mateus, D.D., Mendes, N., Oliveira, P., Trindade, F., Pinto, M.T., et al. (2018). Codon misreading tRNAs promote tumor growth in mice. *RNA Biol.* **15**, 773–786.
42. Torres, A.G., Battle, E., and Ribas de Pouplana, L. (2014). Role of tRNA modifications in human diseases. *Trends Mol. Med.* **20**, 306–314.
43. Chujo, T., and Tomizawa, K. (2021). Human transfer RNA modopathies: diseases caused by aberrations in transfer RNA modifications. *FEBS J.* **288**, 7096–7122.
44. Orellana, E.A., Siegal, E., and Gregory, R.I. (2022). tRNA dysregulation and disease. *Nat. Rev. Genet.* **23**, 651–664.
45. Pinzaru, A.M., and Tavazoie, S.F. (2023). Transfer RNAs as dynamic and critical regulators of cancer progression. *Nat. Rev. Cancer* **23**, 746–761.
46. Noma, A., Kirino, Y., Ikeuchi, Y., and Suzuki, T. (2006). Biosynthesis of wybutosine, a hyper-modified nucleoside in eukaryotic phenylalanine tRNA. *EMBO J.* **25**, 2142–2154.
47. Noma, A., and Suzuki, T. (2006). Ribonucleome analysis identified enzyme genes responsible for wybutosine synthesis. *Nucleic Acids Symp. Ser.* **50**, 65–66.
48. El Yacoubi, B., Bailly, M., and de Crécy-Lagard, V. (2012). Biosynthesis and function of posttranscriptional modifications of transfer RNAs. *Annu. Rev. Genet.* **46**, 69–95.
49. Rodriguez, V., Chen, Y., Elkahlon, A., Dutra, A., Pak, E., and Chandrasekharappa, S. (2007). Chromosome 8 BAC array comparative genomic hybridization and expression analysis identify amplification and overexpression of TRMT12 in breast cancer. *Genes Chromosomes Cancer* **46**, 694–707.
50. Wang, K., Zheng, M., and Ren, Y. (2019). Overexpression of TRMT12 may independently predict poor overall survival in patients with head and neck squamous cell carcinoma. *Oncotargets Ther.* **12**, 7269–7279.
51. Rossello-Tortella, M., Llinas-Arias, P., Sakaguchi, Y., Miyauchi, K., Davalos, V., Setien, F., Calleja-Cervantes, M.E., Pineyro, D., Martinez-Gomez, J., Guil, S., et al. (2020). Epigenetic loss of the transfer RNA-modifying enzyme TYW2 induces ribosome frameshifts in colon cancer. *Proc. Natl. Acad. Sci. USA* **117**, 20785–20793.
52. Mikl, M., Pilpel, Y., and Segal, E. (2020). High-throughput interrogation of programmed ribosomal frameshifting in human cells. *Nat. Commun.* **11**, 3061.
53. Rak, R., Polonsky, M., Eizenberg-Magar, I., Mo, Y., Sakaguchi, Y., Mizrahi, O., Nachshon, A., Reich-Zeliger, S., Stern-Ginossar, N., Dahan, O., et al. (2021). Dynamic changes in tRNA modifications and abundance during T cell activation. *Proc. Natl. Acad. Sci. USA* **118**, e2106556118.
54. Rodriguez, V., Vasudevan, S., Noma, A., Carlson, B.A., Green, J.E., Suzuki, T., and Chandrasekharappa, S.C. (2012). Structure-function analysis of human TYW2 enzyme required for the biosynthesis of a highly modified Wybutosine (yW) base in phenylalanine-tRNA. *PLoS One* **7**, e39297.
55. Ingolia, N.T., Brar, G.A., Rouskin, S., McGeachy, A.M., and Weissman, J.S. (2013). Genome-wide annotation and quantitation of translation by ribosome profiling. *Curr. Protoc. Mol. Biol.* **4**, 4.18.1–4.18.19.
56. Konevega, A.L., Soboleva, N.G., Makhno, V.I., Semenov, Y.P., Wintermeyer, W., Rodnina, M.V., and Katunin, V.I. (2004). Purine bases at position 37 of tRNA stabilize codon-anticodon interaction in the ribosomal A site by stacking and Mg<sup>2+</sup>-dependent interactions. *RNA* **10**, 90–101.
57. Waas, W.F., Druzina, Z., Hanan, M., and Schimmel, P. (2007). Role of a tRNA base modification and its precursors in frameshifting in eukaryotes. *J. Biol. Chem.* **282**, 26026–26034.
58. Tukenmez, H., Xu, H., Esberg, A., and Bystrom, A.S. (2015). The role of wobble uridine modifications in +1 translational frameshifting in eukaryotes. *Nucleic Acids Res.* **43**, 9489–9499.
59. Caliskan, N., Wohlgemuth, I., Korniy, N., Pearson, M., Peske, F., and Rodnina, M.V. (2017). Conditional Switch between Frameshifting Regimes upon Translation of dnaX mRNA. *Mol. Cell* **66**, 558–567.e4.
60. Katunin, V., Soboleva, N., Makhno, V., Sedelnikova, E., Zhenodarova, S., and Kirillov, S. (1994). Effect of the nucleotide-37 on the interaction of tRNA(Phe) with the P site of Escherichia coli ribosomes. *Biochimie* **76**, 51–57.

61. Carlson, B.A., Mushinski, J.F., Henderson, D.W., Kwon, S.Y., Crain, P.F., Lee, B.J., and Hatfield, D.L. (2001). 1-Methylguanosine in place of Y base at position 37 in phenylalanine tRNA is responsible for its shiftiness in retroviral ribosomal frameshifting. *Virology* 279, 130–135.
62. Yewdell, J.W. (2011). DRiPs solidify: progress in understanding endogenous MHC class I antigen processing. *Trends Immunol.* 32, 548–558.
63. Kalaora, S., and Samuels, Y. (2019). Cancer Exome-Based Identification of Tumor Neo-Antigens Using Mass Spectrometry. *Methods Mol. Biol.* 1884, 203–214.
64. Cox, J., and Mann, M. (2008). MaxQuant enables high peptide identification rates, individualized p.p.b.-range mass accuracies and proteome-wide protein quantification. *Nat. Biotechnol.* 26, 1367–1372.
65. Marcu, A., Bichmann, L., Kuchenbecker, L., Kowalewski, D.J., Freudenmann, L.K., Backert, L., Mühlenbruch, L., Szolek, A., Lübke, M., Wagner, P., et al. (2021). HLA Ligand Atlas: a benign reference of HLA-presented peptides to improve T-cell-based cancer immunotherapy. *J. Immunother. Cancer* 9, e002071.
66. Lozano-Rabella, M., Garcia-Garijo, A., Palomero, J., Yuste-Estevanez, A., Erhard, F., Farriol-Duran, R., Martín-Liberal, J., Ochoa-de-Olza, M., Matos, I., Gartner, J.J., et al. (2023). Exploring the Immunogenicity of Noncanonical HLA-I Tumor Ligands Identified through Proteogenomics. *Clin. Cancer Res.* 29, 2250–2265.
67. Gessulat, S., Schmidt, T., Zolg, D.P., Samaras, P., Schnatbaum, K., Zerweck, J., Knaute, T., Rechenberger, J., Delanghe, B., Huhmer, A., et al. (2019). Prosit: proteome-wide prediction of peptide tandem mass spectra by deep learning. *Nat. Methods* 16, 509–518.
68. Wolf-Levy, H., Javitt, A., Eisenberg-Lerner, A., Kacem, A., Ulman, A., Sheban, D., Dassa, B., Fishbain-Yoskovitz, V., Carmona-Rivera, C., Kramer, M.P., et al. (2018). Revealing the cellular degradome by mass spectrometry analysis of proteasome-cleaved peptides. *Nat. Biotechnol.* 36, 1110–1116.
69. Javitt, A., Shmueli, M.D., Kramer, M.P., Kolodziejczyk, A.A., Cohen, I.J., Radomir, L., Sheban, D., Kamer, I., Litchfield, K., Bab-Dinitz, E., et al. (2023). The proteasome regulator PSME4 modulates proteasome activity and antigen diversity to abrogate antitumor immunity in NSCLC. *Nat. Can. (Ott.)* 4, 629–647.
70. Kong, A.T., Leprevost, F.V., Avtonomov, D.M., Mellacheruvu, D., and Nesvizhskii, A.I. (2017). MSFragger: ultrafast and comprehensive peptide identification in mass spectrometry-based proteomics. *Nat. Methods* 14, 513–520.
71. Ferreira, H.J., Stevenson, B.J., Pak, H., Yu, F., Almeida Oliveira, J., Huber, F., Taillandier-Coindard, M., Michaux, J., Ricart-Altimiras, E., Kraemer, A.I., et al. (2024). Immunopeptidomics-based identification of naturally presented non-canonical circRNA-derived peptides. *Nat. Commun.* 15, 2357.
72. McGranahan, N., and Swanton, C. (2019). Neoantigen quality, not quantity. *Sci. Transl. Med.* 11, eaax7918.
73. Ali, M., Foldvari, Z., Giannakopoulou, E., Bösch, M.L., Ströner, E., Yang, W., Toebe, M., Schubert, B., Kohlbacher, O., Schumacher, T.N., and Olweus, J. (2019). Induction of neoantigen-reactive T cells from healthy donors. *Nat. Protoc.* 14, 1926–1943.
74. Ali, M., Giannakopoulou, E., Li, Y., Lehander, M., Viriding Culleton, S., Yang, W., Knetter, C., Odabasi, M.C., Bollineni, R.C., Yang, X., et al. (2022). T cells targeted to TdT kill leukemic lymphoblasts while sparing normal lymphocytes. *Nat. Biotechnol.* 40, 488–498.
75. Giannakopoulou, E., Lehander, M., Viriding Culleton, S., Yang, W., Li, Y., Karpanen, T., Yoshizato, T., Rustad, E.H., Nielsen, M.M., Bollineni, R.C., et al. (2023). A T cell receptor targeting a recurrent driver mutation in FLT3 mediates elimination of primary human acute myeloid leukemia in vivo. *Nat. Can. (Ott.)* 4, 1474–1490.
76. Lo, W., Parkhurst, M., Robbins, P.F., Tran, E., Lu, Y.C., Jia, L., Gartner, J.J., Pasetto, A., Deniger, D., Malekzadeh, P., et al. (2019). Immunologic Recognition of a Shared p53 Mutated Neoantigen in a Patient with Metastatic Colorectal Cancer. *Cancer Immunol. Res.* 7, 534–543.
77. Holmstrom, M.O., Hjortso, M.D., Ahmad, S.M., Met, O., Martinenaite, E., Riley, C., Straten, P., Svane, I.M., Hasselbalch, H.C., and Andersen, M.H. (2017). The JAK2V617F mutation is a target for specific T cells in the JAK2V617F-positive myeloproliferative neoplasms. *Leukemia* 31, 495–498.
78. Patel, S.J., Sanjana, N.E., Kishton, R.J., Eidizadeh, A., Vodnala, S.K., Cam, M., Gartner, J.J., Jia, L., Steinberg, S.M., Yamamoto, T.N., et al. (2017). Identification of essential genes for cancer immunotherapy. *Nature* 548, 537–542.
79. Wolf, Y., Bartok, O., Patkar, S., Eli, G.B., Cohen, S., Litchfield, K., Levy, R., Jiménez-Sánchez, A., Trabish, S., Lee, J.S., et al. (2019). UVB-Induced Tumor Heterogeneity Diminishes Immune Response in Melanoma. *Cell* 179, 219–235.e21.
80. McGinnis, C.S., Patterson, D.M., Winkler, J., Conrad, D.N., Hein, M.Y., Srivastava, V., Hu, J.L., Murrow, L.M., Weissman, J.S., Werb, Z., et al. (2019). MULTI-seq: sample multiplexing for single-cell RNA sequencing using lipid-tagged indices. *Nat. Methods* 16, 619–626.
81. Koues, O.I., Collins, P.L., Cella, M., Robinette, M.L., Porter, S.I., Pyfrom, S.C., Payton, J.E., Colonna, M., and Oltz, E.M. (2016). Distinct Gene Regulatory Pathways for Human Innate versus Adaptive Lymphoid Cells. *Cell* 165, 1134–1146.
82. McGinnis, C.S., Miao, Z., Superville, D., Yao, W., Goga, A., Reticker-Flynn, N.E., Winkler, J., and Satpathy, A.T. (2024). The temporal progression of lung immune remodeling during breast cancer metastasis. *Cancer Cell* 42, 1018–1031.e6.
83. Andreatta, M., Corria-Osorio, J., Müller, S., Cubas, R., Coukos, G., and Carmona, S.J. (2021). Interpretation of T cell states from single-cell transcriptomics data using reference atlases. *Nat. Commun.* 12, 2965.
84. Daniel, B., Yost, K.E., Hsiung, S., Sandor, K., Xia, Y., Qi, Y., Hiam-Galvez, K.J., Black, M., J Raposo, C., Shi, Q., et al. (2022). Divergent clonal differentiation trajectories of T cell exhaustion. *Nat. Immunol.* 23, 1614–1627.
85. Black, S., Phillips, D., Hickey, J.W., Kennedy-Darling, J., Venkataramanan, V.G., Samusik, N., Goltsev, Y., Schürch, C.M., and Nolan, G.P. (2021). CODEX multiplexed tissue imaging with DNA-conjugated antibodies. *Nat. Protoc.* 16, 3802–3835.
86. Jin, S., Guerrero-Juarez, C.F., Zhang, L., Chang, I., Ramos, R., Kuan, C.H., Myung, P., Plikus, M.V., and Nie, Q. (2021). Inference and analysis of cell-cell communication using CellChat. *Nat. Commun.* 12, 1088.
87. Riaz, N., Havel, J.J., Makarov, V., Desrichard, A., Urba, W.J., Sims, J.S., Hodi, F.S., Martín-Algarra, S., Mandal, R., Sharfman, W.H., et al. (2017). Tumor and Microenvironment Evolution during Immunotherapy with Nivolumab. *Cell* 171, 934–949.e16.
88. Cabrita, R., Lauss, M., Sanna, A., Donia, M., Skaarup Larsen, M., Mitra, S., Johansson, I., Phung, B., Harbst, K., Vallon-Christersson, J., et al. (2020). Tertiary lymphoid structures improve immunotherapy and survival in melanoma. *Nature* 577, 561–565.
89. Auslander, N., Zhang, G., Lee, J.S., Frederick, D.T., Miao, B., Moll, T., Tian, T., Wei, Z., Madan, S., Sullivan, R.J., et al. (2018). Robust prediction of response to immune checkpoint blockade therapy in metastatic melanoma. *Nat. Med.* 24, 1545–1549.
90. Karpanen, T., and Olweus, J. (2017). The Potential of Donor T-Cell Repertoires in Neoantigen-Targeted Cancer Immunotherapy. *Front. Immunol.* 8, 1718.
91. Leko, V., and Rosenberg, S.A. (2020). Identifying and Targeting Human Tumor Antigens for T Cell-Based Immunotherapy of Solid Tumors. *Cancer Cell* 38, 454–472.
92. Anton, L.C., and Yewdell, J.W. (2014). Translating DRiPs: MHC class I immunosurveillance of pathogens and tumors. *J. Leukoc. Biol.* 95, 551–562.
93. Minati, R., Perreault, C., and Thibault, P. (2020). A Roadmap Toward the Definition of Actionable Tumor-Specific Antigens. *Front. Immunol.* 11, 583287.
94. Wei, J., Kishton, R.J., Angel, M., Conn, C.S., Dalla-Venezia, N., Marcel, V., Vincent, A., Catez, F., Ferré, S., Ayadi, L., et al. (2019). Ribosomal Proteins

- Regulate MHC Class I Peptide Generation for Immunosurveillance. *Mol. Cell* 73, 1162–1173.e5.
95. Yewdell, J.W., Dersh, D., and Fåhræus, R. (2019). Peptide Channeling: The Key to MHC Class I Immunosurveillance? *Trends Cell Biol.* 29, 929–939.
96. Perez-Riverol, Y., Bai, J., Bandla, C., García-Seisdedos, D., Hewapathirana, S., Kamatchinathan, S., Kundu, D.J., Prakash, A., Frericks-Zipper, A., Eisenacher, M., et al. (2022). The PRIDE database resources in 2022: a hub for mass spectrometry-based proteomics evidences. *Nucleic Acids Res.* 50, D543–D552.
97. Ritchie, M.E., Phipson, B., Wu, D., Hu, Y., Law, C.W., Shi, W., and Smyth, G.K. (2015). limma powers differential expression analyses for RNA-sequencing and microarray studies. *Nucleic Acids Res.* 43, e47.
98. Hao, Y., Stuart, T., Kowalski, M.H., Choudhary, S., Hoffman, P., Hartman, A., Srivastava, A., Molla, G., Madad, S., Fernandez-Granda, C., and Satija, R. (2024). Dictionary learning for integrative, multimodal and scalable single-cell analysis. *Nat. Biotechnol.* 42, 293–304.
99. Zhu, Q., Conrad, D.N., and Gartner, Z.J. (2023). deMULTiplex2: robust sample demultiplexing for scRNA-seq. Preprint at bioRxiv. <https://doi.org/10.1101/2023.04.11.536275>.
100. Phipson, B., Sim, C.B., Porrello, E.R., Hewitt, A.W., Powell, J., and Oshlack, A. (2022). propeller: testing for differences in cell type proportions in single cell data. *Bioinformatics* 38, 4720–4726.
101. Gu, Z., Eils, R., and Schlesner, M. (2016). Complex heatmaps reveal patterns and correlations in multidimensional genomic data. *Bioinformatics* 32, 2847–2849.
102. Amezquita, R.A., Lun, A.T.L., Becht, E., Carey, V.J., Carpp, L.N., Geistlinger, L., Marini, F., Rue-Albrecht, K., Risso, D., Soneson, C., et al. (2020). Orchestrating single-cell analysis with Bioconductor. *Nat. Methods* 17, 137–145.
103. Bankhead, P., Loughrey, M.B., Fernández, J.A., Dombrowski, Y., McArt, D.G., Dunne, P.D., McQuaid, S., Gray, R.T., Murray, L.J., Coleman, H.G., et al. (2017). QuPath: Open source software for digital pathology image analysis. *Sci. Rep.* 7, 16878.
104. Kuleshov, M.V., Jones, M.R., Rouillard, A.D., Fernandez, N.F., Duan, Q., Wang, Z., Koplev, S., Jenkins, S.L., Jagodnik, K.M., Lachmann, A., et al. (2016). Enrichr: a comprehensive gene set enrichment analysis web server 2016 update. *Nucleic Acids Res.* 44, W90–W97.
105. Sakai, Y., Miyauchi, K., Kimura, S., and Suzuki, T. (2016). Biogenesis and growth phase-dependent alteration of 5-methoxycarbonylmethoxyuridine in tRNA anticodons. *Nucleic Acids Res.* 44, 509–523.
106. Liao, Y., Smyth, G.K., and Shi, W. (2014). featureCounts: an efficient general purpose program for assigning sequence reads to genomic features. *Bioinformatics* 30, 923–930.
107. Love, M.I., Huber, W., and Anders, S. (2014). Moderated estimation of fold change and dispersion for RNA-seq data with DESeq2. *Genome Biol.* 15, 550.
108. Ingolia, N.T., Brar, G.A., Rouskin, S., McGeachy, A.M., and Weissman, J.S. (2012). The ribosome profiling strategy for monitoring translation in vivo by deep sequencing of ribosome-protected mRNA fragments. *Nat. Protoc.* 7, 1534–1550.
109. Nagao, A., Suzuki, T., Katoh, T., Sakaguchi, Y., and Suzuki, T. (2009). Biogenesis of glutaminyl-mt tRNAGln in human mitochondria. *Proc. Natl. Acad. Sci. USA* 106, 16209–16214.
110. Varshney, U., Lee, C.P., and RajBhandary, U.L. (1991). Direct analysis of aminoacylation levels of tRNAs in vivo. Application to studying recognition of Escherichia coli initiator tRNA mutants by glutaminyl-tRNA synthetase. *J. Biol. Chem.* 266, 24712–24718.
111. Martin, F.J., Amode, M.R., Aneja, A., Austine-Orimoloye, O., Azov, A.G., Barnes, I., Becker, A., Bennett, R., Berry, A., Bhai, J., et al. (2023). Ensembl 2023. *Nucleic Acids Res.* 51, D933–D941.
112. Reynisson, B., Alvarez, B., Paul, S., Peters, B., and Nielsen, M. (2020). NetMHCpan-4.1 and NetMHCIIpan-4.0: improved predictions of MHC antigen presentation by concurrent motif deconvolution and integration of MS MHC eluted ligand data. *Nucleic Acids Res.* 48, W449–W454.
113. Zhang, J., Xin, L., Shan, B., Chen, W., Xie, M., Yuen, D., Zhang, W., Zhang, Z., Lajoie, G.A., and Ma, B. (2012). PEAKS DB: de novo sequencing assisted database search for sensitive and accurate peptide identification. *Mol. Cell. Proteomics* 11, M111.010587.
114. Tran, N.H., Qiao, R., Xin, L., Chen, X., Liu, C., Zhang, X., Shan, B., Ghodsi, A., and Li, M. (2019). Deep learning enables de novo peptide sequencing from data-independent-acquisition mass spectrometry. *Nat. Methods* 16, 63–66.
115. Zhang, X., Smits, A.H., van Tilburg, G.B., Ovaa, H., Huber, W., and Vermeulen, M. (2018). Proteome-wide identification of ubiquitin interactions using UbiA-MS. *Nat. Protoc.* 13, 530–550.
116. Zhang, X., Smits, A.H., van Tilburg, G.B.A., Jansen, P.W.T.C., Makowski, M.M., Ovaa, H., and Vermeulen, M. (2017). An Interaction Landscape of Ubiquitin Signaling. *Mol. Cell* 65, 941–955.e8.
117. Li, W., Jaroszewski, L., and Godzik, A. (2001). Clustering of highly homologous sequences to reduce the size of large protein databases. *Bioinformatics* 17, 282–283.
118. Li, W., Jaroszewski, L., and Godzik, A. (2002). Tolerating some redundancy significantly speeds up clustering of large protein databases. *Bioinformatics* 18, 77–82.
119. Li, W., and Godzik, A. (2006). Cd-hit: a fast program for clustering and comparing large sets of protein or nucleotide sequences. *Bioinformatics* 22, 1658–1659.
120. Van der Auwera, G.A., Carneiro, M.O., Hartl, C., Poplin, R., Del Angel, G., Levy-Moonshine, A., Jordan, T., Shakir, K., Roazen, D., Thibault, J., et al. (2013). From FastQ data to high confidence variant calls: the Genome Analysis Toolkit best practices pipeline. *Curr. Protoc. Bioinformatics* 43, 11.10.1–11.10.33.
121. Li, H.D., Funk, C.C., and Price, N.D. (2020). iREAD: a tool for intron retention detection from RNA-seq data. *BMC Genom.* 21, 128.
122. Krokhin, O.V., Craig, R., Spicer, V., Ens, W., Standing, K.G., Beavis, R.C., and Wilkins, J.A. (2004). An improved model for prediction of retention times of tryptic peptides in ion pair reversed-phase HPLC: its application to protein peptide mapping by off-line HPLC-MALDI MS. *Mol. Cell. Proteomics* 3, 908–919.
123. Zeng, W.F., Zhou, X.X., Willems, S., Ammar, C., Wahle, M., Bludau, I., Voytik, E., Strauss, M.T., and Mann, M. (2022). AlphaPeptDeep: a modular deep learning framework to predict peptide properties for proteomics. *Nat. Commun.* 13, 7238.
124. Virtanen, P., Gommers, R., Oliphant, T.E., Haberland, M., Reddy, T., Cournapeau, D., Burovski, E., Peterson, P., Weckesser, W., Bright, J., et al. (2020). SciPy 1.0: fundamental algorithms for scientific computing in Python. *Nat. Methods* 17, 261–272.
125. Pataskar, A., Champagne, J., Nagel, R., Kanski, J., Laos, M., Michaux, J., Pak, H.S., Bleijerveld, O.B., Mordente, K., Navarro, J.M., et al. (2022). Tryptophan depletion results in tryptophan-to-phenylalanine substituents. *Nature* 603, 721–727.
126. Toebes, M., Coccors, M., Bins, A., Rodenko, B., Gomez, R., Nieuwkoop, N.J., van de Kastelee, W., Rimmelzwaan, G.F., Haanen, J.B.A.G., Ovaa, H., and Schumacher, T.N.M. (2006). Design and use of conditional MHC class I ligands. *Nat. Med.* 12, 246–251.
127. Hadrup, S.R., Bakker, A.H., Shu, C.J., Andersen, R.S., van Veluw, J., Hombrink, P., Castermans, E., Thor Straten, P., Blank, C., Haanen, J.B., et al. (2009). Parallel detection of antigen-specific T-cell responses by multidimensional encoding of MHC multimers. *Nat. Methods* 6, 520–526.
128. Li, K., Vaudel, M., Zhang, B., Ren, Y., and Wen, B. (2019). PDV: an integrative proteomics data viewer. *Bioinformatics* 35, 1249–1251.
129. Crinier, A., Milpied, P., Escaliere, B., Piperoglou, C., Galluso, J., Balsamo, A., Spinelli, L., Cervera-Marzal, I., Ebbo, M., Girard-Madoux, M., et al.

- (2018). High-Dimensional Single-Cell Analysis Identifies Organ-Specific Signatures and Conserved NK Cell Subsets in Humans and Mice. *Immunity* 49, 971–986.e5.
130. Snyder, A., Makarov, V., Merghoub, T., Yuan, J., Zaretsky, J.M., Desrichard, A., Walsh, L.A., Postow, M.A., Wong, P., Ho, T.S., et al. (2014). Genetic basis for clinical response to CTLA-4 blockade in melanoma. *N. Engl. J. Med.* 371, 2189–2199.
131. Rooney, M.S., Shukla, S.A., Wu, C.J., Getz, G., and Hacohen, N. (2015). Molecular and Genetic Properties of Tumors Associated with Local Immune Cytolytic Activity. *Cell* 160, 48–61.
132. Wherry, E.J., Ha, S.J., Kaech, S.M., Haining, W.N., Sarkar, S., Kalia, V., Subramaniam, S., Blattman, J.N., Barber, D.L., and Ahmed, R. (2007). Molecular signature of CD8+ T cell exhaustion during chronic viral infection. *Immunity* 27, 670–684.
133. Schmidt, U., Weigert, M., Broaddus, C., and Myers, G. (2018). Cell Detection with Star-Convex Polygons (Cham: Springer International Publishing), pp. 265–273.
134. von Chamier, L., Laine, R.F., Jukkala, J., Spahn, C., Krentzel, D., Nehme, E., Lerche, M., Hernández-Pérez, S., Mattila, P.K., Karinou, E., et al. (2021). Democratising deep learning for microscopy with ZeroCostDL4Mic. *Nat. Commun.* 12, 2276.
135. DeLong, E.R., DeLong, D.M., and Clarke-Pearson, D.L. (1988). Comparing the areas under two or more correlated receiver operating characteristic curves: a nonparametric approach. *Biometrics* 44, 837–845.
136. Therneau, T.M., and Grambsch, P.M. (2000). *Modeling Survival Data: Extending the Cox Model* (Springer-Verlag).
137. Therneau, T., and Lumley, T. (2015). *Package Survival: A Package for Survival Analysis in R*. R Package. Version 238. <https://doi.org/10.32614/CRAN.package.survival>.

**STAR★METHODS**

**KEY RESOURCES TABLE**

REAGENT or RESOURCE	SOURCE	IDENTIFIER
<b>Antibodies</b>		
anti-TYW2 (TRMT12)	Novus-Biologicals	Cat#NBP1-76583; RRID: AB_11025190
anti- $\alpha$ tubulin mouse	Millipore	Cat#05-829; RRID: AB_310035
anti-mCherry	Abcam	Cat#Ab167453; RRID: AB_2571870
anti-rabbit HRP conjugate	Cell Signaling Technology	Cat#5127; RRID: AB_10892860
anti-mouse HRP conjugate	Cell Signaling Technology	Cat#91196; RRID: AB_2940774
pan-HLA antibody W6/32	ATCC	ATCC-HB-95RRID; N/A
APC anti human HLA A,B,C	BioLegend	Cat# 311410; RRID: AB_314879
PE anti-human CD3	BioLegend	Cat#300308; RRID: AB_314044
FITC anti-human CD8	BioLegend	Cat#301060; RRID: AB_2564165
APC anti-human CD137 (41BB)	BioLegend	Cat#309810; RRID: AB_830672
APC anti- human IFN $\gamma$	BioLegend	Cat#502512; RRID: AB_315237
APC anti-human TNF $\alpha$	BioLegend	Cat#502912; RRID: AB_315264
APC anti-human CD8	BioLegend	Cat#300912; RRID: AB_314116
PE-Cy7 anti-human CD3	BioLegend	Cat# 300316; RRID: AB_314052
PE anti- human IFN $\gamma$	BioLegend	Cat#502509; RRID: AB_315234
BV421 anti-human TNF $\alpha$	BioLegend	Cat# 502932; RRID: AB_10960738
InVivoMAb anti-mouse CD8 $\alpha$ , clone 2.43	BioXcell	Cat#BE0061; RRID: AB_1125541
InVivoMAb rat IgG2b isotype control, clone LTF-2	BioXcell	Cat#BE0090; RRID: AB_1107780
InVivoMAb anti-mouse PD-1 (CD279), clone RMP1-14	BioXcell	Cat#BE0146; RRID: AB_10949053
InVivoMAb rat IgG2a isotype control, clone 2A3	BioXcell	Cat#BE0089; RRID: AB_1107769
CD8 $\alpha$ (D4W2Z) XP $\text{\textcircled{R}}$ Rabbit mAb	Cell Signaling Technology	Cat#60168RRID; N/A
Anti-CD3 epsilon antibody [CAL57]	abcam	Ab251607RRID; N/A
Anti-LAG-3 antibody [CAL77]	abcam	Ab251606RRID; N/A
CD45 (D3F8Q) Rabbit mAb	Cell Signaling Technology	Cat#98819RRID; N/A
BD Pharmingen $\text{\textsuperscript{TM}}$ Purified Mouse Anti-Ki-67	BD Biosciences	Cat#556003; RRID: AB_396287
FITC anti-mouse CD3	BioLegend	Cat#100203; RRID: AB_312660

(Continued on next page)

**Continued**

REAGENT or RESOURCE	SOURCE	IDENTIFIER
PE anti-mouse CD4	BioLegend	Cat#100511; RRID: AB_312714
APC anti-mouse CD8	BioLegend	Cat#100711; RRID: AB_312750
APC anti-mouse CD3	Biolegend	Cat#100236; RRID: AB_2561456
PacificBlue anti-mouse CD8	Biolegend	Cat#100725; RRID: AB_493425
VioletFluor450 anti-mouse CD45 antibody	Tonbo Biosciences	Cat#75-0451-U100; RRID: AB_2621947
PE-Cy7 anti-mouse CD44 antibody	BioLegend	Cat#103030; RRID: AB_830787
FITC anti-mouse TCR $\beta$ antibody	BioLegend	Cat#109206; RRID: AB_313429
BV421 anti-mouse TCR $\beta$ antibody	BioLegend	Cat#109229; RRID: AB_10933263
Anti-Mouse H-2Db	SouthrenBiotech	Cat#1910-01; RRID: AB_2795489
InVivoMAb anti-mouse MHC Class I (H-2Kb), clone Y-3	BioXCell	Cat#BE0172; RRID: AB_10949300
BV421 anti-mouse CD3	Biolegend	Cat#100228; RRID: AB_2562553
APC-Cy7 anti-mouse CD44	Biolegend	Cat#103028; RRID: AB_830785
BV605 anti-mouse CD8	Biolegend	Cat#100744; RRID: AB_2562609
TruStain FcX™ (anti-mouse CD16/32) antibody	Biolegend	Cat#101319; RRID: AB_1574973
FITC anti-mouse CD3	Biolegend	Cat#100203; RRID: AB_312660
Alexa Fluor 700 anti-mouse CD8a antibody	Biolegend	Cat#100729; RRID: AB_493702
PE anti-mouse TNF $\alpha$ antibody	Biolegend	Cat#506305; RRID: AB_315426
Anti-PSMA-1	Produced from Hybridoma	kind gift from Keiji Tanaka
Anti-Mouse CD16 / CD32 (Fc Sheild)	Tonbo Biosciences	Cat#70-0161-U500; RRID: AB_2621487

**Biological samples**

PBMCs from healthy donors	Weizmann Institute of Science	IRB#2274-2
PBMCs from healthy donors	Oslo University Hospital	REK#2018/879

**Chemicals, peptides, and recombinant proteins**

Ficoll-Paque PLUS	Cytiva	Cat#17144003
Dextrane	Sigma Aldrich	Cat#31392
Trisodium citrate dihydrate	Sigma Aldrich	Cat#S1804
Lipofectamine 2000™	Invitrogen	Cat#11668019
NP-40 Alternative	Calbiochem	Cat#492016
protease-inhibitor cocktail III	Calbiochem	Cat#539134
Protease Inhibitors Cocktail	Sigma Aldrich	Cat#P8340
Synthetic peptides	GenScript Biotech Corp.	N/A
RPMI 1640 medium	Gibco	Cat# 21875-034
Fetal Bovine Serum (FBS)	Gibco	Cat#12657-029

(Continued on next page)

**Continued**

REAGENT or RESOURCE	SOURCE	IDENTIFIER
L-glutamine	Biological Industries	Cat#03-020-1B
Penicillin	Invitrogen	Cat#15140163
HEPES	Sigma Aldrich	Cat#H0887
SDS Solution 20%	Bio-Rad	Cat# 161-0418
Water, ultra-pure	Biological Industries	Cat#01-866-1A
b-mercaptoethanol	EMD Millipore Corp.	Cat#444203
Dulbecco's Phosphate Buffered Saline (PBS)	Biological Industries	Cat#02-023-1A
Sodium pyruvate	Biological Industries	Cat#03-042-1B
TBE/UREA 2X loading dye	Thermo Fisher Scientific	Cat#LC6876
Syber Gold 10000X	Invitrogen	Cat#S11494
40% Acryl (29:1)	Sigma Aldrich	Cat# A7802
T4 PNK	NEB	Cat#M0201L
T4 RNA Ligase 2 truncated K227Q	NEB	Cat#M0351S
T4 PNK	Toyobo	Code#PNK-111
Lipopolysaccharides (LPS) from E-coli O111:B4	Sigma Aldrich	Cat#L26630
Opti-MEM Reduced Serum Medium	Gibco	Cat#31985-047
Trypsin for cell culture	Corning	REF#25-051-CI
5' Deanenylase	NEB	Cat#M0331S
RecJf	NEB	Cat#M0264S
10mM dNTPs	Invitrogen	Cat#18427
Superscript III	Invitrogen	Cat#18080044
0.1M DTT	NEB	Cat#B1222A
GlycoBlue™ Coprecipitant	Invitrogen	Cat#AM9515
Single strand RNA ladder	NEB	Cat#M0364S
Paraformaldehyde (PFA) 16%	Thermo Scientific	Cat#28908
sodium deoxycholate	Sigma Aldrich	Cat#D6750
Iodoacetamide	Sigma Aldrich	Cat#I6125
EDTA	Promega	Cat#V4231
PMSF	Sigma Aldrich	Cat#78830
octyl-b-D glucopyranoside	Sigma Aldrich	Cat#O8001
Dynabeads Protein-G	Thermo Fisher Scientific	Cat#10003D
KAPA HiFi HotStart ReadyMix	Roche	Cat# KK2602
Not1	NEB	Cat#R0189S
EcoRI	NEB	Cat#R0101S
CutSmart	NEB	Cat#B6004
FspI	NEB	Cat#R0135S
TurboFect	Thermo Fisher Scientific	Cat#R0531
RNase A	Thermo Fisher Scientific	Cat#EN0531
DNase I	STEMCELL technologies	Cat#100-0762
DSP	Thermo Fisher Scientific	Cat#22585
Protein G PLUS-Agarose	Santa Cruz	Cat#sc-2002
L-cysteine	Sigma Aldrich	Cat#C7352
LIVE/DEAD Fixable blue dead cell stain	Thermo Fisher Scientific	Cat# L23105
MACS buffer	Miltenyi Biotec	Cat#130-091-221
TRI Reagent	Sigma Aldrich	Cat#T9424
Puromycin	Sigma-Aldrich	Cat#P8833
Trifluoroacetic acid (TFA)	Sigma-Aldrich	Cat#302031
Acetonitrile (ACN)	Bio lab	Cat#000120410100
DMSO	MP Biomedicals	Cat#196055
Human GM-CSF	PeprTech	Cat#300-03

(Continued on next page)

**Continued**

REAGENT or RESOURCE	SOURCE	IDENTIFIER
Human IL-4	PeproTech	Cat#200-04
Human IL-15	PeproTech	Cat#200-15
Human IL-7	PeproTech	Cat#200-07
Human IL-21	PeproTech	Cat#200-21
Human IFN $\gamma$	PeproTech	Cat#300-02
Human AB Serum	Bio IVT	HUMANABSRMP-HI-1
Murine GM-CSF	PeproTech	Cat#315-03-50
Murine IL-4	PeproTech	Cat#214-14-50
Monensin	BioLegend	Cat#420701
Brefeldin A	BioLegend	Cat#420601
Intracellular staining permeabilization wash buffer	BioLegend	Cat#421002
Heparin	Sigma Aldrich	Cat#H3393
ACK Lysing Buffer	Gibco	REF#A10492-01
CELLBANKER 2	Amsbio	SKU#11914
Targeted Retrieval Solution, pH 9	Agilent	Cat#S236784-2
Protein A Resin	Genscript	Cat#L00210
Protein G Resin	Genscript	Cat#L00209
Hanks' Balanced Salt solution (HBSS)	Sigma-Aldrich	Cat#H6648
Histopaque-1077 Hybri-Max	Sigma-Aldrich	Cat#H8889
Anti-CD8 biotin	Biologend	Cat#100704
streptavidin nanobeads	Biologend	Cat#480016
Insulin-Transferrin-Selenium	Thermo Fisher Scientific	Cat#41400045
CellTrace™ CFSE	Thermo Fisher Scientific	Cat# C34554
DAPI	Thermo Fisher Scientific	Cat# D1306
Propidium Iodide (PI) Solution	Biologend	Cat#421301
Adjuvant Incomplete Freund	BD Biosciences	Cat#263910
M.TUBERCULOSIS H37 Ra	BD Biosciences	Cat#231141

**Critical commercial assays**

EZ-PCR mycoplasma	Biological Industries	SKU:20-700-20
DNeasy Blood & Tissue	Qiagen	Cat#69504
Wizard Genomic DNA purification	Promega	REF A9281
NGSgo® - Multiplexed HLA amplification 6 loci	GenDx	MX6-1
Dynabeads mRNA DIRECT Purification Kit	Invitrogen	Cat#61011
CORALL Total RNA-seq library prep kit	LEXOGEN	N/A
Human CD14 MicroBeads	Miltenyi Biotec	Cat#130-050-201
EasySep Human T cell enrichment kit	STEMCELL technologies	Cat#19051
Mouse Tumor Dissociation Kit	Miltenyi Biotec	Cat#130-096-730
Anti-CD11c microbeads	Miltenyi Biotec	Cat#130-125-835
CD8a (Ly-2) MicroBeads, mouse	Miltenyi Biotec	Cat#130-117-044
MojoSort™ Mouse CD8 Nanobeads	Biologend	Cat#480136
ELISA , Mouse IFN-gamma DuoSet	R&D systems	Cat#DY485
MULTI-seq Lipid-Modified Oligos	Millipore-Sigma	LMO001-100RXN
Agilent High Sensitivity DNA Kit	Agilent	5067-4626
Qubit dsDNA HS Assay kit	Fisher Scientific	Q32854
NovaSeq X Series 10B Reagent Kit (100 cycles)	Illumina	20085596
Zombie NIR viability dye	BioLegend	Cat#423105
Pierce™ BCA Protein Assay Kit	Thermo Fisher Scientific	Cat#A65453

**Deposited data**

Melanoma Cell Lines Mass Spectrometry data (Immunopeptidomics, MAPP and Proteomics)	This study	PRIDE: PXD053256
---	------------	------------------

(Continued on next page)

**Continued**

REAGENT or RESOURCE	SOURCE	IDENTIFIER
Bulk RNAseq	This study	BioProject: IDPRJNA1045112
Ribosome Profiling	This study	BioProject: IDPRJNA1045083
HLA-Ligand ATLAS Mass Spectrometry data	Marcu et al. <sup>65</sup>	N/A
DCs Mass Spectrometry data	This study	PRIDE: PXD053256
Raw scRNA-seq data	This study	GEO: GSE272996
Riaz et al. cohort	Riaz et al. <sup>87</sup>	GEO: GSE91061
Cabrita cohort	Cabrita et al. <sup>88</sup>	GEO: GSE65904
Auslander cohort	Auslander et al. <sup>89</sup>	GEO: GSE115821
TCGA primary melanoma cohort	TCGA data portal SKCM	<a href="https://portal.gdc.cancer.gov/projects/TCGA-SKCM">https://portal.gdc.cancer.gov/projects/TCGA-SKCM</a>
TCGA Gene expression counts data	GDC Xena Hub	<a href="https://xenabrowser.net/datapages/?dataset=TCGASKCM.htseq_counts.tsv&amp;host=https%3A%2F%2Fgdc.xenahubs.net&amp;removeHub=https%3A%2F%2Fxena.treehouse.gi.ucsc.edu%3A443">https://xenabrowser.net/datapages/?dataset=TCGASKCM.htseq_counts.tsv&amp;host=https%3A%2F%2Fgdc.xenahubs.net&amp;removeHub=https%3A%2F%2Fxena.treehouse.gi.ucsc.edu%3A443</a>

**Experimental models: Cell lines**

A-375	ATCC	CRL-1619™
SK-MEL-5	ATCC	HTB-70™
SK-Mel-30	DSMZ	ACC-151
Murine melanoma B2905	Laboratory of Prof. Merlino	N/A
HEK293T	ATCC	CRL-3216™
721.221 monoallelic B cells	IHWG cell land DNA bank	N/A

**Experimental models: Organisms/strains**

C57BL/6J OlaHst	Envigo	N/A
NOD.Cg-Prkdc scidll2rg tm1Wjl/SzJ (NSG)	The Jackson Laboratory	Strain#JAX:005557; RRID:IMSR_JAX:005557
C57BL/6J-Rag2em3Lutzj/J (Rag2 KO)	The Jackson Laboratory	Strain #:033526; RRID:IMSR_JAX:033526

**Recombinant DNA**

pSpCas9 (BB)-2A-GFP (PX458)	Addgene	RRID:Addgene_48138
Human <i>Tyw2</i> #1 sgRNA: (5' - GGATGGCTCGGT GGCGCTAC CGG - 3')	Rosella et al., <sup>51</sup> , Sigma-Aldrich	N/A
Human <i>Tyw2</i> #2 sgRNA: (5' AGGCTGATTTGCC CCGATCA TGG - 3')	Rosella et al. <sup>51</sup> , Sigma-Aldrich	N/A
Human <i>Tyw2</i> KO validation primer Forward (5'- TGTGGTTGTTAGCAACATGGA - 3')	Rosella et al. <sup>51</sup> , Sigma-Aldrich	N/A
Human <i>Tyw2</i> KO validation primer Reverse (5' - CTCTACCCAGCCATGGTCAC - 3')	Rosella et al. <sup>51</sup> , Sigma-Aldrich	N/A
Murine <i>Tyw2</i> #1 sgRNA: (5' - TAGCGGAGCGAG TTTAG CTC - 3')	This study, Sigma- Aldrich	N/A
Murine <i>Tyw2</i> #2 sgRNA: (5' CTCGAAGTTTCTCG GTG ATG - 3')	This study, Sigma- Aldrich	N/A
Murine <i>Tyw2</i> KO validation primer Forward (5'-CCCACTGCACCCGAAATTCC - 3')	This study, Sigma- Aldrich	N/A
Murine <i>Tyw2</i> KO validation primer Reverse (5' - TTCAGTTTCTGTTGTCCCC - 3')	This study, Sigma- Aldrich	N/A
Human <i>TYW2</i> K225Q primer Forward (5'-CATC ACTGAGCAGCTTCGAGTGGC- 3')	This study, Sigma- Aldrich	N/A
Human <i>TYW2</i> K225Q primer Reverse (5'- GCC ACTCGAAGCTGCTCAGTGATG- 3')	This study, Sigma- Aldrich	N/A
DNA probe tRNA <sup>phe</sup> - 5'-TGGTGCCGAAACC CGGGATCGAACCAGGGACCTTTAGATC-3'	This study	N/A
pCDH-CMV Human <i>TYW2</i>	This study	N/A
pCDH-CMV-MCS-EF1 $\alpha$ -Neo	SBI	Cat#CD514B-1RRID: N/A

(Continued on next page)

**Continued**

REAGENT or RESOURCE	SOURCE	IDENTIFIER
pMD2.G	Addgene	RRID: Addgene_12259
psPAX2	Addgene	RRID: Addgene_12260
pLV-EIF1a-IRES-Puro Murine <i>tyw2</i>	This study	N/A
MULTI-seq anchor LMO: TGGAATTCTCGG GTGCCAAGGGTAACGATCCAGCTGCTCACT- [Lignoceric-Acid]	This study	N/A
MULTI-seq co-anchor LMO: [Palmitic-Acid]- AGTGACAGCTGGATCGTTAC	This study	N/A
MULTI-seq barcodes: CCTTGGCACCCGAGA ATTCCA- [8bp-Index]-AAAAAAAAAAAAAAAA AAAAAAAAAAAAAAAA	This study	N/A
TruSeq RPI I7 indices: CAAGCAGAAGACGGC ATACGAGAT-[6bp-Index]-GTGACTGGAGTTC CTTGGCACCCGAGAATTCCA	This study	N/A
Universal I5 index: AATGATACGGCGACCAC CGAGATCTACACTCTTCCCTACACGACGC TCTTCCGATCT	This study	N/A
<b>Software and algorithms</b>		
NGSengine® HLA typing software V2.13	GenDx	<a href="https://www.gendx.com/product_line/ngsengine/">https://www.gendx.com/product_line/ngsengine/</a>
Kaluza software v.2.2	Beckman Colter	<a href="https://www.beckman.co.il/flow-cytometry/software/kaluza/downloads">https://www.beckman.co.il/flow-cytometry/software/kaluza/downloads</a>
FLOWJO software V10.10.0	BD Biosciences	<a href="https://www.flowjo.com/solutions/flowjo/downloads">https://www.flowjo.com/solutions/flowjo/downloads</a>
R studio v. 2023.12.0+369	N/A	<a href="https://cran.rstudio.com">https://cran.rstudio.com</a>
PyCharm v.2024.1.1 Community edition	JetBrains	<a href="https://www.jetbrains.com/pycharm/">https://www.jetbrains.com/pycharm/</a>
Jupyter_core 4.9.1	N/A	<a href="https://github.com/jupyter/jupyter_core">https://github.com/jupyter/jupyter_core</a>
MaxQuant v.proteogenomic, 2.1.3.0	This study	N/A
NetMHCpan 4.1	DTU Health Tech	<a href="https://services.healthtech.dtu.dk/services/NetMHCpan-4.1/">https://services.healthtech.dtu.dk/services/NetMHCpan-4.1/</a>
PEAKS X Pro	Bioinformatics Solutions Inc.	<a href="https://www.bioinfor.com/peaks-xpro/">https://www.bioinfor.com/peaks-xpro/</a>
Peptide-PRISM	Erhard et al. <sup>19</sup>	<a href="https://erhard-lab.de/software">https://erhard-lab.de/software</a>
FragPipe v.21.1	Nesvilab	<a href="https://github.com/Nesvilab/FragPipe/releases">https://github.com/Nesvilab/FragPipe/releases</a>
BioRender	BioRender	<a href="http://biorender.com/">http://biorender.com/</a>
Code for Integrated <i>de novo</i> and search engine pipeline (Figure 2B)	This study	<a href="https://github.com/YSamuelsLab/MetaPept2">https://github.com/YSamuelsLab/MetaPept2</a>
Code for scRNA-seq analysis	This study	<a href="https://synapse.org/Synapse:syn61841510">synapse.org/Synapse:syn61841510</a>
scRNA-seq companion code	This study	Zenodo <a href="https://doi.org/10.5281/zenodo.12802673">https://doi.org/10.5281/zenodo.12802673</a>
Cell Ranger version 6.0.0	10x Genomics	<a href="https://10xgenomics.com/support">10xgenomics.com/support</a>
R package – Seurat v.5.0.1	Hao et al. <sup>98</sup>	<a href="https://satijalab.org/seurat/">satijalab.org/seurat/</a>
R package – deMULTIplex2 v. 1.0.1	Zhu et al. <sup>99</sup>	<a href="https://github.com/Gartner-Lab/deMULTIplex2">github.com/Gartner-Lab/deMULTIplex2</a>
R package – CellChat v. 1.6.1	Jin et al. <sup>86</sup>	<a href="https://github.com/sqjin/CellChat">github.com/sqjin/CellChat</a>
R package – Speckle v.0.99.7	Phipson et al. <sup>100</sup>	<a href="https://bioconductor.org/packages/release/bioc/html/speckle.html">bioconductor.org/packages/release/bioc/html/speckle.html</a>
R package – ComplexHeatmap v. 2.14.0	Gu et al. <sup>101</sup>	<a href="https://bioconductor.org/packages/release/bioc/html/ComplexHeatmap.html">bioconductor.org/packages/release/bioc/html/ComplexHeatmap.html</a>
R package – SingleCellExperiment version 1.20.1	Amezquita et al. <sup>102</sup>	<a href="https://bioconductor.org/packages/release/bioc/html/SingleCellExperiment.html">bioconductor.org/packages/release/bioc/html/SingleCellExperiment.html</a>
QuPath - v0.4.3	Bankhead et al. <sup>103</sup>	<a href="https://qupath.github.io/">https://qupath.github.io/</a>
R package – Survminer v.0.4.9	-	<a href="https://github.com/kassambara/survminer/">https://github.com/kassambara/survminer/</a>
R package – SurvRM2 v.1.0-4	-	<a href="https://github.com/cran/survRM2">https://github.com/cran/survRM2</a>
R package – enrichR v.3.2	Kuleshov et al. <sup>104</sup>	<a href="https://www.rdocumentation.org/packages/enrichR/versions/3.2">https://www.rdocumentation.org/packages/enrichR/versions/3.2</a>

(Continued on next page)

**Continued**

REAGENT or RESOURCE	SOURCE	IDENTIFIER
Other		
SPRIselect	Beckman Coulter	B23319
Bovine Serum Albumin	Sigma-Aldrich	A8577-50M
Sep-Pak tC18 96-well	Waters	Cat#186002321
Ultra-Micro SpinColumn, C18	Harvard Apparatus	BVD-74-7206
S-Trap microcolumns	Protifi, USA	C02-96well

**EXPERIMENTAL MODEL AND STUDY PARTICIPANT DETAILS**

**Cell culture**

Human melanoma cell lines A-375 (A375, CRL-1619<sup>TM</sup>; HLA-A\*01:01; HLA-A\*02:01; HLA-B\*44:03; HLA-B\*57:01; HLA-C\*06:02; HLA-C\*16:01) and SK-MEL-5 (SKMEL5, HTB-70<sup>TM</sup>; HLA-A\*11:01; HLA-A\*02:01; HLA-B\*07:02; HLA-B\*40:01; HLA-C\*03:04; HLA-C\*07:02) as well as 293T kidney epithelial cells were purchased from the American Type Culture Collection (ATCC). SK-Mel-30 (SKMEL-30; HLA-A\*01:01; HLA-A\*02:01; HLA-B\*08:01; HLA-B\*44:02; HLA-C\*07:01; HLA-C\*05:01) human melanoma cell line (ACC-151) was purchased from DSMZ (<https://www.dsmz.de>). 721.221 B cells (IHWO0001) were purchased from the Fred Hutch International Histocompatibility Working Group (IHWG) cell and DNA Bank (<https://www.fredhutch.org/en.html>). Murine melanoma B2905 cells<sup>78</sup> were kindly provided from Prof. Glen Merlino's laboratory. All cell lines were tested regularly and were found negative for mycoplasma contamination (using EZ-PCR mycoplasma kit; Biological Industries). All cell lines were cultured at 37°C in Roswell Park Memorial Institute 1640 Medium (RPMI 1640, Gibco), supplemented with heat-inactivated 10% fetal bovine serum (Gibco), 25mM HEPES (Gibco), and 100U/ml penicillin-streptomycin (Gibco). All cell lines were maintained in a humidified atmosphere containing 5% CO<sub>2</sub> at 37°C. Peripheral blood mononuclear cells (PBMCs) were isolated from healthy donors.

**Mice**

Mice were maintained under specific pathogen-free (SPF) conditions at the Weizmann Institute's animal facility and were handled in accordance with the guidelines of the Institutional Animal Care and Use Committee (08571123-1). For *ex vivo* assays, mice were monitored in the TAU animal facility under the approval number of TAU - MD - IL2310 - 163 - 5 and TAU - MD - IL2401 - 102 - 5. Food and water were given *ad libitum*. Wild-type C57BL/6 (B6) mice were purchased from Harlan Laboratories. NOD.Cg-Prkdcscid1l2rgtm1Wjl/SzJ (NSG) and C57BL/6J-Rag2em3Lutzj/J (*Rag2* KO) were obtained from Jackson laboratory.

**Healthy donors for PBMC extraction**

The study was approved by the Weizmann Institutional Review Board and informed consent was obtained from healthy donors in accordance with the IRB doctrine of the Weizmann Institute of Science (protocol number 2274-2). The study was approved by the Regional Committee for Medical and Health Research Ethics (REK) South-East Norway, the Institutional Review Board, and the Data Protection Officer at Oslo University Hospital. Informed consent was obtained from healthy donors following the Declaration of Helsinki and institutional guidelines (REK 2018/879). PBMCs including donor 50 (D50; HLA-A\*01:01, HLA-A\*33:03, HLA-B\*38:02, HLA-B\*57:01, HLA-C\*06:02, HLA-C\*07:02) and donor 160 (D160; HLA-A\*01:01, HLA-A\*30:02, HLA-B\*18:01, HLA-B\*57:01, HLA-C\*06:02, HLA-C\*05:01) were isolated using Ficoll-Paque PLUS (Cytiva) according to the manufacturer's instructions.

**METHOD DETAILS**

**HLA-typing of healthy donor PBMCs**

DNA samples were typed for HLA-A, -B, -C, using the MX6-1 NGS typing kit (GenDx) according to the manufacturer's instructions. The library was paired-end sequenced (2x150bp) on an Iseq100 platform (Illumina). FASTQ files were analyzed in NGSengine® HLA typing software V2.13 (GenDx), using IPD-IMGT/HLA database 3.33.0. Final genotyping calls were made after manual review.

**CRISPR-Cas9 mediated KO for *TYW2***

Two sgRNAs for human *TYW2* (SG1; GGATGGCTCGGTGGCGCTAC CGG, SG2; AGGCTGATTGCCCCGATCA TGG) were kindly provided by Esteller's lab.<sup>51</sup> For the murine *Tyw2*, the following sgRNAs were used: SG1; TAGCGGAGCGAGTTTAG CTC, SG2; CTCGAAGTTTCTCGGTG ATG. Guides were cloned into pSpCas9 (BB)-2A-GFP vector (Addgene). sgRNAs were simultaneously transiently transfected into cells using Lipofectamine 2000 transfection reagent (Invitrogen). 48h later, single GFP<sup>+</sup> cells were sorted into 96-well plates using a BD FACSAria III (BD Biosciences) to form clonal cell lines. Since the transiently transfected constructs are not integrated into genome, Cas9, sgRNA and GFP are not expressed in any cell clones that were subjected to downstream experiments. To genotype the single cell-derived clones for *TYW2* status, DNA was extracted using DNeasy Blood & Tissue Kit (QIAGEN) and a PCR reaction for amplification of a 589 bp amplicon in the human genome (Fwd: 5'-TGTGGTTGTAGCAACATGGA-3'; Rev: 5'-CTCTACCCAGCCATGGTCAC-3') spanning the sgRNA targeting region was applied. For the murine gene, the following primers

were used for PCR: Fwd: 5'- CCCACTGCACCCGAAATTCC-3'; Rev: 5'- TTCAGTTTCTGTTGTCCCC-3'. PCR products were cleaned using Wizard Genomic DNA purification kit (Promega), and samples were analyzed using Sanger sequencing.

### Immunoprecipitation assay and western blot analysis

For TYW2 immunoprecipitation, cells were lysed in NP40 lysis buffer (50mM Tris-HCl [pH 7.4], 150mM NaCl, 1mM EDTA, 0.1% NP40) supplemented with protease inhibitor cocktail (Sigma-Aldrich). Cells were sonicated in a Bioruptor sonicator (Diagenode, 3 cycles of 10 sec) and then centrifuged at 17,000g for 10 minutes at 4°C. Clear lysates were rotated overnight at 4°C with an anti-TYW2 antibody (NBP1-76583, Novus-Biologicals). The next day, Dynabeads Protein G (Thermo Fisher Scientific) were added to the samples for 1 hour at 4°C. Beads were then washed five times with NP40 buffer. Proteins were released from beads by boiling and were resolved by SDS-PAGE.

For western blot analysis, cells were harvested and lysed directly in Laemmli sample buffer containing 2.5% beta-mercaptoethanol followed by sonication. The following antibodies were used: anti-TYW2 rabbit polyclonal antibody (NBP1-76583, Novus Biologicals), anti- $\alpha$  tubulin mouse mAb (DM1A, Millipore), anti-mCherry rabbit polyclonal antibody (ab167453, abcam), mouse anti-rabbit IgG, HRP conjugate (Cell Signaling), and goat anti-mouse IgG HRP conjugate (Cell Signaling).

### MS shotgun analysis of tRNA<sup>Phe</sup> from the cells

Total RNA from cellular models was extracted by TRI Reagent (Sigma-Aldrich) according to manufacturer's instructions. Class I tRNA fraction excision was performed from 10% Urea-PAGE gel, and 2-4 pmol of tRNAs were digested with RNase A (Thermo Fisher Scientific) and subjected to capillary-LC/nano ESI-MS analyzed by liquid chromatography-mass spectrometry as described previously.<sup>105</sup> The modification frequencies indicated in chromatograms were calculated from the peak area ratio of the multiply charged negative ions (-2 to -3) for RNA fragments with different modifications.

### Lentiviral production, mutagenesis, and viral transduction

The human or murine TYW2 WT insert was cloned into the pCDH-CMV lentiviral vector backbone plasmid (Addgene) by Not1 (NEB) and EcoRI (NEB) restriction enzymes, using CutSmart and FspI cloning reagents (NEB). For TYW2 point mutation induction (K225Q mutation), a mutagenesis procedure was used on the WT insert in a two-step PCR reaction. Following Sanger sequencing verification, the insert was cloned into the pCDH-CMV lentiviral vector backbone plasmid. Lentiviral vectors were transfected together with packaging constructs pMD2.G and psPAX2 (#12259 and #12260, Addgene) into 293T cells, using TurboFect transfection reagent (Thermo Fisher Scientific). 72 hours later, viruses were collected and used to infect TYW2 KO cells. Infected cells were selected with Puromycin (A375: 1 $\mu$ g/ml, SKMEL30, B2905: 2 $\mu$ g/ml). For the generation of 721.221 monoallelic B cells, HLA-B\*57:01 or HLA-A\*02:01 or HLA-A\*11:01 DNA was cloned into lentivector pCDH-CMV-MCS-EF1 $\alpha$ -Neo (SBI). Lentiviral particles were produced as described above. 721.221 B cells (HLA-I null) were infected and selected with neomycin (G-418, Sigma-Aldrich). For the *in vivo* experiments presented in [Figures 5D](#) and [S5F](#), pLV-EIF1a-IRES-Puro vector (EV or *Tyw2* WT) were generated and infected into *Tyw2* KO cells as described above.

### PRF reporter assay

Cells were transfected with either an in-frame control ('frame 0') or the -1 FS reporter construct ('frame -1', where mCherry is translated in frame, followed by a linker containing the slippery sequence UUUUUUA. GFP translation occurs only upon ribosomal slippage to the -1 frame)<sup>52</sup> using lipofectamine 2000 transfection reagent (Invitrogen). 24 hours later, cells were washed with PBS, harvested, and stained with LIVE/DEAD Fixable blue dead cell stain (Thermo Fisher Scientific). Cells were washed with MACS buffer (Miltenyi Biotec) and subjected to flow cytometry analysis using a CytoFLEX instrument (Beckman Coulter). Results were analyzed using the Kaluza software (Beckman Coulter). Gated, 'live cell' population was further analysed using R.

Specifically, from the mCherry<sup>+</sup> cell population (fluorescence intensity >10<sup>4</sup>), three different expression ranges were selected according to the Mean Fluorescence Intensity (MFI) of mCherry. Then, for each range, the GFP/mCherry ratio was calculated for each cell independently. GFP/mCherry ratios were presented by density plots. For 'frame 0' construct experiments, ratios were multiplied by 10. For 'frame -1' construct experiments, ratios were multiplied by 10<sup>3</sup>. Statistical analysis was performed separately for each construct and range. All reporter experiments were tested by the ANOVA test, followed by the Tukey HSD post-hoc test for significant ANOVA experiments. Notably, most ranges were normally distributed across all groups. However, because some repetitions violated the assumption of normality (significant Shapiro test) and/or the homoscedasticity (significant Leven's test) assumption, all experiments were also tested by the Kruskal-Wallis (KS) test, and significant KS experiments were subjected to Dunnett post-hoc analysis.

### Bulk RNA-sequencing

Cell lines used for bulk RNA-sequencing were grown in 10cm plates. Upon reaching 80% confluency, total RNA was extracted using TRI Reagent (Sigma-Aldrich), according to the manufacturer's recommendations. Libraries were constructed using COALL Total RNA-seq library prep kit (LEXOGEN), containing UDI 12nt Unique Dual Indexing. Samples were sequenced using NovaSeq (SP100). FASTQ files were processed with the CORALL RNA-Seq integrated data analysis pipelines (<https://www.lexogen.com/corall-data-analysis/>). After completing the quantification with FeatureCounts,<sup>106</sup> DESeq2<sup>107</sup> was used to perform differential gene expression analysis between TYW2 KO and WT samples (background genotype was 'WT', adjusted p-value threshold = 0.05), the data was filtered to select genes exhibiting positive or negative trends in at least two KO cell lines, and the PathCards

database ([pathcards.genecards.org/](http://pathcards.genecards.org/)) was used to identify molecular pathways (e.g. tRNA processing) represented amongst these differentially-expressed genes. To construct the merged volcano plots, we applied a function to keep a representative sample with the most negative or positive value.

### Ribosome profiling

The construction of ribosome-protected fragment (RPF) libraries was done as previously described,<sup>108</sup> with one modification: Fragments corresponding to size range of 17–34bp were purified from TBE-Urea gel. RPF libraries were sequenced using the NovaSeq (SP100), and raw FASTQ files were trimmed to remove the adaptor 'CTGTAGGCACCATCAATATCTCGTATGCCGCTTCTGCTTG AAAA' using the bbdut script in BBtools ([jgi.doe.gov/data-and-tools/bbtools/](http://jgi.doe.gov/data-and-tools/bbtools/)). rRNA sequences were also removed by alignment to a non-coding RNA library, after which trimmed reads failing to align were then aligned to the hg38 human genome sequence using STAR.

To quantify codon-specific effects, we defined the pause score for each instance of a codon of interest as the ratio of the ribosome density on the codon, normalized by the density on the transcript where it occurs. We computed pause scores for the 61 sense codons by averaging the pause scores across tens of thousands of instances of each codon across the transcriptome. The log<sub>2</sub> of the ratio of pause scores in the KO/WT was reported to highlight the differences in the samples.

To compute the metaplot, each open reading frame (ORF) with an average read density >1 (A375 n=4978, SKMEL30 n=4299) was split into 100 bins. For each of these ORFs, the number of reads per bin was determined and divided by the total number of reads for this ORF to obtain relative bin frequencies. The meta value for each bin was then computed as the average of the relative frequencies across all ORFs.

The N-terminal and C-terminal ribosome occupancies were computed for all ORFs with an average read density >1 (A375 n=4978, SKMEL30 n=4299) as the total number of reads mapped to the first or last 50 codon triplets, respectively. log<sub>2</sub> fold changes for each ORF were computed with a pseudocount of 0.1.

### tRNA charging assay by acid urea PAGE northern blotting

Total RNA was extracted from each cell line under acidic conditions and low temperature as described previously.<sup>109,110</sup> As for a deacylated tRNA, 60 μg of WT total RNA was incubated with deacylation buffer containing 20mM CHES-NaOH (pH 9.0) at 37°C for 2h followed by ethanol precipitation. Ten μg of total RNA was resolved by 7.5% PAGE containing 7M urea and 0.1M NaOAc (pH 5.2) at 4°C overnight, blotted onto a nylon membrane, dried, and cross-linked by UV (254nm, 1200mJ/cm<sup>2</sup>). The DNA probes for tRNA<sup>Phe</sup> (5'-TGGTGCCGAAACCCGGGATCGAACCAGGGACCTTTAGATC-3') were 5'-labeled with [ $\gamma$ -<sup>32</sup>P] ATP (PerkinElmer) using T4 Polynucleotide Kinase (Toyobo). The membrane was subjected to hybridization at 50°C overnight in hybridization buffer [500mM sodium phosphate buffer (pH 7.4), 7.5% SDS, 5% polyethylene glycol 6000, 1mM EDTA-NaOH (pH 8.0), and 0.5% Casein] and 4 pmol of the 5'-<sup>32</sup>P-radiolabeled DNA probe. The membrane was washed three times with 1 × SSC [150mM NaCl, 15mM Sodium citrate (pH 7.0)], dried, and exposed to an imaging plate (BAS-MS2040, Fujifilm) to visualize the hybridization bands using the FLA-7000 fluorimager (Fujifilm).

### Immunopeptidome sample processing and LC-MS/MS

HLA purification was done as previously described.<sup>63</sup> Briefly, cell pellets consisting of 2 × 10<sup>8</sup> cells were homogenized and lysed with lysis buffer (containing 0.25% sodium deoxycholate, 0.2mM iodoacetamide, 1mM EDTA, protease inhibitor cocktail (Sigma-Aldrich), 1mM PMSF and 1% octyl-β-D-glucopyranoside in PBS) and incubated at 4°C for 1 hour. Lysates were cleared by centrifugation at 4°C, 48,000g for 45 minutes and passed through a pre-clearing column containing Protein A resin beads (GenScript). Human-derived HLA-peptide complexes were then immunoaffinity purified from the cleared lysate using pan-HLA antibody (W6/32 antibody purified from HB95 hybridoma cells), covalently bound to Protein A Resin (Genescript). For the mouse-derived MHC complexes a 1:1 ratio of anti-Mouse H-2Db (UNLB, SouthernBiotech) and anti-mouse H-2Kb (Y-3, BioXCell) were covalently bound to Protein G Resin (Genescript; same beads were used at the pre-clear step). The MHC-peptide complexes were eluted with 1% trifluoroacetic acid (TFA), followed by purification of the peptides by Sep-Pak tC18 100mg Sorbent 96-well plate (Waters). Elution of the peptides was done with 28% acetonitrile (ACN) in 0.1% trifluoroacetic acid TFA.

In preparation for LC-MS/MS analysis, MHC peptides were dried by vacuum centrifugation and resolubilized with 0.1% formic acid. For Orbitrap MS/MS experiments, the peptides were separated using reversed-phase chromatography using the nanoAquity system (Waters), with a Symmetry trap column (180 × 20 mm) and HSS T3 analytical column, 0.75 × 250 mm (Waters), mobile phase A: H<sub>2</sub>O+0.1% formic acid, B: acetonitrile+0.1% formic acid. The peptides were separated with a linear gradient over 2h from 5 to 28% B, 28 to 35% in 15min, 35% to 95% in 15min, maintained at 95% for 10min and back to initial conditions, at a flow rate of 0.35 μl min<sup>-1</sup>.

The LC was connected online via a nano-electrospray ionization source (Flexlon, Thermo Scientific) using an emitter (Fossil) to either a Quadrupole Orbitrap MS (Q Exactive HF, Thermo Scientific) or a tribrid MS (Fusion Lumos, Thermo Scientific). Data were acquired using a data-dependent method, fragmenting the peptides by higher-energy collisional dissociation (HCD). On the Q Exactive HF, full-scan MS spectra were acquired at a resolution of 120,000 at 200 m/z with automated gain control (AGC) value of 3 × 10<sup>6</sup> ions, mass range of 300 to 1800 Th and maximum injection time of 100msec. MS/MS scans were acquired with an AGC target value of 10<sup>5</sup> with a maximum injection time of 150 msec, isolation of 1.7 Th, normalized collision energy was set to 30%, and MS/MS resolution was 15,000 at 200 m/z. Fragmented m/z values were dynamically excluded from further selection for 20s.

On the Fusion Lumos, full-scan MS spectra were acquired at a resolution of 120,000 at 200 m/z with AGC value of 200%, mass range of 300 to 1800 Th and maximum injection time set to auto. MS/MS scans were acquired with an AGC target value of 100% with a maximum injection time of 150 msec, isolation of 1.7 Th, normalized collision energy was set to 27%, and MS/MS resolution was 15,000 at 200 m/z. Fragmented m/z values were dynamically excluded from further selection for 20 s.

For timsTOF (TTP) experiments, the peptides were resolubilized with 0.1% trifluoroacetic acid and 5mM TCEP before LC-MS/MS analysis. 5 $\mu$ L of each sample was loaded using the nanoElute2 (Bruker, Germany) liquid chromatography. Mobile phase A was 0.1% formic acid in water. B was 0.1% formic acid in acetonitrile. Peptides were separated using the Aurora Ultimate C18 nano column, 0.075x250mm (IonOptiks, Australia), using a gradient of 2% B to 29% B in 80min, then 0.5min to 95% B, maintained 95%B for 2.9min at flow of 300nL/min. The column was placed in the column toaster and connected to a CaptiveSpray Electrospray ionization source. The column was maintained at 50°C. Data was acquired with a timsTOF Pro (Bruker) in data-dependent-acquisition-parallel-accumulation-serial-fragmentation (DDA-PASEF) mode with the following parameters: capillary voltage of 1600v, temperature of 180°C, mass range of 100-1,700 Th, ion mobility 0.6-1.57 1/K0, tims ramp time of 300msec, number of PASEF MS/MS scans 10, target intensity of 20,000 with threshold of 2,500, charge range 0 to 5, collision energy of 20 at 0.6 1/K0 and 59 at 1.6 1/K0.

### Immunopeptidome data analysis

RAW files were analyzed using a MaxQuant (MQ)<sup>64</sup> newly-developed 2-stage database search version (v.proteogenomic, 2.1.3.0) which evaluates target-decoy-based FDR separately for the canonical CDS proteins (searched with the human Ensemble<sup>111</sup> v.109) as well as peptides from other databases (see below). The following parameters were used for the search: LFK was set to a 'minimum ratio count' of 1. A peptide spectrum match FDR of 0.05 was used, and no protein FDR was set. The enzyme digestion was set as 'unspecific,' N-terminal acetylation and methionine oxidation were set as variable modifications, the 'match between runs' option was disabled to avoid false identifications across the samples, mass tolerance was set to 20ppm, and the decoy mode used was reverted. NetMHCpan v.4.1<sup>112</sup> was utilized to predict peptide binding affinity (binder <2% rank).

GO enrichment analysis was performed on genes that present canonical peptides identified in MQ, at least in two replicates for each sample. Enriched GO terms were identified using the R package "enrichR 3.2"<sup>104</sup> and "GO\_Biological\_Process\_2015" database for human genes. Pathways with adjusted P values below 0.05 were considered. Heatmaps were generated using the "seaborn 0.11.2" Python library. The heatmap color density represents the gene count (GC), which was calculated according to the formula:  $GC = \log_2(N+1)$ , where N – is the number of genes in the pathway. Knockout gene abundance (GA) was calculated for GO terms as follows:

$$GA = 100 * (K^{KO} - K^{WT}) / N, \text{ if } K^{KO} > K^{WT}$$

$$GA = 0, \text{ if } K^{KO} < K^{WT}$$

where

$K^{KO}$  – the number of genes shared only between knockout samples in the pathway,

$K^{WT}$  – the number of genes that originated from wild-type samples in the pathway,

N – the total number of annotated genes in the pathway

All GO terms for each cell line are presented in [Table S1](#).

### De novo peptide sequencing

De novo sequencing was performed with PEAKS X (Bioinformatics Solutions Inc.)<sup>113,114</sup> as described in.<sup>19</sup> Parent Mass Error Tolerance was set to 10 ppm, and Error Tolerance was set to 0.02 Da.

### Peptide-PRISM

Peptide-PRISM was applied as described in<sup>19,66</sup> with some modifications; initially, we generated and searched on-the-fly databases according to the following categories termed Prio1/Frameshift:

CDS>UTR5>OffFrame>UTR3>ncRNA>Frameshift>Intronic>Intergenic. FDR control was built on the mixture modeling described by Erhard et al.<sup>19</sup> Then, we filtered PSMs with best ALC>80 and Q<0.1, removed 'frameshift, intronic' incidence, and non-binders (NetMHCpan rank > 2%) and observed the different distribution of categories and off-frame identifications.

When Peptide-PRISM was utilized as a part of the orthogonal independent strategy, we included an 'Extra' database termed ProxyPhe (described in the following paragraph) and generated two new priorities:

Prio2:CDS>UTR5>OffFrame>UTR3>ncRNA>ProxyPhe>Intronic>Intergenic, and Prio3: CDS>ProxyPhe>UTR5>OffFrame>UTR3>ncRNA>Intronic>Intergenic. All three Prio were combined and subjected to the rational filtering step (described below). 'Other cryptic' denotes non-canonical peptides other than ProxyPhe:

UTR5, OffFrame, UTR3, ncRNA, Frameshift, Intronic, and Intergenic.

### Differential enrichment analysis

Mass spectrometry data was analyzed using DEP<sup>115</sup> with the following configurations: A375\_ii dataset was analyzed by MQ with SwissProt database (UniProtKB, 2024) and 'peptide.txt' was used as input for DEP pipeline.<sup>116</sup> Missing values were treated as Thr value was set to 0, and imputation was applied by the MinProb function with q = 0.01. Significant peptides were considered

as  $\alpha = 0.05$  computed by protein-wise linear models combined with empirical Bayes statistics implemented in limma R package,<sup>97</sup> and log<sub>2</sub> fold change of 1.5.

### Peptide distribution along the source protein

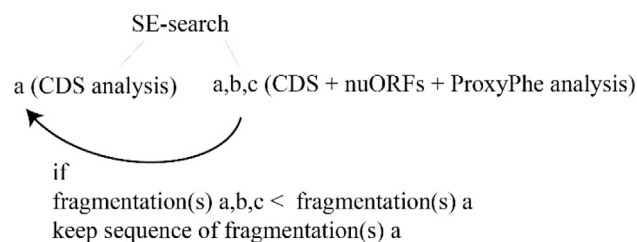
Source proteins were ranked by the number of mapped peptide sequences. The top 25 of them, which were represented by the highest number of peptides, were subjected for further analysis. The distribution of peptide spectra along protein lengths was analyzed on A375\_ii dataset prior to the integration pipeline (described above). To find spectrum locations, each canonical peptide sequence observed in at least two technical replicas of a cell line was mapped to the corresponding protein sequence, to determine its relative position on the protein in the range from 0 to 100% of the protein length. For ProxyPhe-peptides mapping (from the A375\_ii dataset; post-integration pipeline (see below)), an *in-silico* reversed translation was applied to identify the canonical peptide corresponding to the same protein location. Canonical and ProxyPhe-peptides were then mapped to the normalized source protein length as described above.

### Construction of ProxyPhe-peptides database

Coding sequences of GRCh38 were downloaded from Ensembl, and all transcript variants were included. The steps are presented in Figure S3A. Briefly, transcripts with fewer than 150 nt were discarded. Sequences not containing an in-frame TTT/TTC codon (corresponding to Phenylalanine (Phe)) were excluded. Only coding sequences starting with ATG were kept. In cases with multiple in-frame TTT/TTC codons per transcript, each TTT/TTC along the sequence was frameshifted separately. Aberrant peptide databases were constructed to identify trans-frame (- chimera of in-frame and out-of-frame) peptides and adjacent off-frame in a narrow window of 13 amino acids surrounding Phe residues (As a 13-amino-acid window upstream to the Phe in question consists of all possible HLA-I-bound altered peptides). The *in silico* off-frame translation was applied up to the first stop codon in the new frame. In the last step, in cases of 100% sequence identity, sequence redundancy was removed, and the most extended sequence was kept using CD-HIT.<sup>117–119</sup>

### Data analysis workflow for ProxyPhe-peptide identification

For the Search Engine (SE) arm, we utilized MQ proteogenomic search (with the parameters detailed above) and performed two independent runs: i) containing only canonical sequences (termed 'a', Ens v.109), and ii) 'a,b,c' – containing canonical, nuORFs<sup>12</sup> and ProxyPhe databases. The updated MQ version allows the user to separately treat the canonical and cryptic spaces (i.e. the nuORFs and ProxyPhe) with separated 0.05 FDR (prioritizing first the canonical space). As leucine and isoleucine residues are indistinguishable by MS due to their identical molecular masses, we looped through our list of all peptides in all the different categories, termed 'I2L followed by db-search' (Canonical, nuORFs, and ProxyPhe) in which inverting I to L (or L to I) resulted in peptides that can be derived from a canonical sequence. The I to L loop prioritization was: canonical>nuORFs>ProxyPhe. We then utilized NetMHCpan for HLA-I binding prediction and kept HLA-binders (HLA rank < 2%). To avoid misinterpretation, the last part of the SE arm was to perform 'scan validation versus run a', whereby fragment ion mass spectra identified in both canonical and ProxyPhe databases are tested to discard PSMs with a higher number of peptide fragment ions in run 'a' compared to run 'a,b, and c' querying only for 'b' and 'c' databases.



In parallel, we applied a modified Peptide-PRISM as described above. The PSMs of both methods were then integrated and filtered as described below.

### Integration and filtering

An integration algorithm was applied to the SE and Peptide-PRISM outputs to generate a 'combined' list of peptides. The integration algorithm input is derived from i) database searching (MQ output) and ii) *de-novo* peptide identification (Peptide-PRISM output). A peptide is included in the list of combined peptides if detected in MQ and Peptide-PRISM outputs in at least one replicate. Additionally, PSMs were kept as follows: Peptide-PRISM unique peptides with ALC>80 and Q<0.1, combined peptides with ALC>80\* and Q<0.1 (\* - we also obtained ALC>70 sequences if their fragmentation coverage was > 80 and their delta score >10). Fragmentation coverage was calculated as the number of fragmented ions (0 or 1) between two amino acids along the peptide sequence length -1 (multiplied by 100). All integrated PSMs are shown in Table S1.

### Source validation

To confirm that the identified ProxyPhe peptides were not derived from insertions/deletions (indels) or from intron-retention events and somatic variants, we analysed RNAseq data using the GATK<sup>120</sup> and iREAD<sup>121</sup> analysis tools, respectively, to filter out such

sequences. Identified events that matched PSM identifications after integration step are presented in [Table S1](#) and were excluded from further analysis.

To restrict the list of ProxyPhe hits to cancer-specific peptides, the PSMs identified in the melanoma cells (presented in [Table S1](#)) were intersected with peptides identified in the benign HLA-ligand ATLAS<sup>65</sup> ([Table S1](#)), that was re-analysed using the modified Peptide-PRISM pipeline. Matched hits are indicated in 'HLA\_atlas\_PRISM' column in [Table S1](#). Immunopeptidomic data of healthy donors' PBMCs that harbor the HLA-B\*57:01 allotype (generated in this study) was analyzed as described for the HLA-ligand ATLAS ([Table S1](#)).

ProxyPhe peptides that passed all filters (not intersected with GATK, iREAD, HLA ligand ATLAS and the healthy donors' PBMCs) are shown in [Table S1](#).

In addition to the filtration steps described above, we searched the peptide spectrum matches (PSM) identified by peptide-PRISM for identical peptide sequences that could be derived from an alternative, non-canonical translation of a different transcript/ UTR of the same transcript. These 'ambiguous peptides' are indicated in [Table S1](#).

### Retention time and hydrophobicity index

Hydrophobicity values for total PSM peptides were predicted with R package *protViz* version 0.7.7<sup>122</sup> (<https://CRAN.R-project.org/package=protViz>) and were plotted against the experimental retention time for the A375\_i dataset ([Figure 2D](#)). In addition, retention time values for eluted peptides were predicted using the AlphaPeptDeep framework for the A375\_i dataset ([Figure 2E](#)).<sup>123</sup> LS-MS/MS raw files and MQ ProxyPhe library output were used to fine-tune the AlphaPeptDeep's default model for each cell line. After model tuning, the MQ and Peptide-PRISM combined peptides were processed with AlphaPeptDeep in the 'precursor table' mode. A charge value for each peptide was taken from the 'best fragmentation coverage' scan. Observed RT values were normalized according to the formula:  $RT = (RT_{observed} - RT_{min}) / (RT_{max} - RT_{min})$ . Applied linear regressions were built with the statistics library from *scipy* Python package version 1.8.0.<sup>124</sup>

### Allelic enrichment analysis

The enrichment of ProxyPhe peptide presentation by different HLA alleles in KO and WT samples was calculated according to the formulas for strong and weak binders,

$$E_{ProxyPhe}^{KO} = 1000 * K_{ProxyPhe}^{KO} / N_{Canonical}^{KO}$$

$$E_{ProxyPhe}^{WT} = 1000 * K_{ProxyPhe}^{WT} / N_{Canonical}^{WT}$$

$$E_{ProxyPhe}^{KO,WT} = 2000 * K_{ProxyPhe}^{KO,WT} / (N_{Canonical}^{KO} + N_{Canonical}^{WT})$$

where

$E_{ProxyPhe}^{KO}$  – the enrichment of KO unique ProxyPhe peptides,

$E_{ProxyPhe}^{WT}$  – the enrichment of WT unique ProxyPhe peptides,

$E_{ProxyPhe}^{KO,WT}$  – the enrichment of KO and WT shared ProxyPhe-peptides,

$K_{ProxyPhe}^{KO}$  – the number of ProxyPhe-peptides found at least in one of KO replicas but not found in WT replicas,

$K_{ProxyPhe}^{WT}$  – the number of ProxyPhe-peptides found at least in one of the WT replicas but not found in KO replicas,

$K_{ProxyPhe}^{KO,WT}$  – the number of ProxyPhe-peptides found at least in one of the KO replicas and one of the WT replicas,

$N_{Canonical}^{KO}$  – the number of canonical peptides found at least in one of the KO replicas,

$N_{Canonical}^{WT}$  – the number of canonical peptides found at least in one of the WT replicas;

The figures were created using the "matplotlib 3.5.1" Python library.

### Spectra validation

Light synthetic peptides for spectra validation were ordered from GenScript, as HPLC grade ( $\geq 85\%$  purity). These were analyzed using the same LC-MS/MS system and acquisition parameters as indicated above for the endogenous peptides, with the following changes: the gradient was from 4% to 30% acetonitrile in 20 min, and NCE was set to 27 or 30 for HF2 and FS1, respectively. The data were processed with MaxQuant using the following parameters: all FDRs were set to 1, and the individual peptide mass tolerance was set to false. MQ spectra from endogenous and synthetic runs were correlated against each other in ProSight<sup>67</sup> (termed mirror plots above).

### Mass spectrometry analysis of proteolytic peptides (MAPP)

#### Sample preparation

**Purification of proteasome complexes.** Cells were lysed with 25mM HEPES, pH 7.4, 10% glycerol, 5mM MgCl<sub>2</sub>, 1mM ATP, and 1:400 protease-inhibitor cocktail III (Calbiochem), then homogenized through freeze-thaw cycles and passed through a needle. The lysates were cleared by 30-min centrifugation at 21,130g at 4°C. Lysates were treated with 2mM 1,10-phenanthroline (Sigma-Aldrich), cross-linked with 2mM DSP (Thermo Fisher Scientific) for 30min at room temperature, and quenched in 100mM

Tris-HCl, pH 8, 5mM L-cysteine (Sigma-Aldrich) for 10 min at room temperature. For immunoprecipitation, the lysates were then incubated with Protein G PLUS-Agarose (Santa Cruz) with antibodies to PSMA1 and eluted with 100mM Tris-HCl, pH 8, 8M urea and 50mM DTT for 30min at 37°C. Subsequently, 1% trifluoroacetic acid (TFA) was added. Aliquots of each elution fraction were analyzed by SDS-PAGE to evaluate yield and purity.

#### **Purification and concentration of proteasome peptides**

Immunoprecipitated proteasomes and their encompassed peptides were loaded on Ultra-Micro SpinColumn, C18 (Harvard Apparatus) that were prewashed with 80% acetonitrile (ACN) in 0.1% TFA, then washed with 0.1% TFA only. After loading, the cartridges were washed with 0.1% TFA. Peptides were eluted with 30% ACN in 0.1% TFA. Protein fractions were eluted with 80% ACN in 0.1% TFA.

#### **Mass spectrometry sample processing**

Total proteomics: Lysates in 5% SDS in 50mM Tris-HCl were incubated at 96°C for 5min, followed by six cycles of 30s of sonication (Bioruptor Pico, Diagenode, USA). Proteins were reduced with 5mM dithiothreitol and alkylated with 10mM iodoacetamide in the dark. Each sample was loaded onto S-Trap microcolumns (Protifi, USA) according to the manufacturer's instructions. In brief, after loading, samples were washed with 90:10% methanol/50mM ammonium bicarbonate. Samples were then digested with trypsin for 1.5 h at 47°C. The digested peptides were eluted using 50mM ammonium bicarbonate; trypsin was added to this fraction and incubated overnight at 37°C. Two more elutions were made using 0.2% formic acid and 0.2% formic acid in 50% acetonitrile. The three elutions were pooled together and vacuum-centrifuged to dry. Samples were kept at -80°C until analysis.

#### **Liquid chromatography mass spectrometry**

Peptide fraction: ULC/MS grade solvents were used for all chromatographic steps. Each sample was loaded using split-less nano-Ultra Performance Liquid Chromatography (10 kpsi nanoAcquity; Waters, Milford, MA, USA). The mobile phase was: A) H<sub>2</sub>O + 0.1% formic acid and B) acetonitrile + 0.1% formic acid. Desalting of the samples was performed online using a reversed-phase Symmetry C18 trapping column (180 μm internal diameter, 20mm length, 5 μm particle size; Waters). The peptides were then separated using a T3 HSS nano-column (75 μm internal diameter, 250mm length, 1.8 μm particle size; Waters) at 0.35 μL/min. Peptides were eluted from the column into the mass spectrometer using the following gradient: 4% to 35%B in 120 min, 35% to 90%B in 5 min, maintained at 90% for 5min and then back to initial conditions.

The nanoLC (Ultimate3000, Thermo Scientific) was coupled online through a nESI emitter (10 μm tip; FossilonTech) to a quadrupole Orbitrap mass spectrometer (Exploris480, Thermo Scientific).

Data was acquired in data-dependent acquisition (DDA) mode, using a Top10 method. MS1 resolution was set to 70,000 (at 400m/z), mass range of 375-1650m/z, AGC of 3e6 and maximum injection time was set to 100msec. MS2 resolution was set to 17,500, quadrupole isolation 1.7m/z, AGC of 1e5, dynamic exclusion of 40sec and maximum injection time of 150msec.

#### **Mass spectrometry data analysis**

Raw data were analyzed in MaxQuant software (V.2.1.3.0) with the parameters as described above, except for the following: match between runs was enabled and a false discovery rate (FDR) of 1% was applied for peptide identification. For the analysis of tryptic digests, the default parameters were set. Masses were searched against the human proteome database from UniprotKB (last update 2024).

#### **Proteomics processing and label-free quantification**

Peptides resulting from MaxQuant were initially filtered to remove reverse sequences and known MS contaminants. For the MAPP peptide fraction, we removed antibody and proteasome peptides, as well as ribosome-associated proteins as contaminants.

#### **Differential enrichment analysis and aberrant peptides identification**

MAPP differential analysis was performed using the DEP package as described above. For differential abundance analyses, the peptides that were filtered were consistently different (up/ down) in the two KO or WT clones with the higher log<sub>2</sub> fold change values presented and labeled. GO enrichment analysis was performed by enrichR package<sup>104</sup> and Padj values were considered as significant as <0.05.

For ProxyPhe aberrant peptide identification, the custom-reference database was generated as described above, but trimming was not restricted to 13 amino acids, but *in-silico* translation proceeded until a stop codon was read. In addition, group-specific 1% FDR was applied by utilizing FragPipe where Protein Evidence (PE) was: PE1 = Canonical, PE2 = nuORFs and PE3= Phe-OOF, as described before.<sup>70,71</sup> PSMs underwent filtering as described above, except for length and HLA-binding affinity filters. Rational filtering was applied by filtering PSMs of Hyperscore >= 20 and delta score (Hyperscore - Nextscore) >= 4 as shown in Figures S3R and S3S to keep high confidence identifications. Mirror plots projection was performed by Prosit as described above.

#### **Immunogenicity assessment for identified peptides (human)**

##### **T cell activation measurement using flow cytometry**

Protocol was adapted from<sup>73</sup> with modifications; Peripheral blood mononuclear cells (PBMCs) were isolated on day -4 from fresh blood of healthy donors with HLA-matched alleles. PBMCs were subjected to CD14 separation (with CD14 MicroBeads, Miltenyi

Biotech). CD14<sup>+</sup> cell fraction was cryopreserved in freezing media containing 12% DMSO in human serum (Bio IVT) on day -4 and thawed on day -1 (in the presence of DNase I (10 μg/ml; STEMCELL technologies) to isolate T cells (with EasySep Human T cell enrichment kit, STEMCELL technologies). CD14<sup>+</sup> monocytes were differentiated into immature DCs for three days with GM-CSF (800 IU/ml, PeproTech) and IL-4 (50 IU/ml, PeproTech). On day -1, DCs were matured by the addition of a maturation cocktail containing 10 ng/ml Lipopolysaccharides (LPS from *Escherichia coli* O111:B4, (Sigma-Aldrich)) and 100 IU/ml IFN $\gamma$  (PeproTech) for 16 hours. On day 0, mature monocyte-derived DCs were pulsed with the corresponding synthetic peptides or DMSO at a concentration of 1 μg/ml for 2 hours and subsequently co-cultured with the autologous T cells for 12 days. On days 3, 5, 7, and 9, IL-7 (5 ng/ml, PeproTech) and IL-15 (5 ng/ml, PeproTech) were added to the culture media. On day 12, T cells were re-stimulated with irradiated (35 Gy) 721.221 B cells expressing the relevant (predicted) HLA allele, pre-pulsed with the relevant peptides, and cultured for an additional 7 days. On day 19, cells were co-cultured with 721.221 B cells, pre-pulsed with the aberrant peptide, or canonical control peptide (that was previously identified by immunopeptidomics. Notably, both aberrant and canonical peptides were predicted to bind strongly to HLA-A\*02:01, HLA-A\*11:01 or HLA-B\*57:01 (Rank BA < 2% by NetMHCpan)), or DMSO, and subjected to flow cytometry analysis of TNF $\alpha$ , IFN $\gamma$ , and 41BB abundance 6 or 18 hours later:

Cells were harvested and plated in U-bottom 96-well plates and washed with PBS. Cells were then stained with LIVE/DEAD Fixable blue dead cell stain (Thermo Fisher Scientific), washed with PBS, and stained for surface antigens (PE anti-human CD3, FITC anti-human CD8a and APC anti-human CD137 (41BB) (BioLegend)). Cells were then washed twice with MACS buffer (Miltenyi Biotec), resuspended in MACS buffer, and analyzed by CytoFLEX flow cytometer (Beckman Colter). For intracellular staining, cells were treated with Monensin and Brefeldin A (BioLegend) 6 hours before harvesting. Following surface antigen staining, cells were fixed with 4% paraformaldehyde (Fisher Scientific), washed and permeabilized with intracellular staining permeabilization wash buffer (BioLegend) according to the manufacturer's protocol, and stained with APC anti-human IFN $\gamma$  or APC anti-human TNF $\alpha$  (BioLegend). For analysis, we used Kaluza analysis software (Beckman Coulter).

### Identification of T cells reactive to aberrant peptides using multimers

Priming of naïve CD8<sup>+</sup> T cells with autologous monocyte-derived DCs (MoDCs) and identification of T cells reactive to aberrant peptides presented on HLA-A\*02:01 was performed as previously described.<sup>17,73,75,125</sup> In brief, monocytes and naïve CD8<sup>+</sup> T cells were isolated from HLA-A\*02:01 positive healthy donors. Peptide-loaded MoDCs were co-cultured with naïve CD8<sup>+</sup> T cells for 10–12 days prior to screening of cultures for the presence of pMHC multimer-reactive CD8<sup>+</sup> T cells complexed with aberrant peptides or control peptides. The pMHC multimers were labeled with various combinations of two streptavidin-fluorochromes, including PE, PE-Cy7, PE-CF594, BV605, BV421, APC-R700 or APC, and were prepared in-house as previously described.<sup>126,127</sup> Neopeptide-reactive CD8<sup>+</sup> T cells were identified as live CD8<sup>+</sup> T cells staining double positive for two fluorochrome-conjugated pMHC multimers while being negative for all other fluorochromes. Immunogenicity of translation-aberrant peptides was compared to control peptides representing known neopeptides encoded by shared mutations<sup>76,77</sup>: covering the JAK2\_p.V617F mutation (VLNYGVCF; donors 1 and 2) and TP53\_p.R175H mutation (HMTEVVRHC; for donors 3–6).

### In vivo tumor inoculation

For cell inoculation, 5 × 10<sup>5</sup> tumor cells in 100 μl PBS were injected intradermal into the right lower flank of 6–8-week-old C57BL/6, NSG or Rag2 KO female mice after shaving. Tumors were measured using calipers. Tumor volume was assessed by measuring tumor diameter in the long (y) and short axis (x) and calculation using the equation X<sup>2</sup> × Y × 3.14/6. Mice with a tumor volume of >1 cm<sup>3</sup> were euthanized. Statistical analysis was performed with KS test. For KS significant days (Pvalue < 0.05) we performed a Wilcoxon-pairwise test to determine the source of the variance within each day.

### In vivo CD8<sup>+</sup> T cell depletion

For CD8<sup>+</sup> T cell depletion, mice were treated with monoclonal anti-CD8 $\alpha$  antibody (clone 2.43, BioXCell) or monoclonal antibody rat IgG2b control (clone LTF-2, BioXCell). Each antibody was administered intra-peritoneum (i.p), first, at 250 μg per dose 3 days before tumor cells inoculation (day-3), and then at 200 μg per dose at day 0 (the day of tumor cell inoculation) and twice weekly thereafter. Depletion efficiency was examined at days 0 and 20 using flow cytometry analysis of blood with the following antibodies: FITC anti-mouse CD3 (clone 17A2), PE anti-mouse CD4 (clone RM4-5) and APC anti-mouse CD8 (clone 53-6.7), (BioLegend).

### Tumor cell lysate preparation

To generate tumor cell lysates (TCL), tumor cells were trypsinized, washed and resuspended in 1 mL PBS. Lysates were prepared by 4 freeze-thaw cycles, followed by passing 30 times through a 27-gauge needle. Lysates were then centrifuged at 1500 rcf for 10 minutes to remove cell debris, and protein levels were quantified by Pierce™ BCA Protein Assay Kits (ThermoFisher).

### T cell proliferation assay

To isolate DCs, the inguinal, brachial, and axillary lymph nodes were collected from euthanized mice, homogenized in 2% FBS and 5 mM EDTA supplemented HBSS (Sigma-Aldrich), and passed through a 70 μm strainer (ThermoFisher). Cells were next incubated with anti-CD11c MicroBeads and column (Miltenyi Biotec) and used immediately for T cell proliferation assays. To extract CD8<sup>+</sup> T cells, spleens were collected, homogenized in 2% FBS and 5 mM EDTA supplemented HBSS, and passed through a 70 μm strainer (ThermoFisher). Lymphocytes were enriched on a Histopaque-1077 Hybri-Max (Sigma-Aldrich) density gradient medium. Collected PBMCs were

washed twice with a complete RPMI 1640 medium [-RPMI 1640 medium supplemented with 1% pen-strep, 10% heat-inactivated FBS, 1% sodium pyruvate, 1% MEM-Eagle non-essential amino acids, 1% insulin-transferrin-selenium (Thermo Fisher Scientific), 50 $\mu$ M  $\beta$ -mercaptoethanol (Sigma-Aldrich)], followed by incubation with anti-CD8 magnetic beads (MojoSort™ Nanobeads, BioLegend or CD8a (Ly-2) MicroBeads, mouse Miltenyi Biotec) according to the manufacturer's instructions. CD8<sup>+</sup> T cells were stained with 5 $\mu$ M CellTrace™ CFSE (ThermoFisher) according to the manufacturer's instructions. Stained T cells were incubated for approximately 4 hours with 100IU IL-2 before incubation with DCs, in order to reduce the amount of CFSE in the cells. 2 $\times$ 10<sup>5</sup> CFSE-labeled T cells were co-cultured with isolated DCs pre-loaded for 16 hours with 20  $\mu$ g/mL of TCL at a ratio of 3:1 (T:DC), or, with isolated DCs pre-loaded for 1 hour with 10  $\mu$ g/mL of synthetic peptide at a ratio of 4:1 (T:DC) in a round-bottom 96-well plate. Four days later, cells were stained with extracellular markers APC anti-CD3 (BioLegend), and BV405 anti-CD8 antibodies (BioLegend) or BV405 anti-TCR $\beta$  (BioLegend) and BV610 anti-CD8 (BioLegend) antibodies for 15 minutes and for two minutes with DAPI or Propidium Iodide (PI), respectively, and analyzed by flow cytometry (CytoFLEX, Beckman Coulter).

### Dendritic cells immunopeptidomics

Bone marrow cells were isolated from the tibia, femur and hip bones of control C57BL/6 mice under sterile conditions in a laminar hood. Bones were washed extensively in PBS, incubated for 20 sec in 70% EtOH and washed again twice in PBS. Bones were ground using a sterile mortar and pestle and filtered through a 70  $\mu$ m strainer. Cells were then washed, re-filtered, and cultured in 15cm culture dishes for 4-5 days in complete DMEM medium (Gibco) in the presence of 50ng/ml GM-CSF (PeproTech) and 10ng/mL IL-4 (PeproTech) to generate monocyte-derived DCs. Cells were then incubated for 16 hours with 20 $\mu$ g/mL of lysates derived from either *Tyw2* WT or KO cells, or without any lysate (unloaded DC control). Cells were then washed, harvested, and stored at -80°C until further processing. Sample preparation for immunopeptidomics, MS/MS sample preparation and data acquisition were performed as described above.

To analyze the DC immunopeptidomic data, FragPipe group-specific 1% FDR searched '.d files' (activating ion-mobility) from the TTP.<sup>70,71</sup> Canonical Ensemble GRCm39 and ProxyPhe *in-silico* translated database were inquired as different groups by setting the 'Group variable' to 'protein evidence from FASTA file'. The default Nonspecific-HLA workflow was utilized, and subsequent modifications and filters were performed for known contaminants and reverse decoy, length, HLA-binding affinity, I2L, and scan validation function. MaxLFQ was set to a minimum ion of 2 and MBR was set to off. *De novo* sequencing and peptide-PRISM search (described above) were applied to avoid peptide ambiguity. PSMs were annotated if Peptide-PRISM could identify an additional source or if Peptide-PRISM interpreted the spectrum by a different sequence (Table S3). PSMs were also searched against the DC-only data that underwent the same data analysis pipeline. For high-confidence identifications, we observed PSMs with delta score > 4 and Hyperscore > 17 as this threshold we were able to observe KO-specific ProxyPhe-identifications (shown in Figure S5R). PSMs were generated by the FragPipe-PDV viewer,<sup>128</sup> and mirror plots were obtained for the experimental fragment ion spectrum VS predicted spectrum using deep learning.<sup>128</sup>

### Immunization of mice

To perform an antigen-adjuvant vaccination, PBS solution containing a pool of ten peptides (1mg/ml) was emulsified in complete Freund's adjuvant (CFA; 1mg/ml M. Tuberculosis H37 Ra; BD) in a 1:1 (v/v) ratio by sonication (40% amplitude, Pulser: 25 seconds (net), 2 sec on, 2 sec off). Naïve 7-week-old female C57BL/6 mice were subcutaneously injected with the emulsion into the lower flanks (right + left; each animal was injected with a total of 0.2 ml harboring 100 $\mu$ g peptide-pool, 10 $\mu$ g of each peptide). 11 days later, mice were boosted subcutaneously with the same peptide pool, emulsified in incomplete Freund's adjuvant (IFA; BD).

### Ex-vivo peptide stimulation

T cells from tumor-bearing mice (from spleens and dLNs) were analysed on day 27 after tumor-cell inoculation, and 5 doses of anti-PD-1 antibody treatment, on days 11, 14, 17, 21 and 24. Splenic T cells were isolated using CD8a (Ly-2) MicroBeads (Miltenyi Biotec) following the manufacturer's protocol, resuspended in complete RPMI 1640 medium, washed with PBS and stained with CFSE as described above, and co-cultured with isolated DCs (pre-loaded for 1 hour with 10  $\mu$ g/mL of synthetic peptide) at a ratio of 4:1 (T:DC) in a U-bottom 96-well plate. 16 hours later, culture media was collected and subjected to enzyme-linked immunosorbent assay (ELISA) for the measurement of Mouse IFN-gamma (DuoSet ELISA; R&D systems). Four days post co-culture, T cell proliferation analysis was performed using flow cytometry (as described above).

Cells isolated from the dLNs were cultured in complete RPMI 1640 and plated in a U-bottom 96-well plate (at a concentration of 10<sup>6</sup> cells/ml) in the presence of 1 $\mu$ M synthetic peptide. 2 hours later, Monensin and Brefeldin A (BioLegend) were added to the culture media. 14 hours later, cells were washed with PBS and stained with LIVE/DEAD Fixable blue dead cell stain (Thermo Fisher Scientific). Cells were then washed with PBS, resuspended with MACS buffer (Miltenyi Biotec) supplemented with Mouse TruStain FcX™ antibody (BioLegend) for 15 minutes at room temperature and stained for surface antigens FITC anti-CD3 (BioLegend) and A700 anti-CD8 antibodies (BioLegend) for 30 minutes on ice. Stained cells were then washed twice with MACS buffer, fixed with 4% paraformaldehyde (Fisher Scientific), washed and permeabilized with intracellular staining permeabilization wash buffer (BioLegend) according to the manufacturer's protocol, and stained with PE anti-TNF $\alpha$  (BioLegend). Following two washes with MACS buffer, cells were resuspended in MACS buffer and analyzed by CytoFLEX flow cytometer (Beckman Colter). For analysis, we used FlowJo V10.10.0 (BD Biosciences) analysis software.

T cells from immunized mice were analysed 7 days post the boost injection. Spleens were collected, homogenized in 2% FBS and 5mM EDTA supplemented HBSS, and passed through a 70  $\mu$ m strainer (ThermoFisher). Cells were then washed with PBS, and red blood cells were lysed by incubation in ACK lysis buffer (Gibco) for 5 minutes at room temperature, following two washes with PBS and filtration through a 70  $\mu$ m strainer (ThermoFisher). Cells were resuspended in complete RPMI 1640 medium, counted and plated in a U-bottom 96-well plate (at a concentration of  $10^7$  cells/ml) in the presence of 1  $\mu$ M synthetic peptide. 2 hours later, Monensin and Brefeldin A (BioLegend) were added to the culture media, and 14 hours later, cells were subjected to intracellular staining as described above.

### T cell:tumor cell co-culture

T cells from immunized mice were analysed 14 days post the boost injection. Spleens were collected, homogenized in 2% FBS and 5mM EDTA supplemented HBSS, passed through a 70  $\mu$ m strainer (ThermoFisher) and resuspended in complete 1640 RPMI medium. PBMCs were isolated using Ficoll Paque Plus (Cytiva) according to the manufacturer's instructions and resuspended in wash buffer containing PBS, pH 7.2, 0.5% bovine serum albumin (BSA), and 2 mM EDTA. CD8<sup>+</sup> T cells were then isolated using CD8a (Ly-2) MicroBeads (Miltenyi Biotec) according to the manufacturer's instructions, resuspended in complete RPMI 1640 medium, and cultured in a flat bottom 96 well plate ( $2 \times 10^5$  cells/well) that was pre-seeded with  $4 \times 10^4$  cancer-cells the night before. T cell reactivity was measured 16 hours later by flow cytometry using the following antibodies: FITC anti-CD3 (BioLegend), A700 anti-CD8 (BioLegend), PE-anti TNF $\alpha$  (BioLegend) and LIVE/DEAD Fixable blue dead cell stain (Thermo Fisher Scientific).

### scRNA-seq sample preparation

Tumors were surgically removed and dissociated according to manufacturer's recommendations (Miltenyi Biotec). Dissociated tumor cells were then cryopreserved with CELLBANKER 2 (serum-free media, Amsbio). Four cryopreserved tumors from each tumor background and timepoint were then thawed in a 37°C water-bath, pooled by sample type into 9mL of warm 10% FBS in DMEM, pelleted, and washed twice with PBS. Cells were then labelled in PBS with lipid-modified oligonucleotides hybridized to a sample-specific MULTI-seq barcode as described previously.<sup>80</sup> MULTI-seq LMO labelling reactions were then quenched with 1% BSA in PBS, pooled, and washed with 1% BSA in PBS prior to labelling with Zombie NIR viability dye (1:500 in PBS; BioLegend). After 15 minutes on ice, the cells were diluted with 5mL of 2% FBS in PBS (FACS buffer), pelleted, and resuspended in 150  $\mu$ L of Fc-block (1:200 in FACS buffer; Tonbo). After 5 minutes on ice, the cells were diluted with 5mL of FACS buffer, pelleted, and resuspended in 100  $\mu$ L of an antibody cocktail containing 1:100 anti-CD44 (PE-Cy7; BioLegend), 1:100 anti-TCRb (FITC; BioLegend), and 1:40 anti-CD45 (violetFluor™ 450; Tonbo) mouse monoclonal antibodies in FACS buffer. After 30 minutes on ice, the cells were diluted with 5mL of FACS buffer, washed once with 5mL of FACS buffer, and filtered through a 70  $\mu$ m Macs SmartStrainer prior to FACS enrichment for CD45<sup>+</sup> live immune cells using a BD FACSaria II instrument. After FACS, cells were counted, the concentration was adjusted to  $1 \times 10^6$  cells/mL, and 43.2  $\mu$ L of the cell suspension was 'super-loaded' across 4 lanes of a 10x Genomics 3' scRNA-seq V3.1 chip.

### scRNA-seq library preparation and next generation sequencing

scRNA-seq libraries were prepared according to manufacturer's recommendations (10x Genomics). MULTI-seq libraries were prepared as described previously.<sup>80</sup> scRNA-seq and MULTI-seq libraries were pooled and sequenced using NovaSeqX 10B flow cells. scRNA-seq libraries were sequenced to an average of 65,000 reads per cell while MULTI-seq libraries were sequenced to an average of 3,000 reads per cell.

### scRNA-seq library pre-processing, quality-control, MULTI-seq sample classification, and cell type annotation

scRNA-seq library FASTQs were pre-processed using Cell Ranger version 6.0.0 (10x Genomics) and aligned to the mm-10-3.0.0 reference transcriptome. Cell Ranger aggregate was used to perform read-depth normalization. Filtered read depth normalized scRNA-seq count matrices were then read into R and parsed to exclude genes with fewer than 5 counts across all cell barcodes. Parsed scRNA-seq data was then pre-processed using Seurat V5<sup>98</sup> and clusters with low total UMIs and/or high proportion of mitochondrial transcripts were excluded. Cell barcodes passing the first quality-control workflow were then used to pre-process MULTI-seq barcode FASTQs and perform sample classification using the 'deMULTiplex2' R package.<sup>99</sup> Following MULTI-seq demultiplexing, unclassified cells and clusters enriched with MULTI-seq-defined doublets were removed prior to re-processing. These data were used for unsupervised clustering, differential gene expression testing, and manual annotation of major immune cell types based on the following literature-supported marker genes: CD4<sup>+</sup> T cells (*Cd3e*, *Cd4*), CD8<sup>+</sup> T cells (*Cd3e*, *Cd8b1*), B cells (*Cd79a*, *Igkc*), ILCs (*Cd3e*, *Fcer1g*),<sup>81</sup> Tregs (*Cd3e*, *Foxp3*), NK cells (*Gzma*, *Klre1*), Mono/Macs (*Csf1r*, *Lst1*), DCs (*Syngn2*, *Napsa*), and proliferative cells (*Mki67*, *Hells*).

After annotating the major immune cell types, the data was subsetted by cell type and re-processed prior to unsupervised clustering, differential gene expression testing, and manual annotation of immune cell subtypes based on the following literature-supported marker genes: naïve (*Ccr7*, *Sell*), memory-like (*Tcf7*, *Ilr1*, *Cxcr3*), effector-like (*Gzmb*, *Gzmk*, *Ccl5*), progenitor exhausted (*Xcl1*, *Lag3*), exhausted (*Pdcd1*, *Lag3*), and proliferative CD8<sup>+</sup> T cells (*Mki67*, *Hells*)<sup>83,84</sup>; as well as cytotoxic (*Prf1*, *Ccl5*, *Gzma*), immunomodulatory (*Ctla2a*, *Cd27*, *Ly6e*), and proliferative NK cells (*Mki67*, *Hells*).<sup>129</sup> Notably, low-quality/doublet cell clusters missed during the initial quality-control workflows were removed during the subtype annotation workflow, after which all datasets were re-processed, as described previously.<sup>82</sup>

### CODEX multiplexed tissue imaging

Oligo-conjugated primary antibodies were prepared 50 $\mu$ g at a time, precisely as detailed in Black et al.<sup>85</sup> For CODEX multiplexed imaging, tumors were excised at day 21 post-inoculation, fixed in 4% (w/v) PFA for 24 h, and restored in 1% PFA until embedded in paraffin for histological analysis. The tissue was pretreated by heating the slides in an incubator at 70°C for 1 h to melt the paraffin and improve tissue attachment to the slide. Immunohistochemistry was performed on deparaffinized and rehydrated 4- $\mu$ m thick paraffin-embedded sections using Xylene and a decreasing concentration of Ethanol (100%, 95%, 80%, 70%). For antigen retrieval, the slides were heated in Dako retrieval solution buffer (- Target Retrieval Solution, pH 9, Agilent, diluted 1:10) in a PT module, followed by washing steps with ddH<sub>2</sub>O and TBST and blocking with CODEX FFPE blocking solution (B1+ B2+ B3+ BC4) for 1 h at RT in a humidity chamber. The tissue was incubated overnight at 4°C with the antibody mix diluted in FFPE blocking solution. The next day, the tissue was fixated using three fixation steps. First, the antibodies were fixed with PFA fixation solution, followed by the treatment with ice-cold methanol for the precipitation of proteins, the removal of lipids from cells and clearing fluorescent reporters with the cell membranes, and finally the incubation with final fixative solution (BS3 in PBS) for maintaining CODEX antibodies bound to the tissue for the hybridization and stripping cycles during imaging. Until the experiment run, the specimens were stored in CODEX staining buffer (S4) solution at 4°C. Using the Experiment Designer, all PhenoCycler Reporters were assigned to a cycle number and cycles were associated with specific wells. For each cycle the reporter master mix was prepared by diluting each reporter in plate buffer and for each run two blank cycles with plate buffer were prepared. During the PhenoCycler run, in each cycle, the instrument withdrew the Reporter Master Mix from one well of the 96-well plate.

Following the antibody labeling, a flow cell was affixed to the tissue slide. Then the slide was mounted into the stage carrier and placed into the PhenoCycler-Fusion Phenolmager (Akoya Biosciences, Marlborough, MA), and multicycle imaging was initiated using 20 $\times$  magnification.

### In vivo $\alpha$ -PD-1 therapy

Animals were treated with 250 $\mu$ g of anti-PD-1 flat dose (clone RMP1-14, BioXCell) or rat IgG2a isotype control (clone 2A3, BioXCell). Antibodies were administrated i.p., starting on day 11 or 12 post tumor cell inoculation, or when the tumors' mean volume reached 50mm<sup>3</sup> (conditions i or ii, shown in Figure 7A, respectively) and twice weekly thereafter until mouse reached the humane endpoint (- tumor volume=1cm<sup>3</sup> or developed ulceration). Mice were monitored three times a week. When reaching the humane endpoint, mice were sacrificed, and the tumor weight was measured. Mice that did not reach the humane point by day 50 were sacrificed, and the tumor was weighed. Kaplan-Meier plots were generated by utilizing the 'survminer' package from R, and statistics were obtained by the Wald, log-rank, likelihood ratio test. Mice that did not reach the human-end point by day 50 were censored and sacrificed as described above.

### Patient DATA analysis

Melanoma patient clinical and transcriptomic data were downloaded from public databases, as detailed in the "data and code availability" section above. Survival outcomes and ICB objective response were analyzed by computing the following variables for the human melanoma cohorts depending on data availability: overall survival (TCGA and Riaz et al.<sup>87</sup> cohorts), progression free survival (TCGA, Riaz et al.<sup>87</sup> and Cabrita et al.<sup>88</sup> cohorts) and ICB objective response (Riaz et al.<sup>87</sup> and Auslander et al.<sup>89</sup> cohorts).

Survival analyses were performed using the R packages *survminer* v.0.4.9 and *survival* v.3.3.1 where *TYW2* high versus low expression was determined by binarizing *TYW2* expression at the 50th percentile. TMB status was determined using a previously established threshold of 100 mutations to differentiate between high and low TMB patients in the Riaz et al.<sup>87,130</sup> cohort. AUCs were calculated with the *roc()* function in the *pROC* R package v1.18.5.

To identify differentially expressed genes (DEGs) in TCGA data of *TYW2*-high versus *TYW2*-low tumors we employed *DESeq2*<sup>107</sup> with criteria of  $|\log_2$  fold change| > 1 and adjusted p-value < 0.05. Ranking the DEGs was performed by computing hazard ratios (HRs) and p-values for overall survival and progression free survival. The effect size defined as HRs (1/HR when HR < 1) for survival analysis and AUCs (1-AUC when AUC < 0.5) for ICB objective response, was used to rank the genes.

Cytolytic score was defined as the geometric mean of the expression levels of the genes *GZMA* and *PRF1*, as previously described.<sup>131</sup> Exhausted score was defined as the geometric mean of the expression levels of the genes *PDCD1*, *CTLA4*, *LAG3*, *HAVCR2*, and *TIGIT*, as previously described.<sup>132</sup>

## QUANTIFICATION AND STATISTICAL ANALYSIS

### Intercellular signaling predictions

Intercellular signaling interactions were predicted using *CellChat*<sup>86</sup> first by splitting the full scRNA-seq dataset by tumor background and timepoint and processing individual *CellChat* objects using the demonstrated workflow. Processed *CellChat* objects were then merged using the 'mergeCellChat' function, enabling comparative visualizations of weighted cell-cell signaling networks.

### scRNA-seq statistical tests

Statistically-significant shifts in cell type and subtype proportions in the scRNA-seq data were identified using the 'propeller' function with bootstrapping in the 'Speckle' R package.<sup>100</sup> Differentially-expressed genes between clusters in all datasets were defined using the Wilcoxon rank-sum test as implemented in the 'FindAllMarkers' Seurat function. Specific differential expression testing was

performed using the Wilcoxon rank-sum test as implemented in the 'FindMarkers' Seurat function. Statistically-significant differences in LAG3<sup>+</sup> and Ki67<sup>+</sup> CD8<sup>+</sup> T cell proportions in the CODEX data were identified using the 't.test' R function.

### Codex image processing

Cell segmentation and classification was applied to the fluorescence images using QuPath<sup>103</sup> to detect and quantify the T cells (CD3<sup>+</sup> CD8<sup>+</sup>).<sup>103</sup> Nuclei were segmented from the 4',6-diamidino-2-phenylindole (DAPI) channel using StarDist<sup>133</sup> and further inflated to have approximated cell segmentation. To improve nuclei segmentation a new StarDist model was trained using the ZeroCostDL4Mic<sup>134</sup> StarDist notebook with examples that were not perfectly segmented by the provided model. The cells were then classified as positive or negative for each of the stains, and the total number of double or triple-positive cells and their respective ratio were quantified within each tumor. Positive/Negative random trees cell classifiers were trained for each stain independently on multiple image regions representative of the tissue characteristics and experimental conditions. The classifiers were then combined to detect double and triple-positive cells. The classifiers were then applied to each tumor, based on a threshold classifier, to quantify the total number of the double positive CD3<sup>+</sup> CD8<sup>+</sup> T cells and their respective ratio to the total number of cells per tumor and the triple positive CD3<sup>+</sup> CD8<sup>+</sup> LAG3<sup>+</sup> and CD3<sup>+</sup> CD8<sup>+</sup> Ki67<sup>+</sup> cells and their respective ratio to the number of CD3<sup>+</sup> CD8<sup>+</sup> T cells.

### Statistical analyses

All statistical analyses were performed with R as described above. For all experiments shown above, measurements were taken from distinct samples. All statistical tests used in the study were two-sided tests. Assumptions and multiple comparisons corrections were tested (or corrected) for each reported statistic by the Shapiro test, Leven's test and Bonferroni correction, as described above. A pellet results of statistical parameters, including central tendency and variation (means differences and confidence intervals), ANOVA or Kruskal-Wallis test results, are available upon request from the corresponding author. Standard errors of the mean are shown as error bars or unshown when only the observed data points are shown. Null hypothesis testing statistics are described in the figure legend, while confidence intervals and estimation of effect size (calculated by Cohen's D for FS reporter experiments) are not shown.

Statistics for the human data analysis were computed using R (v.4.3.0). DeLong's test<sup>135</sup> was used for calculating p values for AUCs. We calculated HRs with 95% confidence intervals and p values with univariable Cox proportional hazards regression using the *coxph()* function.<sup>136,137</sup> All the tests are two-tail unless otherwise specified. No statistical methods were used to pre-determine sample sizes because we used all available samples from published studies.